Measurement of the $Z \longrightarrow \tau\tau$ production cross-section in proton-proton collisions at $\sqrt{s} = 7$ TeV with the ATLAS detector

Justin Griffiths

A dissertation
submitted in partial fulfillment of the
requirements for the degree of

Doctor of Philosophy

University of Washington

2012

Reading Committee:

Anna Goussiou, Chair

Jeffrey Wilkes

Henry Lubatti

Program Authorized to Offer Degree:
Department of Physics

University of Washington

Abstract

Measurement of the $\boldsymbol{Z \longrightarrow \tau\tau}$ production cross-section in proton-proton collisions at $\sqrt{s} = 7$ TeV with the ATLAS detector

Justin Griffiths

Chair of the Supervisory Committee:
Professor Anna Goussiou
Department of Physics

The first measurement of the inclusive cross-section of the Z boson decaying to two tau leptons was measured with the ATLAS detector at the LHC. The data sample in this analysis represents an integrated luminosity of 35 pb^{-1} of proton-proton collisions at a center of mass energy of $\sqrt{s} = 7$ TeV. Separate measurements were performed in four decay modes based on how the two tau leptons decay: to hadrons and an electron, to hadrons and a muon, to an electron and a muon, and to two muons. In all four final states, inclusive cross-section measurements were made both in the fiducial region of the ATLAS detector where acceptance is high and in the full phase space, restricted to the mass range of $[66, 116]$ GeV. The measurements from the four individual channels were then combined to yield the combined $Z \rightarrow \tau\tau$ cross-section of 970 ± 70 (stat.) $\pm$ 60 (sys.) $\pm$ 30 (lumi.) pb.

TABLE OF CONTENTS

LIST OF FIGURES

LIST OF TABLES

GLOSSARY

CROSS-SECTION (σ): The cross-section is the area, measured in barns (1 b = 10^{-24} cm^2), in which an interaction will occur.

DELTA R (ΔR): Angular distance between two points in space defined as: $\sqrt{(\Delta\eta)^2 + (\Delta\phi)^2}$.

IMPACT PARAMETER (d_0/z_0): The transverse impact parameter, d_0, is the point of closest approach of a track to the interaction point in the plane transverse to the beam, while the longitudinal impact parameter, z_0, is the point of closest approach along the beam axis direction.

LUMINOSITY ($\mathcal{L}$): The instantaneous luminosity is the number of particles per cross-sectional area per unit time. The integrated luminosity is the total number of particles per unit area. Instantaneous luminosity is measured in units of $\frac{1}{\mathrm{cm}^2\mathrm{s}}$, while integrated luminosity is measured in units of $\frac{1}{\mathrm{b}}$ (barn b = 10^{-24}cm^2).

MISSING TRANSVERSE ENERGY ($E_{\mathrm{T}}^{\mathrm{miss}}$): The total energy, transverse to the beam, of all non-interacting particles in an event inferred from the momentum imbalance in the event.

PRIMARY VERTEX (PMV)/INTERACTION POINT (IP): The three dimensional location at which the hard scattering event occurred.

PSEUDORAPIDITY (η): The pseudorapidity defined as: $-\ln\tan(\theta/2)$, is an approximation of the rapidity when the mass of a particle is much smaller than its energy.

RAPIDITY: The invariant measure of momentum boost along the beam axis: $y = \frac{1}{2}\ln\frac{E+p_z}{E-p_z}$.

TRANSVERSE ENERGY/MOMENTUM ($E_{\mathrm{T}}/p_{\mathrm{T}}$): The energy (momentum) of a particle measured transverse to the direction of the accelerating beams.

LIST OF ACRONYMS

BDT: Boosted Decision Tree

BLUE: Best Linear Unbiased Estimator

CDF: Collider Detector at Fermilab

CM: Center of Mass

CMS: The Compact Muon Solenoid

CSCs: Cathode Strip Chambers

D0: Detector on the Tevatron accelerator at point 'D0' located at Fermilab.

DLV: Dilepton Veto

EM: Electromagnetic

EMB: Electromagnetic Barrel (Calorimeter)

EMEC: Electromagnetic Endcap (Calorimeter)

FCal: Forward Calorimeter

HAD: Hadronic

ID: Inner Detector

IP: Interaction Point

LAr: Liquid Argon

LEP: Large Electron-Positron (Collider)

LHC: Large Hadron Collider

LO: Leading Order (in perturbation theory)

MC: Monte Carlo

MDT: Monitored Drift Tube

MJ: Multijet

MS: Muon Spectrometer

NLO: Next-to-Leading Order (in perturbation theory)

NNLO: Next-to-Next-to-Leading Order

OS: Opposite Signed (electric charge)

PDF: Parton Distribution Function

PMV: Primary Vertex

PS: Proton Synchrotron

PSB: Proton Synchrotron Booster

QCD: Quantum Chromodynamics

RF: Radio Frequency

ROI: Region of Interest

RPCs: Resistive Plate Chambers

SCT: Semiconductor Tracker

SD: Sensitive Detector

SM: Standard Model

SPS: Super Proton Synchrotron

SS: Same Signed (electric charge)

TES: Tau Energy Scale

TGCs: Thin Gap Chambers

TRT: Transition Radiation Tracker

VDM: Van der Meer

ACKNOWLEDGMENTS

I would like to thank my adviser, Anna Goussiou, for advising me through my graduate career. I would also like to thank my colleagues, Matthew Beckingham and Nikolaos Rompotis, who took time out of their busy schedules to read and advise me on my thesis. I must thank the entire ATLAS Collaboration for all the massive work that the 3000+ collaborators performed to make analyses like mine possible. I also thank the National Science Foundation which helped to make research abroad at CERN possible.

DEDICATION

to my parents

Chapter 1

INTRODUCTION

This thesis concentrates on the first measurement of the $Z \rightarrow \tau\tau$ production cross-section at a center of mass energy ($\sqrt{s}$) of 7 TeV in proton-proton (pp) collisions at the Large Hadron Collider (LHC) and collected by the ATLAS detector. The measurement of known physics processes with tau leptons is the crucial first step in using tau leptons in the final state to discover the Higgs particle or to search for new physics beyond the Standard Model. This chapter will discuss the Standard Model, proton-proton collisions, an introduction and motivation for studying tau physics, and finally give an outline of the analysis and thesis as a whole.

1.1 Standard Model

Currently the Standard Model (SM) of Particle Physics is the theory most widely accepted by physicists and supported by experimental evidence to explain the structure of matter and the fundamental interactions at the smallest dimensions. The standard model gauge symmetry group can be written as:

$$SU(3) \times SU(2) \times U(1) \tag{1.1}$$

where $SU(3)$ represents the Strong Interaction mediated by 8 flavors of gluons, while $SU(2) \times U(1)$ represents the Electroweak symmetry mediated by the three massive vector bosons $W^{\pm}/Z$ and the massless photon (γ). The particles believed to be elementary along with the force carriers are depicted in Figure 1.1.

1.1.1 Quarks and Leptons

Quarks and leptons are fermions (spin 1/2 particles) that are grouped into three generations. Quarks, within each generation, are generally classified as either “up” type or “down” type

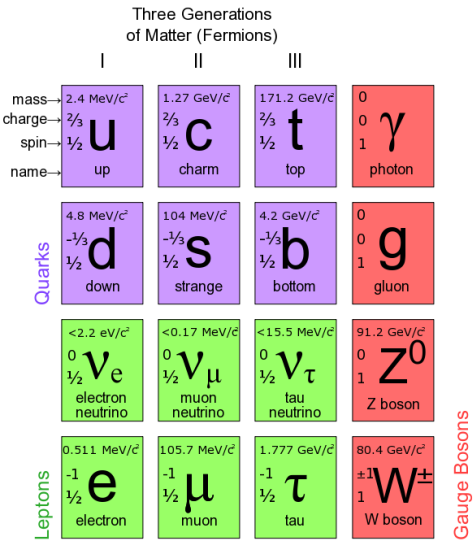

Figure 1.1: The known elementary Standard Model particles and force carriers. The charge, spin, and mass is also displayed for each particle.

quarks based on whether their charge is 2/3 (u-type), or 1/3 (d-type). The three quark generations are: up/down (u/d), charm/strange (c/s), and top/bottom (t/b). Each lepton generation consists of a charged particle, e, μ, or τ, and their associated chargless neutrinos, ν_e, ν_μ, or ν_τ. Every quark and lepton has a corresponding anti-particle with the same mass and spin, but opposite charge. Neutrinos, however, may be their own anti-particles (majorana particles [1]). Observations of neutrinoless double beta decay may provide insight into whether neutrinos are majorana or not [2].

1.1.2 Strong Interaction

The strong interaction is the force responsible for binding quarks in hadrons (such as protons and neutrons). The Strong interaction acts on quarks and gluons. All quarks have one of three color charges. Quark flavor (d u s c b t), electric charge, and color charge are all conserved in strong interactions. The study of the strong interaction is quantum chromodynamics (QCD).

1.1.3 Electroweak Interaction

The electroweak interaction arises from the unification of the weak and electromagnetic forces through spontaneous symmetry breaking. The electromagnetic force is mediated by the massless photon, while the weak force is mediated by massive vector bosons ($W^{\pm}/Z$). The fact that the vector bosons were not massless seemingly contradicted the electroweak symmetry. Salam, Glashow, and Weinberg were able to show that through spontaneous symmetry breaking, the bosons were able to acquire mass while still maintaining the gauge invariance of the theory [3, 4]. It is believed that the massless bosons acquire mass through the Higgs mechanism. The existence of the Higgs mechanism would imply the existence of another massive scalar particle; the Higgs boson.

To date, the Higgs boson has yet to be directly observed. Currently the ATLAS collaboration has excluded the SM Higgs boson at a 95% confidence level in the mass ranges $[112.7, 115.5]$, $[131, 237]$, and $[251, 468]$ GeV analyzing primarily the $H \to \gamma\gamma$, $H \to WW$, and $H \to ZZ$ decay channels [5]. The CMS collaboration, using the $\tau\tau$, $\gamma\gamma$, bb, WW, and ZZ decay modes, has excluded the SM Higgs boson at a 95% confidence level in the mass range $127 < m_H < 600$ GeV [6]. Previous measurements at LEPII have put a lower limit of 114 GeV on the SM Higgs boson mass [7].

As of December 2011, both the ATLAS and CMS collaborations have observed an excess of events in the low Higgs mass region ($\sim$125 GeV) [5, 6]. Neither experiment can make a definitive claim on discovery or exclusion until more data are collected in 2012.

1.2 Proton Collisions

Protons are composite structures that, at rest, are made up of three quarks, uud, held together by gluons. As protons are accelerated, such as in the LHC, additional quark-antiquark pairs accompanied by gluons appear within the proton (Figure 1.2). The three quarks at rest are called valence quarks, while the additional quark-antiquark pairs are called *sea*-quarks. Together, the valence quarks, sea quarks, and gluons are referred to as partons. In proton-proton (pp) accelerating machines, such as the LHC, hard scattering collisions occur between these constituent partons, rather than the protons themselves. The

exact energies of the incoming partons in pp collisions are not known on an event by event bases.

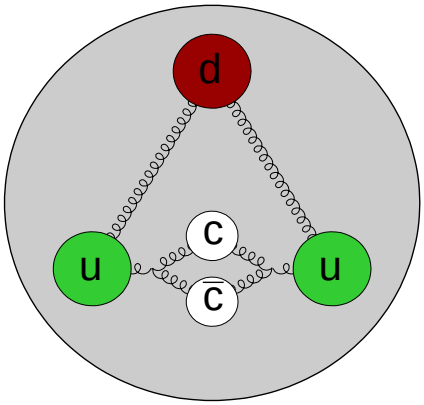

Figure 1.2: A diagram of a proton with its 3 valence quarks and an quark-antiquark pair.

A simple pp collision is depicted in Figure 1.3 where a valence u quark from one proton interacts with a valence d quark from the other proton. Assuming that the mass of incident partons is negligible compared to their energy (exact for gluons), we can write down the

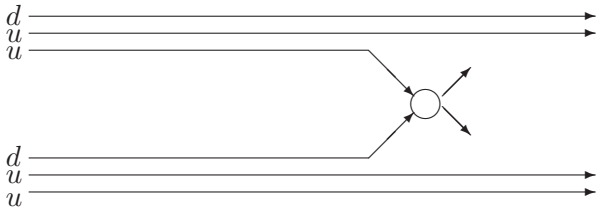

Figure 1.3: An example parton-parton collision where a valence u quark interacts with a valence d quark and produces X particles. In reality the incident protons will have any number of *sea*-quarks and gluons available for interactions.

4-vectors for generic incoming partons as[1]

$$p_1 = (x_1E, 0, 0, x_1E) \tag{1.2}$$

$$p_2 = (x_2E, 0, 0, x_2E), \tag{1.3}$$

$$\tag{1.4}$$

where x_i represents the fraction of the incident proton's energy the given parton has, and E is the energy of the beam[2]. The center of mass energy($\sqrt{s}$) of the parton-parton system can then be found:

$$s = E^2 - \vec{\mathrm{p}}^2 = 4x_1x_2E^2. \tag{1.5}$$

Thus the center of mass energy for each collision is dependent on the incident proton's parton distribution function (PDF). PDFs, $f_p(x, Q^2)$, are defined as the probability of finding a parton with momentum fraction x of a proton of momentum P at a momentum transfer[3] of Q^2. Each quark/gluon has its own PDF. PDFs will be discussed further in Chapter 4.

1.3 Tau Leptons

Tau leptons were discovered in events with the signature:

$$e^+ + e^- \rightarrow e^\pm + \mu^\mp + \geq 2 \text{ undetected particles} \tag{1.6}$$

which were detected at the Stanford Linear Accelerator Center-Lawrence Berkeley Laboratory in 1975 [8]. Precision measurements of the tau's mass, spin, and decay modes have been made at LEP, SLAC, and SPEAR.

1.3.1 Tau Properties

Tau leptons are the only leptons massive enough to decay hadronically. The mass of the tau lepton is 1776.84 MeV, its spin is $\frac{1}{2}$, and its proper lifetime is 2.906×10^{-13} s. All tau lepton decays occur through the weak interaction. Figure 1.4 depicts a tau lepton decaying

[1] ($\vec{\mathrm{p}}$, E)

[2] The LHC beam energy was 3.5 TeV during the 2010 and 2011 runs.

[3] For example, the momentum transfer for resonant Z production is the mass of the Z boson squared, ~ 8000 GeV^2.

to a virtual W boson which then decays leptonically $\sim 35\%$ of the time and hadronically $\sim 65\%$ of the time (Figure 1.5).

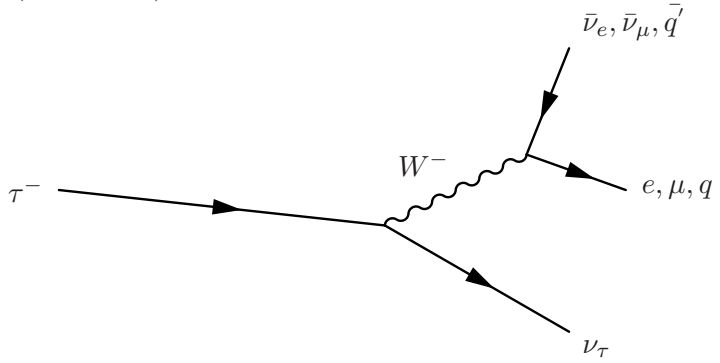

Figure 1.4: A Feynman diagram depicting the possible decay modes of the tau lepton.

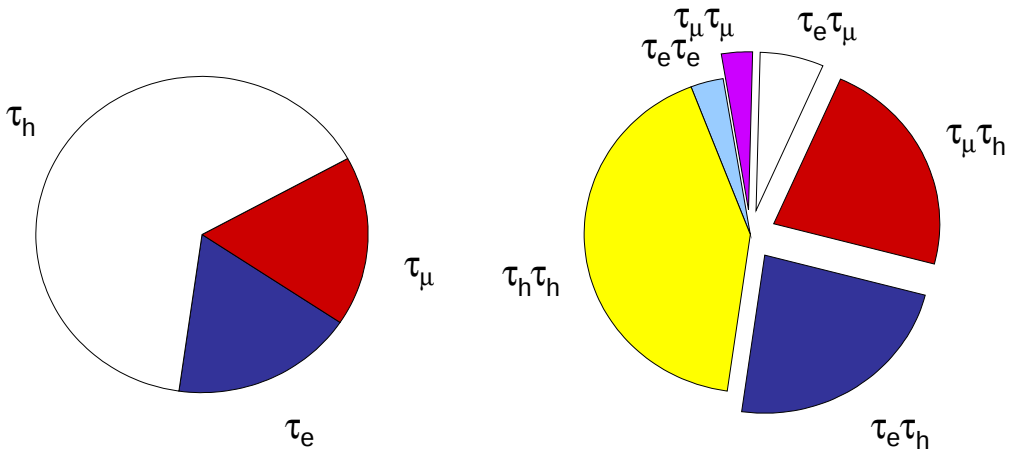

(a) (b)

Figure 1.5: The branching ratios for the tau lepton decay modes (left) and the ditau decay modes (right). The ditau decay modes studied in this analysis are slightly removed from the pie chart.

Tau leptons have a lifetime of $c\tau = 81.1$ μm which means that they generally decay before they can be directly observed. The hadronic decays, summarized in Table 1.1, will have final states with either one or three charged particles along with any number of neutrals[4].

[4]Five prong tau decays have been observed, however, their branching ratio is small and thus will not be

The majority of hadronic decays involve charged and neutral pions, with decays involving kaons making up $\sim 5\%$ of all hadronic decays.

Final State	branching ratio	resonance
All hadronic states	64.8%	-
All 1 prong states	49.5%	-
$\tau^- \to \pi^- \nu_\tau$	10.91%	-
$\tau^- \to \pi^- \pi^0 \nu_\tau$	25.12	$\rho(770)$
$\tau^- \to \pi^- \pi^0 \pi^0 \nu_\tau$	9.27	$a1(1260)$
All 3 prong states	15.18	-
$\tau^- \to \pi^- \pi^+ \pi^- \nu_\tau$	9.32	$a1(1260)$
$\tau^- \to \pi^- \pi^+ \pi^- \pi^0 \nu_\tau$	4.48	-

Table 1.1: Selected hadronic tau decay modes split between 1 prong and 3 prong final states. Modes with kaons in the final state ($\sim 5\%$) are not shown.

1.3.2 Taus in Higgs Boson Discovery

The partial width for Higgs bosons decaying to two fermions (f) is governed by [9]:

$$\Gamma(H \to f\bar{f}) = \frac{G_f m_f^2 m_H N_c}{4\pi\sqrt{2}}(1 - 4m_f^2/m_H^2)^{3/2} \tag{1.7}$$

where G_F is the Fermi coupling constant, m_f is the mass of the fermion, m_H is the Higgs mass, and $N_c = 1(3)$ for leptons (quarks). Since the Higgs coupling to leptons is approximately $\propto m_f^2$, the tau lepton is the only lepton that couples significantly to the Higgs boson.

Figure 1.6 plots the relative branching ratios of numerous decay modes of the Higgs boson as a function of the Higgs mass. Other than the $b\bar{b}$ final state, the ditau final state has the highest branching ratio in the mass range that has seen hints of signal. Fully understanding the $Z \to \tau\tau$ process provides a test-bed for discovery physics with a ditau

considered in this analysis.

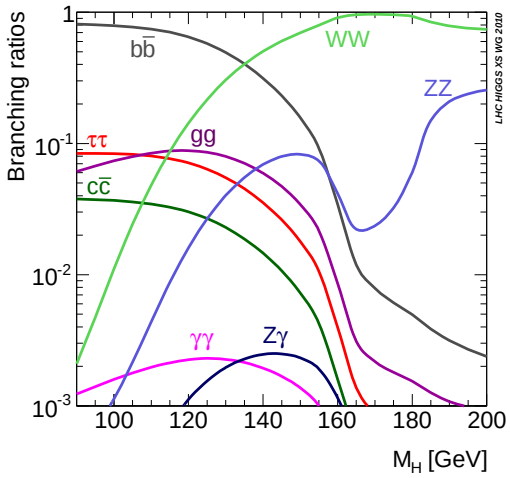

Figure 1.6: The low mass Higgs decay branching ratios [10].

final state; provides an unbiased measurement of the the tau trigger, reconstruction, and identification efficiencies; and provides a measurement of the hadronic tau energy scale.

1.4 Analysis Goals

Evidence for neutral weak currents was first observed in an electron neutrino scattering event by the Gargamelle bubble chamber in 1973 [11] and later confirmed with the observation of neutrino neutron scattering events [12, 13]. First direct evidence of the Z boson along with a measurement of its mass was made in 1983 by the UA1 and UA2 experiments at the Super Proton Synchrotron (SPS) [14, 15]. The discovery of the Z boson (along with the W a year before) provided definitive evidence for the electroweak model. Precision measurements of the Z boson including its mass and couplings were made by the four Large Electron-Positron Collider (LEP) experiments [16]. The first $Z \rightarrow \tau\tau$ cross-section measurements in hadron colliders were made by the CDF and D0 collaborations in the final state where one tau decays hadronically, while the other tau lepton decays to electrons (CDF) or muons (D0) [17, 18].

The leading order (LO), in α_s (the strong coupling constant), Feynman diagrams for Z and W boson production, at the LHC, are shown in Figure 1.7. The full Z boson cross-

section, over all orders of α_s, can be expressed as [19]:

$$\begin{aligned}\sigma(pp \to (Z \to f\bar{f}) + X) &= \sum_{a,b=q,\bar{q},g} \int dx_1 dx_2 f_{a/P}(x_1,\mu) f_{b/P}(x_2,\mu) \\ &\times \sigma(ab \to Z(\to f\bar{f})X),\end{aligned} \tag{1.8}$$

where the summation is over all types of incoming parton types, and the integral is over the parton momentum fractions. The theoretical prediction is primarily dependent on the order of $\sigma(ab \to Z(\to f\bar{f})X)$ and the experimentally measured proton PDFs. We will compare our measured cross-section with the next-to-next-to leading order (NNLO) calculation of $\sigma(ab \to Z(\to f\bar{f})X)$ [20].

The Z boson always decays to a pair of fermions whose partial widths are governed by [9]:

$$\begin{aligned}\Gamma(Z \to f\bar{f}) &= N_c \frac{\sqrt{2} G_F m_Z^3}{6\pi} \\ &\times [(T_3 - q \sin^2\theta_W)^2 + (qT_3 \sin\theta_W)^2]\end{aligned} \tag{1.9}$$

$$\tag{1.10}$$

where N_c is 3 for quarks and 1 for leptons, m_Z is the mass of the Z boson, q is the charge of the fermion, θ_W is the weak mixing angle, T_3 is the weak isospin ($\frac{1}{2}$ for charged leptons and d-type quarks and $-\frac{1}{2}$ for neutrinos and u-type quarks), and G_F is the Fermi coupling constant. The theoretical along with the measured branching ratios are presented in Table 1.2. In this analysis we will measure the cross-section when the Z boson decays to a pair of tau leptons which represents approximately 3.37% of all Z boson decays.

1.4.1 $Z \to \tau\tau$ Event Topology

Since the lifetimes of the Z boson and tau lepton are extremely short, we only see the decay products of the tau in the detector. $Z \to \tau\tau$ events can be classified based on how the two taus decay: to an electron and hadrons ($\tau_h\tau_e$), to a muon and hadrons ($\tau_h\tau_\mu$), to an electron and a muon ($\tau_e\tau_\mu$), to two electrons/muons ($\tau_e\tau_e/\tau_\mu\tau_\mu$), and to only hadrons ($\tau_h\tau_h$). The fully hadronic and dielectron channels were not fully considered in this analysis due to overwhelming backgrounds from either multijet events or $\gamma^*/Z \to ee$ events. Table 1.3 gives

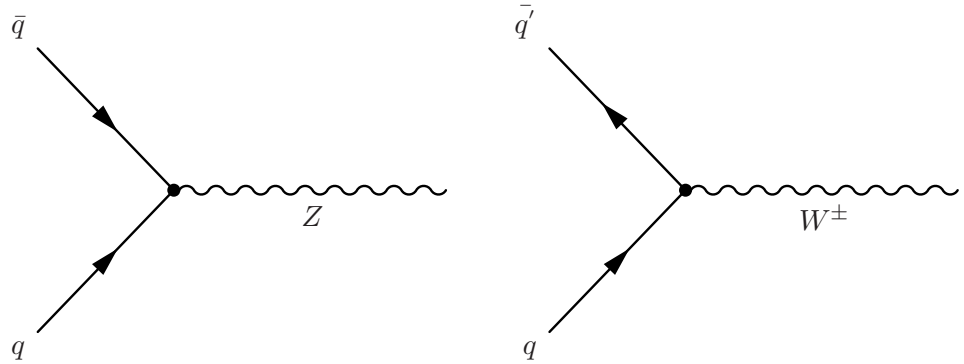

Figure 1.7: Tree level W/Z boson production Feynman diagrams for hadron-hadron collisions.

	$\Gamma(Z \to ff)/\Gamma(Z)$	
	Predicted (%)	Measured (%)
$u\bar{u}, c\bar{c}$	11.7	11.6
$d\bar{d}, s\bar{s}, b\bar{b}$	15.1	15.6
hadrons	68.8	69.9
$\nu\nu$	20.6	20.0
$\ell\ell$	10.5	10.1

Table 1.2: The predicted and measured branching ratios for Z bosons decaying to a pair of fermions is shown.

	$\Gamma(Z \to \tau\tau \to x_1x_2)/\Gamma(Z \to \tau\tau)$ (%)
$\tau^+\tau^-$	100
$\tau_h\tau_h$	42.0
$\tau_h\tau_e$	23.1
$\tau_h\tau_\mu$	22.5
$\tau_e\tau_\mu$	6.20
$\tau_e\tau_e$	3.19
$\tau_\mu\tau_\mu$	3.01

Table 1.3: The branching ratios for the six different ditau final states are shown relative to the branching ratio of $Z \to \tau\tau$. Z bosons decay to a pair of taus with a branching ratio of 3.37%.

the explicit branching ratios for the four final states with respect to the total $Z \to \tau\tau$ cross-section. In total, the four final states considered in this analysis represent approximately 55% of the total $Z \to \tau\tau$ cross-section.

The four final states considered in this analysis are depicted in Figure 1.8. The two semileptonic states ($\tau_h\tau_e$ and $\tau_h\tau_\mu$) have the signature of a isolated lepton (electron or muon) and a hadronic tau candidate. The two fully leptonic final states have a signature of two isolated leptons. In this analysis, unless explicitly stated, lepton will refer to either an electron or muon.

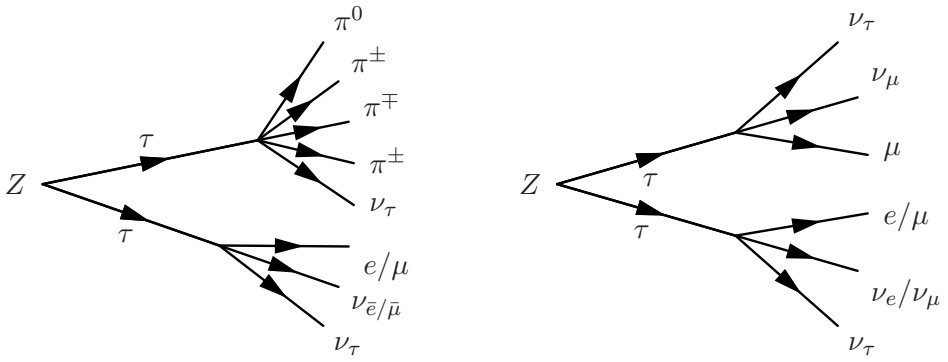

Figure 1.8: The four final states considered in this analysis are shown above. The two semileptonic final states are shown on the left while the two leptonic final states are shown on the right. The purely hadronic and dielectron final states are not considered.

A candidate $Z \to \tau\tau$ event display in the $\tau_h\tau_\mu$ final state is shown in Figure 1.9.

1.4.2 Summary

An introduction to the LHC and the ATLAS detector is presented in Chapter 2, followed by a description of the ATLAS trigger system in Chapter 3. Monte Carlo event generation is discussed in Chapter 4, while Chapter 5 discusses the techniques used to reconstruct the final physics objects used in the following analysis. The description of the analysis begins with the introduction and event selections in Chapter 6, followed by a description of the background estimation method in Chapter 7, and the final cross-section measurement in Chapter 8. The thesis concludes with a detailed description of all systematic uncertainties in Chapter 9, and a brief summary in Chapter 10.

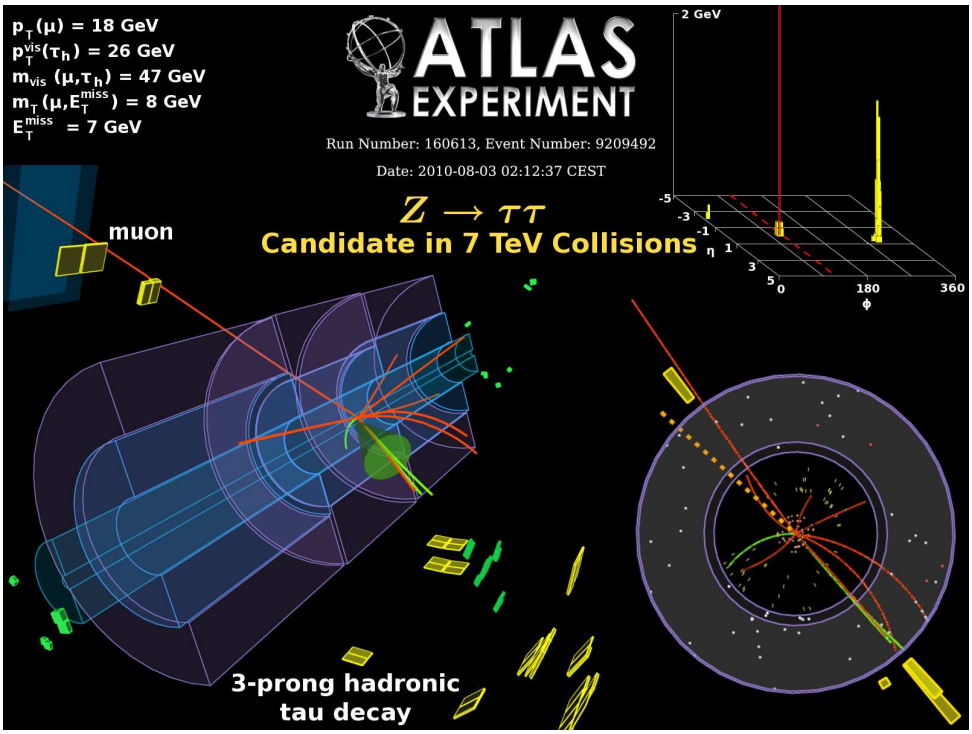

Figure 1.9: An example $Z \rightarrow \tau\tau$ Event Display in the $\tau_h\tau_\mu$ final state. The left sub-figure of the event display shows a three-dimensional view of the ATLAS detector, the upper right sub-figure shows an $\eta - \phi$ view of the calorimeter deposition, and the lower right sub-figure shows an $x - y$ view of the event. The muon candidate is marked and well isolated. The hadronic tau candidate has three associated, highly collimated tracks that are enclosed within a $\Delta(R)$ cone. There exists a forward track with momentum of 13 GeV whose invariant mass with the muon candidate is 21 GeV and has the same sign as the muon candidate. Kinematic quantities of the τ_h, τ_μ, and the overall event are shown in the upper left part of the figure.

Chapter 2

THE LHC AND ATLAS

2.1 The Large Hadron Collider

The Large Hadron Collider (LHC) is a 26.7 km superconducting hadron accelerator ring designed to collide protons at center of mass energies (CM) energies up to 14 TeV and at instantaneous luminosities of $10^{34}\text{cm}^{-2}\text{s}^{-1}$ [21]. The data used in this analysis was produced by LHC collisions with CM energies of 7 TeV at a peak instantaneous luminosity of $\sim 2 \times 10^{32}\text{cm}^{-2}\text{s}^{-1}$. The number of events for a given process with cross-section, σ_{process}, and total integrated luminosity, $\mathcal{L}^{\text{int}}$, is:

$$N_{\text{events}} = \sigma_{\text{process}} \times \mathcal{L}^{\text{int}}. \tag{2.1}$$

Thus, since the cross-section of a given process increases with CM energy, the unprecedented energies and luminosities at the LHC allows for the most competitive probing of new physics.

Instantaneous luminosity ($\mathcal{L}$), the number of particles per unit area per unit time, at a colliding experiment can be approximated as:

$$\mathcal{L} = \frac{f_{\text{col}} N_1 N_2}{A}, \tag{2.2}$$

where f_{col} is the frequency at which collisions can occur, A is the cross-section of the beam, and N_i represents the total number of available protons in each beam at the time of collision. In order to maximize the luminosity, the LHC needs to maximize the collision frequency and the number of available protons per collision while minimizing the cross-sectional area of the beam at the point of collision.

The protons in the LHC are supplied by a specific injection chain: First, protons are accelerated to an energy of 50 MeV in the Linac2 linear accelerator; second, protons are accelerated in the Proton Synchrotron Booster (PSB), the Proton Synchrotron (PS), and the Super Proton Synchrotron (SPS) to an energy of 450 GeV before being injected into

the main LHC synchrotron accelerator (Figure 2.1). Protons in the LHC are circulated for approximately 20 minutes in the "beam ramping" process from 450 GeV to 3.5 TeV. Once the beams reach the desired energy, a physics fill occurs in which the detectors are able to record data.

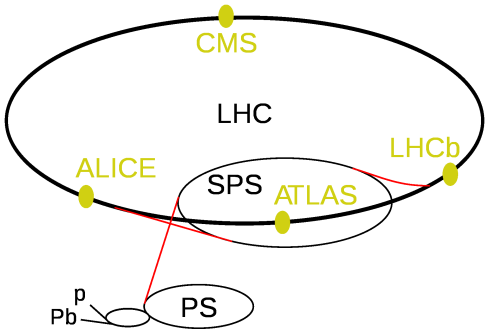

Figure 2.1: The full injection chain for protons circulating the LHC.

The LHC, along with the PSB, PS, and SPS, are synchrotron accelerators. Synchrotrons are accelerators that employ oscillating electric fields to increase the momentum of particles along the beam axis, and magnetic fields to both bend the particles around the ring and to focus the beams. The LHC consists of 8 octants; four of the octants are reserved each for the four detectors, two octants are reserved for beam cleaning, one for the beam Radio Frequency (RF) resonant cavities, and one for beam dumping (Figure 2.2).

Protons entering the resonant cavity are accelerated as they pass a potential difference created by a gap between two electrodes. A particle, with charge q, experiencing a maximum potential difference, V, will experience a change of potential energy:

$$\Delta(U) = qV\sin(\phi) \tag{2.3}$$

where ϕ is a phase angle defined as:

$$\phi = f_{\mathrm{rf}} t_0 + \pi/2, \tag{2.4}$$

where f_{rf} is the frequency of the RF power source and t_0 is the time the proton enters the gap. Due to the oscillating nature of the electric-field, a uniform beam of protons entering

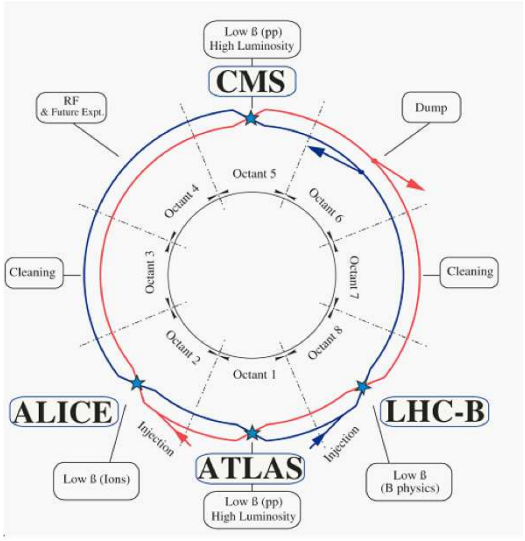

Figure 2.2: Visual schematic of the different octants of the LHC.

the gap will, depending on the time that they enter, either be accelerated or decelerated into groups of particles referred to as bunches. In order to ensure that these bunches always enter the gap at a time corresponding to maximal acceleration, the frequency of the RF power source must be an even multiple of the frequency in which particles circulate the synchrotron (f_{s}):

$$f_{\mathrm{rf}} = h f_{\mathrm{s}}, \tag{2.5}$$

where h is called the harmonic number of the synchrotron. The harmonic number thus dictates the number of possible bunches that are allowed to be simultaneously accelerated in a beam.

In the LHC, the RF frequency is 400.8 MHz and the frequency of the accelerator is $\sim$1100 Hz[1] ($c/26.7 \times 10^3$ m) making the harmonic number 35640. Each of the potential h proton bunches are typically referred to as buckets, where as the bunches refer to buckets filled with protons. The bucket spacing at the LHC is 2.5 ns ($1/f_{\mathrm{rf}}$), while the nominal spacing between proton bunches is never less than[2] 25 ns. At collision energy, the bunch

[1]The speed of light, c, in a vacuum is $3{\times}10^8$ m/s.

[2]Currently the bunch spacing is never less than 50 ns.

length will be 1.06 ns. At peak LHC luminosity, there will be 2808 proton bunches each with an intensity of 1.15×10^{11} protons. More beam parameters are shown in Table 2.1.

In order to increase the cross-sections of new physics processes, the LHC needs to maximize the energy of each incoming proton beam. As the energy of the protons increase, so does the energy required to bend the protons back to the RF cavity. By equating the Lorentz force on a single proton with its centrifugal force, the magnitude of the magnetic field required to bend the particles can be computed as:

$$\begin{aligned} B &= \gamma mc/(qeR) \\ &= (P/c)/(qR); \text{ momentum } (P) \text{ in eV, } c \text{ and } R \text{ in SI units.} \end{aligned} \tag{2.6}$$

One finds, plugging in the effective radius of the LHC (R), the mass of the proton, and the relativistic[3] γ, that a magnetic field of 8.3 T is required. Producing magnetic fields of this magnitude is one of the limiting factors in the energy attainable by accelerators in general.

In order to maximize the number of available particles per collision, the LHC chose to collide protons with protons rather than protons with hard to produce anti-protons such as at the Tevatron. The Lorentz force bending the particles around the ring is:

$$\vec{F} = q\vec{v} \times \vec{B} \tag{2.7}$$

where q is the charge of the particle, v is the particles velocity and direction, while B is the magnitude and direction of the magnetic field. The Tevatron had the advantage that, with one magnetic field, the direction of the Lorentz force was always in the same direction for the proton and anti-proton beams since both the direction and charge of the particles were opposite each other. The LHC, however, cannot depend on this natural cancellation. To further complicate matters, the physical space within the LHC tunnels is not sufficient to house two sets of dipole magnets. Special dipole magnets, twin bore dipole magnets, are used to provide a magnetic field with opposing directions for each proton beam while housing the two beam pipes within one support structure.

In addition to the dipole magnets used to steer the beam around the accelerator, quadrupole magnets and collimators are also used to combat the natural tendency of bunches

[3]The relativistic factor, γ can be expressed as $1/\sqrt{1-v^2/c^2}$ or in terms of energy and mass $E = \gamma mc$.

of like signed particles to drift apart, and focus the beams in order to minimize the cross-sectional areas of the beams at the point of collision. In all, the LHC contains 1232 dipole magnets, 858 quadrupole, and numerous higher order magnets.

	Unit	Injection Energy 450 GeV	Collision Energy 7 TeV
Circumference	km	27.6	27.6
Bucket spacing	ns	2.5	2.5
Bunch length	ns	1.71	1.06
Intensity per bunch (N)	10^{11} p	1.15	1.15
Number of bunches (n_b)		2808	2808
Normalized rms transverse emittance (ϵ_n)	μm	3.75	3.75
Synchrotron radiation (loss/turn)	keV	-	7
Magnetic Field Strength	T	0.5	8
Harmonic Number		35640	35640
Machine frequency (f_{LHC})	Hz	11200	11200
RF Frequency	MHz	400	400
Energy gain / revolution	keV	485	485
Effective Radius	m	2804	2804
Relativistic γ factor		480	7460
Beta function at IP ($\beta*$)	m		0.55

Table 2.1: Basic parameters of the LHC both at injection (450 GeV) and at peak energy (7 TeV) [21]. The quoted $\beta*$ value is the ideal value which will attain the design luminosity of $10{\times}10^{34}\mathrm{cm}^{-2}\mathrm{s}^{-1}$.

Now that we better understand the main parameters of the LHC, we can revisit equation 2.2 and recognize that the collision frequency is simply the frequency of the LHC multiplied by the number of filled proton bunches (n_b). In addition, the number of protons available per collision, N_i, is the number of protons per bunch. We can then write the cross-section of the collision either in terms of the widths of the individual beams, $A = 4\pi\sigma_x\sigma_y$,

or in terms of LHC beam parameters: the normalized transverse beam emittance[4], ϵ_n, and the β function at the interaction point[5] ($\beta*$). Putting together the LHC beam parameters leads to [21]:

$$\mathcal{L} = \frac{f_{\mathrm{LHC}} n_b N_1 N_2 \gamma_p}{4\pi\epsilon_n \beta*}. \tag{2.8}$$

Figure 2.3 shows a plot of the integrated luminosity delivered by the LHC and collected by the ATLAS detector as a function of day of the year. The discrete increases in the luminosity correspond to the introduction of extra colliding bunches, more protons per bunch, and/or the squeezing of the proton beams. At the beginning of data taking in 2010, the instantaneous luminosity increased from $1.1 \times 10^{27}\mathrm{cm}^{-2}\mathrm{s}^{-1}$ to $2.3 \times 10^{32}\mathrm{cm}^{-2}\mathrm{s}^{-1}$ or by a factor of 200,000. The instantaneous luminosity has since increased further to $3 \times 10^{33}\mathrm{cm}^{-2}\mathrm{s}^{-1}$ in 2011.

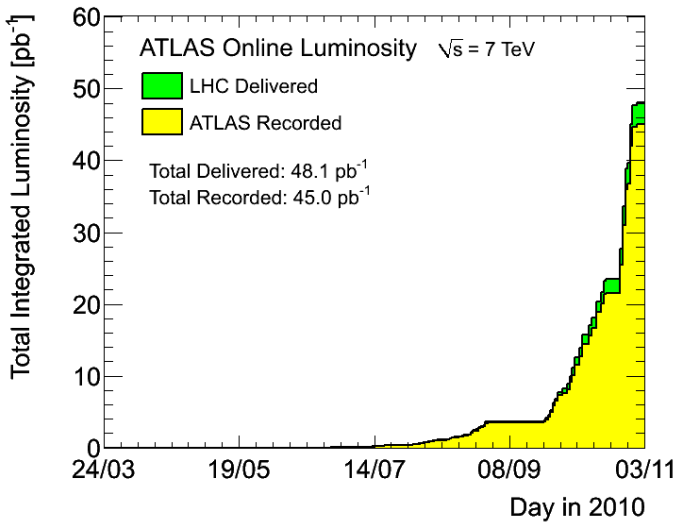

Figure 2.3: The total integrated luminosity delivered by the LHC and collected by the ATLAS detector during 2010. The x-axis displays the day/month in the year 2010.

[4]Transverse beam emittance is the minimum opening in which all or a certain percentage of the beam can be squeezed through.

[5]The beta function is a measure of the amplitude modulation of the beam due to the focusing quadrupole magnets [22]. $\beta*$ is the value of the beta function at the interaction point.

2.2 The ATLAS Detector

The ATLAS detector was optimally designed in order to perform precision physics in the demanding LHC environment.

The ATLAS coordinate system is defined with the positive z-axis pointing along the beam axis (counter clockwise), while the positive x-axis points towards the center of the ring, and the positive y-axis points straight upwards toward the sky. The radial distance, R, is defined as the distance projected onto the transverse $(x-y)$ plane to the origin, while the azimuthal angle, ϕ is defined as the angle between R and the positive x-axis. The polar angle, θ, is defined as the angle between the positive z-axis and a point. Rather than using θ directly, the invariant quantity rapidity[6] (y) is used to measure the component of a particle along the z-axis. In the limit that the mass of the particle is small (m$\ll$E), pseudorapidity (η) approximates the rapidity and is defined as:

$$\eta = -\ln(\tan(\frac{\theta}{2})) \tag{2.9}$$

Many sub-detectors in the ATLAS detector are composed of a cylindrical barrel region concentric with the beam pipe at low pseudorapidity and two sets of end-cap disks at high pseudorapidity. The exact boundaries in pseudorapidity depend on the specific sub-detector and are referred to as overlap/transition regions.

The ATLAS detector has three main components: the Inner Detector, composed of three sub-detectors designed to reconstruct tracks of charged particles up to $|\eta| < 2.5$ and resolve their interaction vertices; the Calorimeter System, designed to reconstruct clusters of charged and neutral particles out to $|\eta| < 4.9$ in order to measure jets and the missing transverse energy[7] $(E_{\mathrm{T}}^{\mathrm{miss}})$; and the Muon System, designed to measure, in conjunction with the Inner Detector, muon tracks out to $|\eta| < 2.4$. A 2 T magnetic solenoid is situated between the Inner Detector and the calorimeters, while a barrel toroid and two endcap

[6] $y = -\frac{1}{2}\ln\frac{E+p_z}{E-p_z}$

[7] The transverse missing energy is measured by vectorially summing all energy transverse to the beam. Since the initial energy transverse to the beam is zero, any excess transverse energy measured after the collision is caused by particles that do not (or rarely) interact with ordinary matter such as neutrinos. The total missing energy cannot be measured, because the initial energy in the beam direction is not known.

toroid magnets are placed within the Muon System. The three detector sub-systems are discussed in more detail in Sections 2.2.1, 2.2.2, and 2.2.3. An overview of the ATLAS detector is depicted in Figure 2.4.

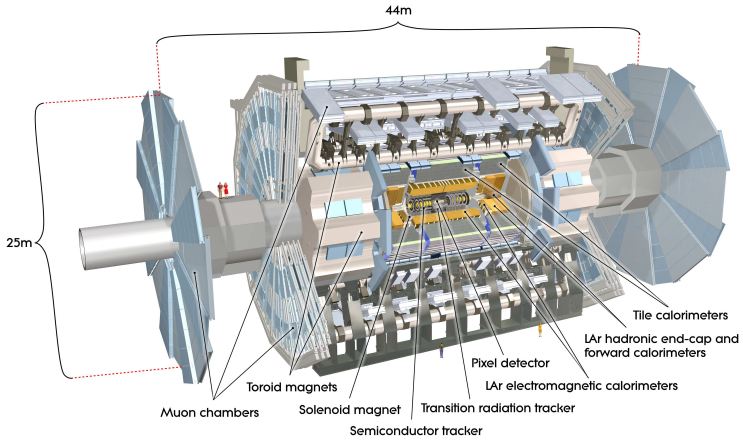

Figure 2.4: The ATLAS detector is composed of three main parts. The Inner Detector contains three tracking sub-detectors: the pixel, SCT, and TRT straw tube detectors. The Inner Detector is surrounded by the solenoid magnet followed by two calorimeter detectors. The Muon system along with the toroid magnets, make up the outer most parts of the ATLAS detector.

2.2.1 The Inner Detector

The Inner Detector (ID) extends out to 1.2 m in R and 3.5 m in z and is composed of the pixel detector, the silicon microstrip semi-conduction tracker (SCT), and the Transition Radiation Tracker (TRT). The primary goals of these three technologies are to reconstruct tracks that charged particles traverse starting from the Interaction Point (IP) to the inner face of the calorimeter. At design luminosity ($10 \times^{34}$ cm^{-2}s^{-1}) approximately 1000 tracks per bunch crossing (25 ns) are expected [23] creating a very challenging environment for the ID. In order to accurately reconstruct the tracks and the primary vertices, high precision and a very fine granularity are required. The ID is depicted in Figure 2.5.

The pixel detector lies at the innermost part of the ID and has both a barrel component of three concentric layers and an endcap component comprising three disks. The sensitive

region ranges from $50.5 < R < 122.5$ mm in the barrel and $88.8 < R < 149.6$ mm in the endcap, while the sensitive component along z extends to 400.5 mm in the barrel and to 650 mm in the endcap. The detecting elements are the 50x400 μm ($\phi \times z$) pixel sensors which give resolutions of 10 μm ($R - \phi$) and 115 μm (z) in the barrel 10 ($R - \phi$) and 115 μm (R) in the endcap. In all, there are approximately 80.4 million readout channels.

The SCT detector surrounds the Pixel detector and comprises 4 cylindrical layers in the barrel and 9 disks in each endcap. The sensitive region of the barrel extends from $299 < R < 514$ mm and $0 < |z| < 749$ mm, while the endcap extends from $275 < R < 560$ mm and $839 < |z| < 2735$ mm. The typical detector element has a length of 6.4 cm and a pitch of 40 μm. In order to gain a handle on the z coordinate of the track, each layer has two sets of strips: one parallel with the beam axis, and the second set at a 40 mrad offset. The endcap disks each have a set of strips pointing out radially and a set also at a 40 mrad offset in order to gain a handle on the R coordinate of a hit. The SCT has approximately 6.3 million readout strips yielding an accuracy of 17 μm$(R - \phi)$ in both the barrel and endcap and 580 μm (z) in the barrel and 580 μm(R) in the end-caps.

The last region of the ID consists of the TRT which has a sensitive barrel region consisting of 73 straw planes extending from $563 < R < 1066$ mm and $0 < |z| < 712$ mm and 160 straw planes in the endcap extending from from $644 < R < 1004$ mm and $848 < |z| < 2710$ mm. The detecting element, the straw, is approximately 144 cm long and 4 mm in diameter. Due to the layout of the TRT, only ($R - \phi$) measurements are made with an accuracy of 130 μm per tube. Radiators are interleaved in the straw tube chambers causing low mass particles to radiate photons. These photons are absorbed in the Xe gas mixture within each tube yielding hits with higher amplitudes. These hits are then interpreted as either low or high threshold in the front-end electronics resulting in electron/pion separation [24].

2.2.2 The Calorimeter

The ATLAS calorimeter has full azimuthal coverage and pseudorapidity coverage up to $|\eta| < |4.9|$. This is needed in order to discover new physics with multijet or high $E_{\mathrm{T}}^{\mathrm{miss}}$ signatures. The calorimeter has three main components: the electromagnetic (EM) calorimeter used

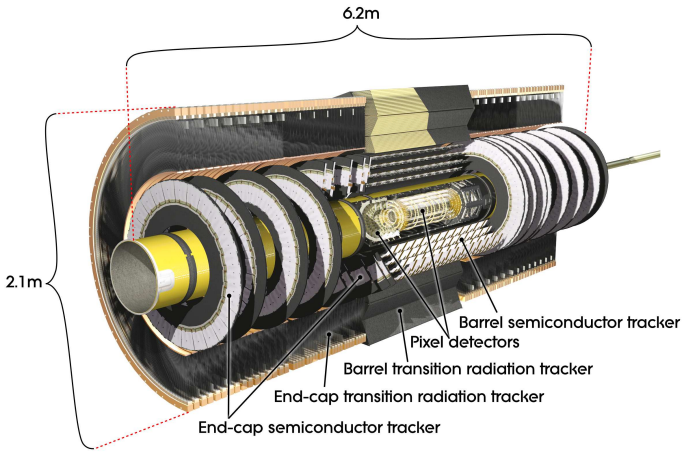

Figure 2.5: The inner-most part of the ATLAS detector is composed of three tracking technologies from inner-most: the pixel detector, the semi-conducting tracker, and the transition radiation tracker.

to measure the energy of electrons and photons, the hadronic (HAD) calorimeter used to measure the energy of hadrons, and the forward calorimeter (FCal) which is used to measure the energy of electrons, photons, and hadrons at high pseudorapidity. The calorimeter systems are located beyond the solenoid magnetic field and before the Muon Spectrometer (MS) and toroidal magnets. The calorimeter is shown in Figure 2.6.

The EM-calorimeter is a lead-liquid-Argon (LAr) sampling calorimeter that is separated into a barrel portion (EMB), $|\eta| < 1.475$, and an endcap portion (EMEC), $1.375 < |\eta| < 3.2$. In the region of precision physics, $|\eta| < 2.5$, the barrel and endcap contain 3 layers of active material, while the rest of the EM-calorimeter has two layers with a less fine granularity sufficient for measuring jets and $E_{\mathrm{T}}^{\mathrm{miss}}$. In order to correct for the energy lost by electrons and photons upstream of the calorimeter, a presampler is installed for $|\eta| < 1.8$. The EM calorimeter has nearly 64k channels, has a typical depth between 22 and 33 radiation lengths, and has an average energy resolution $\sigma_E/E = 10\%/\sqrt{E[\text{ GeV}]} \pm 0.7\%$ [23].

The HAD calorimeter comprises a barrel ($|\eta| < 1.0$), an extended barrel ($0.8 < |\eta| < 1.7$), and two end-caps ($1.5 < |\eta| < 3.2$). The two barrel components use steel as the absorber and scintillating tiles as the active material, while the endcap, like the EM calorimeters, is a LAr sampling calorimeter. The HAD calorimeter has over 15k channels and has an average

energy resolution of $\sigma_E/E = 50\%/\sqrt{E[\text{ GeV}]} \pm 3\%$.

Each Forward calorimeter has three modules, with the first module, made of copper, optimized for electron/photon measurements, while the other two modules, made of tungsten, are optimized for the detection of hadronic jets. Together, the three modules extend the pseudorapidity range of the calorimeter out to $|\eta| < 4.9$. The Forward calorimeter has approximately 3.5k channels, has an average depth between 7 and 9 interaction lengths, and has an average energy resolution of $\sigma_E/E = 100\%/\sqrt{E[\text{ GeV}]} \pm 10\%$.

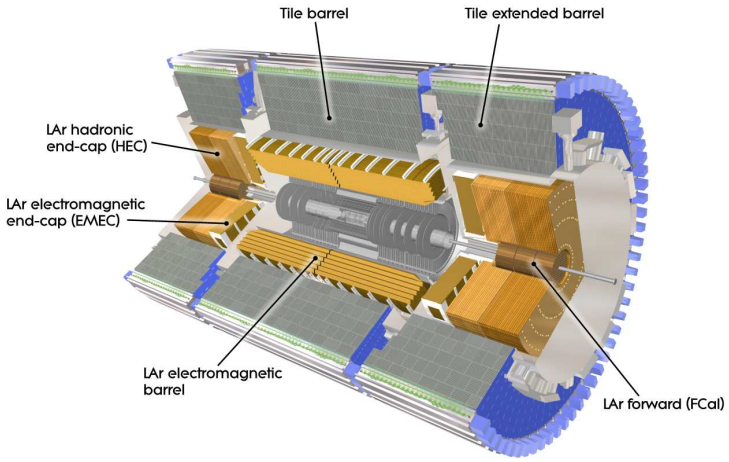

Figure 2.6: The calorimeter system is made up an electromagnetic and hadronic calorimeter.

2.2.3 The Muon System

The Atlas Muon System is capable of performing precision tracking out to $|\eta| < 2.7$ and triggering on muons out to $|\eta| < 2.4$. The Muon Spectrometer is split into a barrel component ($|\eta| < 1.05$) and two endcap components ($|\eta| > 1.05$). The magnetic field is provided by the barrel toroid in the region $|\eta| < 1.4$ and two endcap toroidal magnets at $|\eta| > 1.6$. The region $1.4 < |\eta| < 1.6$ is generally known as the transition region where the total magnetic field is influenced by both the barrel and endcap toroids. Four detector technologies are employed in the Muon Spectrometer. Two precision measurement technologies: the Monitored Drift Tube (MDT) chambers and Cathode Strip Chambers (CSCs), along with

two triggering technologies: the resistive plate chambers (RPCs) and the thin gap chambers (TGCs). The Muon Spectrometer is shown in Figure 2.7.

The MDTs are stationed throughout the barrel and the endcap out to $|\eta| < 2.7$, except in the innermost wheel ($|\eta| > 2.0$) of the endcap where rates are expected to be the highest. All MDTs are organized in chambers that generally consist of 6-8 layers of tubes arranged orthogonal to the beam in the barrel and in the endcap. There are three layers of chambers in the barrel and endcap, except in the innermost layer of the endcap, providing on average approximately 18-20 hits per track. The main detecting element is the drift tube, which is a pressurized 3 cm diameter tube containing primarily Ar and CO_2 with an anode wire at 3080 V at the center. Muons traversing a tube will ionize the gas mixture causing an avalanche of electrons to drift to the anode wire. By measuring the minimum time it takes for electrons to drift towards the anode and an understanding of the r (distance) vs t (time) relationship of the gas in the tube, the distance of closest approach of the muon to the anode can be measured with an accuracy of $z < 10$ μm. Due to the layout of MDTs, only the z/η coordinate can be measured with high precision; the ϕ measurements are taken from the trigger chambers, when available.

CSCs are used for precision track measurements within $2.0 < |\eta| < 2.7$ in the inner wheel of the endcap, since they perform better in higher rate environments [23]. The CSCs are multiwire proportional chambers that provide both an η and ϕ measurement. Each CSC disk, one per endcap, are segmented into 16 chambers where each chamber is composed of 4 planes yielding 4 measurements per track. The anode wires are oriented radially out from the beam pipe, while the cathode strips are segmented either perpendicular (R) or parallel (ϕ) to the anode wire yielding a resolution of approximately 40μm in R and 5mm in ϕ.

The RPC and TGC chambers provide valid Level 1 Trigger objects (Sec. 3) by simultaneous coincidence requirements in both the η and ϕ projections, and also provide the precision ϕ measurement. The RPC is located in the barrel and has an effective trigger coverage out to $|\eta| < 1.05$, while the TGC is located in the end-caps and has a trigger coverage of $1.05 < |\eta| < 2.4$. The RPC has three layers: the first two layers sandwich the middle layers of the MDT, while the outer layer is located past the outer layer of the MDT chambers. The TGC is segmented into four layers in increasing z: the first layer is situated

directly in front of the innermost MDT/CSC wheel, while the other layers are directly in front of and behind the middle endcap MDT chambers.

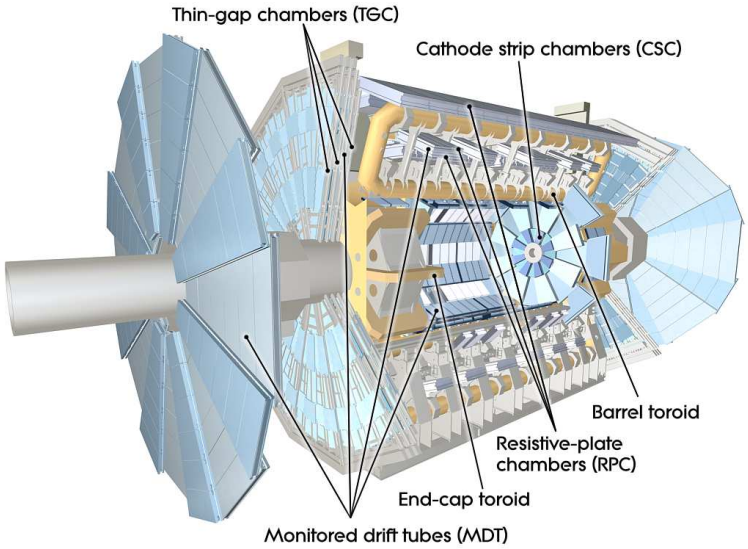

Figure 2.7: The muon system consists of MDT chambers in the barrel and endcap for precision measurements with RPC and TGC trigger chambers in the barrel and endcap respectively. In the forward regions, CSC chambers are used instead of the MDTs.

Chapter 3

ATLAS TRIGGER SYSTEM

At nominal LHC machine conditions the spacing between proton bunches is 25 ns producing an event rate of 40 MHz. The actual cross-section for inelastic proton proton collisions at design energy is 80 mb, which corresponds to an event rate of 1 GHz, which in turn means that there are on average 23 collisions per bunch crossing [23]. With an average event size of 1.3 Mbytes, the storage of all interactions would require writing more than one peta byte of data every second. Most of these events, however, are uninteresting minimum-bias (min-bias) interactions. Min-bias events refer to a class of collisions that has no (minimum) selection bias. Such events will include diffractive events, collisions in which the protons do not fragment upon collision, and non-diffractive events, collisions in which the protons do fragment upon collision. These min-bias events are considered uninteresting since we do not expect to find new physics in these events, however, an understanding of these events is vital in Monte Carlo Simulation (Section 4.2). The ATLAS trigger system is designed to both select only interesting events, and to reduce the overall rate to a manageable 200 Hz. In order to achieve this goal, the ATLAS trigger system is comprised of 3 levels: L1, L2, and the event filter.

The L1 trigger makes fast hardware decisions (2 μs) to reduce the overall event rate to approximately 75 kHz using subsets of the calorimeter and muon sub-detectors. The L1 trigger attempts to identify high p_{T}[1] particles such as muons, electrons, photons, jets, and hadronic taus, along with events with large $E_{\mathrm{T}}^{\mathrm{miss}}$. These particles are identified in a small η by ϕ window of the detector, known as a region of interest (ROI).

Events with one or more ROIs are stored in a buffer and are further processed by the L2 trigger. The L2 trigger is a software-based trigger that unpacks the information in

[1]The transverse momentum (p_{T}) of a particle is its momentum transverse to the direction of the beam ($\pm z$). $p_{\mathrm{T}} = p\,\sin(\theta) = \sqrt{p_x^2 + p_y^2}$.

interesting ROIs and is required to make a decision on the order of 40 ms. The L2 trigger further reduces the event rate from 75 kHz to 3.5 kHz.

Events that pass the L2 trigger are finally analyzed with the event filter. The event filter has access to the entire data record of the event and makes a decision on whether to write the event to disk on average in 4 s. The final event rate after all three trigger systems is 200 Hz. In general, the event filter attempts to fully emulate offline reconstruction (Section 5).

Chapter 4

MONTE CARLO GENERATION

Predicting the energy loss and decays of particles as they pass through and interact with matter in a deterministic fashion is exceedingly difficult. Instead, the behavior of particles are analyzed using a set of deterministic and stochastic processes [25]. This method is better known as the Monte Carlo (MC) method. Having a Monte Carlo (MC) theoretical prediction is necessary in order to understand the magnitude and shape of our backgrounds, as well as understanding how efficient/inefficient our analysis is in selecting signal events and rejecting background events. In order to trust the results of our MC prediction, we must ensure that it models how true physics processes behave in the ATLAS detector as best as possible. To achieve this goal, we generate MC events in three main steps: generate a hard scattering parton-parton event, simulate how the products of the hard scatter will interact with the active elements and dead material in our detector, and finally convert the simulated hits into raw digitized detector hits. The last step produces an event in the same form as an event coming from the ATLAS data acquisition system. Thus, after digitization, we can run the exact same reconstruction algorithms as on real data events. Figure 4.1 depicts the three steps of MC production.

4.1 Parton Distribution Functions

Since the momentum of incident protons in pp collisions is shared between its constituent partons, one needs a prediction of the incoming parton's momentum fraction of the proton in order to generate realistic events. To this end, parton distribution functions (PDF)s are used to predict the given fraction of momentum (x_a) a parton type ($a = q, g$), will have of the incident proton at momentum transfer Q^2:

$$f_a(x_a, Q^2). \tag{4.1}$$

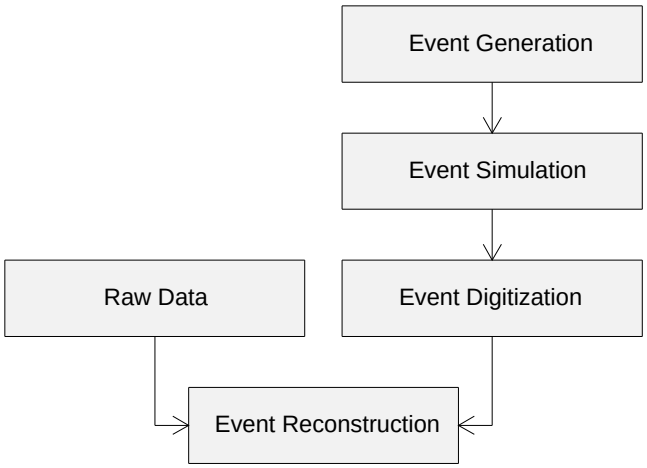

Figure 4.1: The MC production begins with event generation, followed by event simulation and digitization. Following event digitization, the MC event is reconstructed as if it were a normal data event.

Each parton type, a, has its own distribution function. Since PDFs cannot be determined solely on theoretical grounds, experiments are used to predict them. Deep inelastic electron-proton scattering at HERA (and fixed target experiments) provided a direct probe into the structure of the proton up to momentum transfer squared values of 10^4 GeV^2. PDFs are fitted to experimental data, and then perturbative QCD is used to extrapolate the results to higher center of mass energies and momentum transfers [26, 27, 28]. An example of the parton distributions produced by the `MSTW` collaboration at leading order, are shown in Figure 4.2.

4.2 Event Generation

Event generation is the process of simulating the hard scattering hadron-hadron collisions in accordance with theoretically calculated production cross-sections. In addition to the hard scattering process, any quarks or gluons produced from initial and final state radiation parton showers are hadronized into semi-stable mesons which can then be observed in the detector. In physics processes, both stable and unstable particles will be produced. A

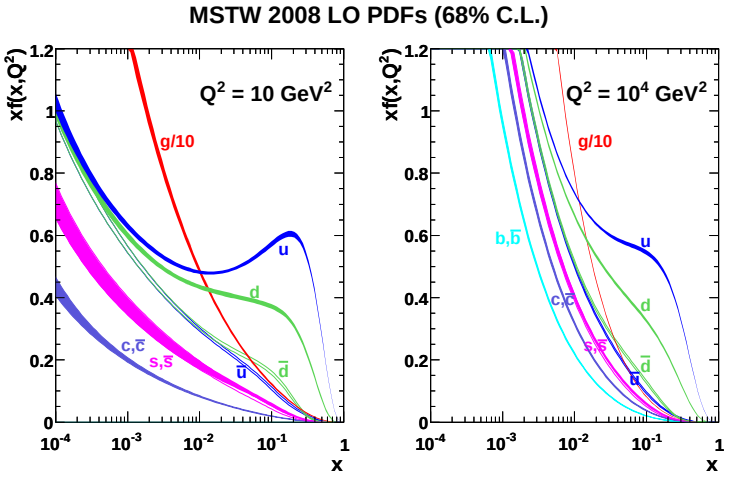

Figure 4.2: Example leading order (LO) parton distribution functions (PDFs) are shown at momentum transfers of 10 GeV^2 (left) and 100 GeV^2 (right) by the MSTW collaboration [29]. The PDFs used to reconstruct the MC signal events in this analysis were produced by the same collaboration (MRST) and modified at leading order.

particle is generally considered to be stable (i.e., e, μ, $\pi^{\pm}$, $k^{\pm}$, ...) if its[1] $c\tau > 10$ mm and unstable (i.e., τ, W, Z, ...) otherwise [30]. The event generator will generate the 4-vectors for all unstable particles, and decay these particles, and any subsequent unstable particles, until only stable particles remain. These four vectors, for stable particles, are further processed by the detector simulation. In addition to the hard scatter, event generators are also responsible for simulating the underlying event and pileup interactions (Section 9.1).

The three event generators used in this analysis are `PYTHIA` [31], `MC@NLO` [32], and `HERWIG` [33]. In addition, specialized event generators are interfaced with the three event generators in order to perform the decay of the tau lepton (`TAUOLA` [34]) or electromagnetic radiation (`PHOTOS` [35]). PDF sets must also be supplied to the event generators. All W/Z boson physics processes used modified leading order PDF sets (`MRSTLO*` [36]), while `CTEQ6.6` [37] NLO order PDF sets were used for the $t\bar{t}$ sample. The underlying event is further tuned to early min-bias event measurements with the ATLAS detector [38] (`ATLAS`

[1] τ is the mean lifetime of a particle. $c\tau$ is then the mean distance that a particle can travel before it subsequently decays.

MC tune).

4.2.1 PYTHIA

The PYTHIA event generator produces hard scatter events at leading order. In order to approximate higher order processes, PYTHIA adds in QCD and QED radiation in its parton showering model. In general, the parton showering approximation of higher order processes is successful at predicting the substructure of jets, but is poorer at predicting the rate of well separated jets [31]. If other generators are used to simulate the hard process to higher orders in perturbative QCD, then PYTHIA (or HERWIG) may still be used to perform the parton showering. The inclusive W and Z MC samples are fully generated with PYTHIA.

4.2.2 HERWIG

Like PYTHIA, HERWIG also generally only computes the leading order matrix elements for the hard scattering event and depends on parton showering to simulate higher orders of QCD. When used solely as a parton showering program interfaced with a generator that computes higher orders of QCD perturbation, such as MC@NLO, HERWIG will match each parton shower with first order matrix elements in order to avoid double counting. HERWIG was used to produce all three diboson samples used in this analysis.

4.2.3 MC@NLO

Unlike HERWIG and PYTHIA, MC@NLO, as its name implies, is capable of including next-to-leading order matrix elements in the hard physics process [39]. The MC $t\bar{t}$ background sample is produced with the MC@NLO event generator interfaced with HERWIG for the parton showering. It was found that the resulting top transverse momentum distribution is produced better with MC@NLO than either HERWIG or PYTHIA [30].

4.2.4 TAUOLA *and* PHOTOS

TAUOLA and PHOTOS are specialized generators that simulate the decay of the tau lepton and the emission of final state QED photons, such as bremsstrahlung radiation, respectively.

These generators are interfaced with a generator, such as PYTHIA, that produces the hard scattering event. In the case of $Z \rightarrow \tau\tau$ events generated by PYTHIA, the tau leptons, although unstable ($c\tau = 10\ \mu$m), are left undecayed and are then fed to TAUOLA. TAUOLA is capable of generating more than twenty different tau decays. In the case of leptonic tau decays, complete $\mathcal{O}(\alpha)$ QED radiative corrections are included, while for hadronic decays to resonances, QED corrections are approximated by PHOTOS.

4.3 Detector Simulation and Digitization

After an event is generated, a full detector simulation is performed for the complete ATLAS geometry built within the GEANT4 program [40] to predict how the particles will interact with material in the detector using Monte Carlo methods. The ATLAS detector geometry and layout, as described in Section 2.2 and [23], is parameterized as a collection of three-dimensional shapes with optional type of material and position within the detector. In total, more than 300k physical volumes, i.e., three-dimensional shapes with a specified type of material and position, are required to accurately depict the true geometry of the ATLAS detector. The magnetic field produced by the solenoid and toroidal magnets is also parameterized into a magnetic field map for use by GEANT4. Having accurate as possible a description of the detector and magnetic field is necessary to correctly model physics processes, especially missing energy [30].

With a set of *stable* particles from the event generator and an accurate detector description, GEANT4 simulates how a particle interacts with each element of the detector. Processes that GEANT4 is able to simulate include: electromagnetic interaction, hadronic interaction, transportation through a medium, and more [40]. The simulation of a response of a particle in flight is performed in discrete steps. During each step, a particle has a probability to either have a material interaction or to decay. After each step, if the particle does not decay, its properties such as energy are updated, while if it does decay, new particles are produced and each of these particles are continued in a stepping process through the rest of the detector. Table 4.1 shows how many steps, hits in sensitive detector regions, and secondary particles are performed and simulated in typical $t\bar{t}$ events. From the sheer number of steps performed and hits produced, it becomes clear that the simulation process is the

most time consuming process of the MC simulation chain. In particular, the simulation of electromagnetic and hadronic showers in the calorimeter is the most time consuming portion of simulation.

	Steps	Hits in SD	Sec. above 50 MeV	Sec. above 1 GeV
Inner Detector	1.80×10^6	3.10×10^5	1,570	260
Calorimeter	1.87×10^7	6.87×10^6	39,900	1,040
Muon Detector	1.90×10^6	1,030	7,820	332

Table 4.1: The number of steps performed per event per ATLAS detector sub-system in $t\bar{t}$ events. Also included is the average number of hits produced in sensitive detector (SD) regions and the number of secondary particles produced with energy above 50 MeV and above 1 GeV [30].

The simulation of the digitization process is performed by ATLAS sub-detector specific algorithms. Simulated signals, along with noise (i.e., cross-talk between two electric channels), are digitized when a simulated voltage or current in a readout channel exceeds a certain threshold within a timing window. The algorithms used to produce the digits were tuned using test-beam and cosmic data [30].

4.4 Summary

A list of the MC samples used in this analysis is presented in Table 4.2 along with the event generator used, total integrated luminosity of events generated, theoretical cross-section to which the MC sample is normalized to, and the order to which the theoretical cross-section was carried out. It should be noted that the theoretical cross-section prediction is independent of the event generator used to simulated the corresponding MC sample. The uncertainty on the theoretical W/Z cross-section predictions are dominated by the choice of PDF, from factorization and renormalization scale dependence, and from the uncertainty of α_s [41].

Process	$\mathcal{L}^{\text{int}}$ [fb^{-1}]	Generator	$\sigma \times$ BR [nb]	
$\gamma^*/Z \to ee$ ($m_{\ell\ell} > 60$ GeV)	5.04	PYTHIA	0.99 ± 0.05	NNLO
$\gamma^*/Z \to \mu\mu$ ($m_{\ell\ell} > 60$ GeV)	5.04	PYTHIA	0.99 ± 0.05	NNLO
$\gamma^*/Z \to \tau\tau$ ($m_{\ell\ell} > 60$ GeV)	2.02	PYTHIA	0.99 ± 0.05	NNLO
$W \to e\nu$	0.666	PYTHIA	10.5 ± 0.4	NNLO
$W \to \mu\nu$	0.662	PYTHIA	10.5 ± 0.4	NNLO
$W \to \tau\nu$	0.190	PYTHIA	10.5 ± 0.4	NNLO
$t\bar{t}$	4.83	MC@NLO	$0.165^{+0.011}_{-0.016}$	$\sim$NNLO
WW	5.51	HERWIG	0.045 ± 0.003	NLO
WZ	13.5	HERWIG	0.0185 ± 0.0009	NLO
ZZ	41.6	HERWIG	0.0060 ± 0.0003	NLO

Table 4.2: The Monte Carlo samples used in this analysis together with the total number of events, the default event generator used, the theoretical cross-section, and the $\mathcal{O}(\alpha_s)$ in which the calculation was performed. The $t\bar{t}$ sample was filtered at the generator level to only have events in which at least one of the W bosons decays to leptons ($e/\mu/\tau$). The order to which the theoretical cross-section calculation was performed is independent of the MC event generator that was used to simulate the specific physics process. The NNLO theoretical cross-sections were obtained in [41].

Chapter 5

RECONSTRUCTION ALGORITHMS

Events that pass all three trigger levels (Chapter 3), are grouped into physics streams depending on the specific trigger chain that the event satisfied; events that passed multiple triggers potentially could be placed into multiple streams. This analysis used events from two physics streams: one where events had at least one electron or photon object that passed all three trigger levels, and one where events had at least one muon object that passed all three trigger levels. The event selection was designed, for each of the four final states, to ensure that no double counting occurred (see dilepton veto in Section 6.5). All events in each stream are then fully reconstructed using the same software used to reconstruct the simulated MC (Chapter 4). Reconstruction includes forming tracks from hits in the inner detector (ID) and the muon spectrometer (MS) as well as jets from depositions in the calorimeters. Once all the tracks are reconstructed, the primary vertex (PMV) and subsequent secondary or pileup vertices can be formed. Once all tracks, jets, and a PMV are reconstructed, higher order physics objects such as electrons, muons, and taus are formed by either associating ID tracks to calorimeter clusters of energy or in the case of muons, by associating an ID track to a MS track. Finally, the presence of neutrinos are inferred by measuring any excess energy (momentum) transverse to the beam ($E_{\mathrm{T}}^{\mathrm{miss}}$).

5.1 Track Reconstruction

Track reconstruction in the ATLAS ID takes advantage of the strengths of all three sub-detector technologies, Pixel, SCT, and TRT. Tracks are reconstructed with $p_{\mathrm{T}} > 100$ MeV over all angles of ϕ and $|\eta| < 2.5$. All ID tracks are reconstructed through two sequences of algorithms: an inside out approach that reconstructs tracks starting from the beam spot, and an outside in approach that starts from the TRT hit information and attempts to reconstruct tracks that did not originate from the PMV such as kaon decays or photon

conversion tracks [42].

The inside out approach first attempts to form a track from the hit information within the silicon detectors (Pixel and SCT). The first step converts the raw detector information into 3 dimensional space points. This is automatic for pixel hits since their is segmentation in both ϕ and z, while for the SCT this is not possible for individual measurements since there is no segmentation in z. Instead pairs of SCT hits from adjacent layers, which are offset by 40 mrad, are used to form the 3 dimensional hits. Once the detector hit information is translated to space points, pattern recognition is performed to produce a collection of tracks. Once a collection of tracks are formed, there exist many fake tracks that share hits with actual tracks. An iterative process then loops over tracks with shared hits. A ranking process will then sort all the tracks based on hit quality information such as whether there is a hit in the innermost-layer of the pixel detector or a hole in any of the pixel layers. Tracks with higher scores retain the shared hit, while the track with the lower score has the shared hit removed and the track is then refit and re-scored. This procedure is done until all ambiguities are removed. After the collection of good silicon tracks are resolved, an attempt is made to extend the track with a segment of hits into the TRT sub-detector [43, 44].

The outside in approach is performed after the inside out approach. TRT segments that were used in extending tracks from the silicon detector are then removed and attempts are made to extend the remaining TRT segments with hits from the SCT and pixel detectors (that were previously not used). Tracks resulting from long-lived hadrons and photon conversions with a p_{T} above 300 MeV can then be recovered.

5.2 Jet Reconstruction

Jets in ATLAS are reconstructed from the anti-k_{T} algorithm [45] using three dimensional topological clusters as input [46]. The anti-k_{T} algorithm is preferred over other jet clustering algorithms because it produces conical jets that are both collinear and infrared safe.

A topological cluster begins with a single calorimeter cell seed with an energy that is at least 4σ above the noise threshold for that cell. Neighboring cells are then added iteratively to the cluster if their energy exceeds 2σ of the noise threshold. Finally all neighboring cells are added to the cluster.

Jets are then formed from the list of clusters using the anti-k_{T} algorithm which defines two distance parameters between clusters/pseudo-jets:

$$d_{ij} = \min(k_{ti}^{-2}, k_{tj}^{-2})\frac{\Delta_{ij}^2}{R^2} \quad (5.1)$$

$$d_{i\mathrm{B}} = k_{ti}^{-2} \quad (5.2)$$

Where R is the distance parameter, 0.4, Δ is the distance between the two clusters(ΔR), and k_t is the transverse momentum of the cluster. Cluster i is considered a jet and removed from the list of clusters if $d_{i\mathrm{B}} < \min_j\{d_{ij}\}$, otherwise cluster i is combined with the cluster j that minimizes equation 5.1 and the combined cluster is inserted back into the list of clusters. This procedure is done until the list of clusters is empty.

The distance parameter, R, dictates whether soft radiation will tend to be clustered with a hard jet (cluster) or not. If the distance between a cluster from soft radiation and a hard jet is less than the distance parameter, then the hard jet will tend to absorb the soft cluster, otherwise the two objects will be classified as separate jets. By making R too small, a reconstructed jet may underestimate the energy and size of the underlying physics object. If the distance parameter is too large, on the other-hand, the reconstructed jet may overestimate the energy of the underlying physics object. Jets in ATLAS are reconstructed with either $R = 0.4$ or 0.6. Due to the collimation of hadronic taus, jets with $R = 0.4$ were used in this analysis.

The energy of jets is initially calibrated at the electromagnetic (EM) scale. At the electromagnetic scale, energy resulting from EM showers are properly accounted for, while the energy resulting from hadronic showers are not. Jets, which are primarily hadronic in nature, are calibrated to the hadronic scale in three steps:

- Correct for any excess energy caused by multiple pp collisions occurring during the same bunch crossing. This correction is done on average in bins of η and on the number of reconstructed vertices.

- The position of the reconstructed jet is corrected from pointing to the geometric center of the detector to the primary reconstructed vertex. Corrections are applied on each

of the constituent topoclusters.

- Monte Carlo derived multiplicative factors are applied to each reconstructed jet.

The derivation of the Monte Carlo correction factors is performed by comparing the reconstructed jets energy at EM scale with the energy of matched truth jets.[1] The method used to derive a continuous response function is done in the same way as is done for the tau energy scale (TES Section 5.5.1).

5.3 Electron Reconstruction

High performance[2] electron candidates are reconstructed in the region $|\eta| < 1.37$ && $1.52 < |\eta| < 2.47$, where the gap in η corresponds to the barrel/endcap transition region in the EM calorimeter. Forward electrons, on the other hand, are reconstructed using only the calorimeter (fiducial ID coverage ends $|\eta| > 2.5$). Electron reconstruction begins by reconstructing 2-dimensional clusters in the second layer of the electromagnetic (EM) calorimeter using a sliding window. Clusters with energy greater than 2.5 GeV become electron candidate seeds. The seed becomes an electron candidate if a track from the ID, with $p_{\mathrm{T}} > 0.5$ GeV, is matched to the cluster within $\Delta(\eta) \times \Delta(\phi) = 0.05 \times 0.1$ [47]. If multiple tracks are found within the window, the track of closest approach to the cluster's baryon center is retained. The energy of the final electron candidate is taken from the calorimeter cluster, while its direction is taken from the ID track. Electron candidates with E_{T} as low as 5 GeV can be reconstructed, however, in this analysis all electrons are required to have an E_{T} of at least 16 GeV.

5.3.1 Electron Identification

Electron identification concentrates on separating prompt electrons resulting from the direct decay of W/Z bosons from hadrons faking electrons in jets, electrons from converted

[1] A truth jet is a jet reconstructed with a given jet algorithm using stable truth particles with a $c\tau > 3$ mm as the input collection of clusters. Muons and neutrinos are not included in truth jet reconstruction.

[2] Electron candidates are reconstructed outside of the ID fiducial region, $|\eta| > 2.5$, however, these candidates do not have an associated track. In addition, the calorimeter segmentation is more coarse at high pseudorapidity.

photons, or from real electrons that decay from heavy flavor mesons. Electron identification generally provides a Loose, Medium, and Tight decision where Tight is a subset of Medium and Medium is a subset of Loose. The decision is based on variables derived from the cluster shape, leakage into the hadronic calorimeter, quality of the matched track, and the track/cluster association. The decisions for each discriminant are:

- **"Loose: "**

  The "Loose" decision includes requirements on hadronic leakage, the energy in the second layer of the EM calorimeter (where the seed is formed), and on the lateral width of the shower shape. Hadronic leakage is defined as the ratio of either all the E_{T} in the hadronic calorimeter or only the E_{T} in the first layer of the hadronic calorimeter to that of cluster itself. The energy in the second layer is further required to be centralized by ensuring that the ratio of energy in a window of $3x7$ cells centered about the cluster to a window of $7x7$ cells is close to unity.

- **"Medium: "**

  The "Medium" decision requires stricter track and cluster matching, track quality criteria, and requirements on the strip layer of the calorimeter.[3] The requirements on the strip layer of the calorimeter include ensuring that the E_{T} of the maximal cell is much greater than the sub-maximal cell and that the total shower width is small in the η direction.

- **"Tight: "**

  The "Tight" decision places even more stringent cuts on the matched track. High threshold TRT hits on the matched track are used to distinguish heavier hadrons from electrons, while a hit is required in the innermost layer of the pixel detector, assuming the track does not traverse a dead pixel module, to veto photon conversions.

---

[3]The strip layer of the EM calorimeter is the first layer of the calorimeter which has very fine longitudinal segmentation $(\Delta\eta) = 0.0031$ at the expense of ϕ segmentation.

The specific thresholds used in the above variables are binned in 10 (cluster)[4] η bins by 11 (cluster) E_{T} bins [48].

Both the "Medium" and "Tight" cuts are used in this analysis and have an efficiency, relative to the 98.3% reconstruction efficiency, of 96.3% and 78.5% respectively for electrons with $20 < E_{\mathrm{T}} < 50$ GeV within the pseudorapidity region of $|\eta| < 1.37$ or $1.52 < |\eta| < 2.47$. For electrons with $15 < p_{\mathrm{T}} < 20$ GeV, lower identification efficiencies of 94.9% (78.3%) were measured for "Medium" ("Tight") identified electrons [48]. The efficiencies were derived from $Z \to ee$ and $W \to e\nu$ MC simulated samples. A discussion on the scale factors used to correct the MC reconstruction and identification efficiencies to that observed in $Z \to ee$ events can be found in Section 9.2.1.

5.4 Muon Reconstruction

Muon stand-alone reconstruction is performed using information only from the muon subdetectors and is performed without the requirement of an ID track. The reconstruction begins locally in an individual precision chamber with the construction of straight-line segments using the precision η measurement in conjunction with the trigger ϕ information when available. Segments are required to point to the origin of the ATLAS detector. Three dimensional tracks are then formed from 2 or more segments reconstructed in unique chambers. The tracks' p_{T}, η, ϕ, z_0, and[5] d_0 are then measured after extrapolating to the PMV and accounting for energy loss in the calorimeters. The average energy loss for a muon traversing the calorimeter system is 3 GeV [42].

The combined muon is formed when an ID track can be associated with a stand-alone muon track. In order to associate a MS track with an ID track, a χ^2 test is performed which is computed by taking the difference between the respective ID and MS track parameters weighted by their combined covariance matrices. There are two algorithms used to compute

[4]The direction of electron candidates can be based on either the parameters of the matched track or on the center of the calorimeter cluster seed. For analysis purposes (i.e., the invariant mass of an electron and hadronic tau candidate), the electron candidates track direction is used, for purposes of identification the direction of the cluster is used.

[5]The d_0 is the transverse distance of closest approach of the track with the PMV, while z_0 is the longitudinal distance of closest approach.

the parameters of the final combined track: one where the combined track parameters are a statistical combination of the individual track parameters, and one where the final track parameters are extracted from a refit of the combined ID and MS track. Both methods were tested and shown to yield equivalent results [42]; the former method was used in this analysis.

The efficiency of combined muon reconstruction was measured in data using a $Z \rightarrow \mu\mu$ tag and probe analysis. A tight combined muon was tagged, while a track reconstructed in the ID with opposite charge to the tag was used as the probe. The invariant mass of the muon ID track system was then required to be within 10 GeV of the Z peak. An efficiency of 93.3 ± 0.022 (stat) ± 0.013 (sys)% relative to the ID track was found for muons with $p_{\mathrm{T}} > 20$ GeV, while the corresponding value in MC was found to be 92.4% [42, 49]. Although the efficiency measurements in data are consistent with simulation, the use of scale factors was necessary depending on the geometrical location of the reconstructed muon. This is discussed further in Section 9.2.2. Muon reconstruction is commissioned as low as $p_{\mathrm{T}} = 6$ GeV, however, muons in this analysis are required to have a p_{T} of at least 10 GeV. Other than ensuring that the the muon candidate is combined, there is no explicit identification required on the muon candidate. [6]

5.5 Tau Reconstruction

Tau reconstruction attempts to reconstruct only hadronically decaying tau leptons; those taus that decay to a lepton (electron or muon) are nearly indistinguishable from a lepton that decays directly from a W/Z boson and are thus reconstructed as a lepton. A tau candidate is reconstructed from a jet seed, $|\eta| < 2.5$, using the anti-k_{T} algorithm with an R value of 0.4 (Section 5.2). From the initial jet seed, the tau candidate direction is determined from the vector sum over all the constituent topoclusters, the energy is determined by summing over all uncalibrated (EM scale) cells within the seed jet ($\Delta(R) < 0.4$) and further calibrated to the tau energy scale (Section 5.5.1), while the mass is defined to be zero [50]. Tracks with the following quality criteria:

[6] There are track quality requirements on the ID track that our analysis imposed. This is discussed in detail in Section 6.2.2

- $p_{\mathrm{T}} > 1$ GeV
- Number of hits in the first layer pixel ≥ 1
- Number of total pixel hits ≥ 2
- Number of total pixel and SCT hits ≥ 7
- $d_0 < 1.0$ mm
- $|z_0 \sin\theta| < 1.5$ mm

are then associated to each tau candidate in a core cone $\Delta(R) < 0.2$ about the initial jet seed. The number of tracks associated with the tau candidate is also known as its number of "prongs". Tracks are also counted in an isolation annulus, $0.2 < \Delta R < 0.4$, about the core cone in order to reject jet fakes (see Section 5.5.2).

5.5.1 Tau Energy Scale

When measuring the energy of a hadronic tau candidate, we can only measure the energy deposited by the decay products of the original tau lepton that are "visible" to the detector. Thus, since neutrinos rarely interact with matter, we are only measuring the energy deposited by the stable charged and neutral pion[s] (or possibly kaon[s]). Since hadronic taus, depending on their specific decay mode, may have in addition to charged pions, neutral pions (which decay immediately to two photons) in the final state, neither the EM scale nor the hadronic scale is appropriate for measuring the energy of the tau candidate. Thus, an independent scale is applied to each tau candidate depending on whether it has one track or multiple tracks; and whether the tau was reconstructed in the barrel ($|\eta| < 1.3$), the barrel-endcap transition region ($1.3 < |\eta| < 1.6$), or in the endcap ($|\eta| > 1.6$). In order to further separate single prong taus with no neutral pions from those with neutral pion[s], the electromagnetic energy fraction at EM scale (f_{EM}) of the tau candidate is required to be $f_{\mathrm{EM}} < / > 0.15$. Single prong taus with $f_{\mathrm{EM}} < 0.15$ are not classified with respect to η due to a lack of statistics.

For each tau candidate classification, response functions:

$$R(p_{\mathrm{T}}^{\mathrm{EM}}) = \frac{p_{\mathrm{T}}^{\mathrm{EM}}}{p_{\mathrm{T}}^{\mathrm{gen}}} \tag{5.3}$$

are formed from simulation, where $p_{\mathrm{T}}^{\mathrm{EM}}$ refers to the energy from summing over all cell energies within $\Delta R = 0.4$ of the jet seed axis, while $p_{\mathrm{T}}^{\mathrm{gen}}$ is the true visible p_{T} of the tau candidate[7]. Response functions are constructed in bins of $p_{\mathrm{T}}^{\mathrm{gen}}$, where for each bin, a distribution of $p_{\mathrm{T}}^{\mathrm{EM}}/p_{\mathrm{T}}^{\mathrm{gen}}$ and of $p_{\mathrm{T}}^{\mathrm{EM}}$ are produced. The response is then, for each $p_{\mathrm{T}}^{\mathrm{gen}}$ bin, the mean of an antisymmetric Gaussian fit of the $p_{\mathrm{T}}^{\mathrm{EM}}/p_{\mathrm{T}}^{\mathrm{gen}}$ distribution. In order to get the response as a function of $p_{\mathrm{T}}^{\mathrm{EM}}$ rather than $p_{\mathrm{T}}^{\mathrm{gen}}$, the arithmetic mean of the $p_{\mathrm{T}}^{\mathrm{EM}}$ distribution is computed in the corresponding $p_{\mathrm{T}}^{\mathrm{gen}}$ bin. Finally to get a continuous tau energy scale (TES), the discrete set of points, ($p_{\mathrm{T}}^{\mathrm{EM}}$, $p_{\mathrm{T}}^{\mathrm{EM}}/p_{\mathrm{T}}^{\mathrm{gen}}$), are fit to the following function:

$$1 + \frac{a_1}{\ln(p_{\mathrm{T}}^{\mathrm{EM}})} + \frac{a_2}{[\ln(p_{\mathrm{T}}^{\mathrm{EM}})]^2} + \frac{a_3}{[\ln(p_{\mathrm{T}}^{\mathrm{EM}})]^3} \tag{5.4}$$

which is shown for a particular classification in Figure 5.1.

5.5.2 Tau Identification

Hadronic taus generally decay to one or three charged pions with 0, 1, or 2 associated neutral pions. Differentiating these objects from generic multijet events is difficult since the resulting detectable decay products are similar, and the cross-section for multijet events is six orders of magnitude larger than W/Z decays. The two primary methods used to differentiate hadronic taus from jets are: the tau candidates track multiplicity and the width of the tau candidate as measured by the calorimeter. Since more than 99% of true hadronic taus have either 1 or 3 prongs [9], tau candidates with more than 3 prongs can generally be considered fakes. Also, since $m(W/Z) \gg m(\tau)$, true hadronic taus should be highly collimated leaving a relatively narrow deposition of energy in the calorimeter as compared to generic jets.

The track multiplicity is not explicitly used in any tau identification method in order to minimize any bias of the tau track distribution after identification is applied. Applying tau

[7]The four vector of the true visible tau is $\tau_{\mathrm{vis}} = \tau - \tau_{\nu}$.

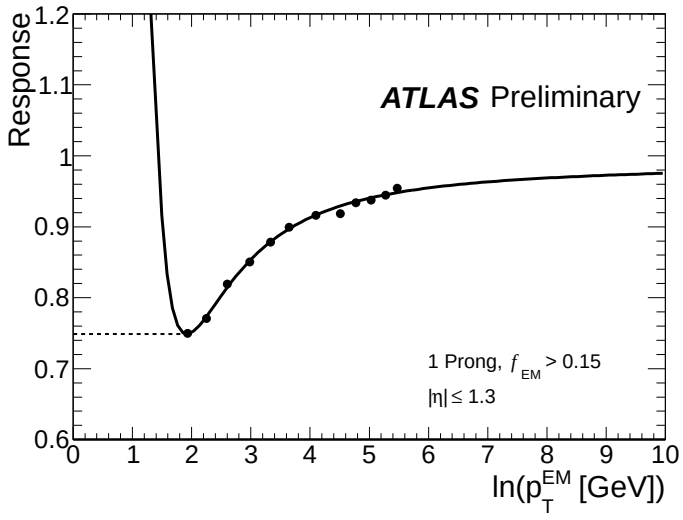

Figure 5.1: Final response function for single prong tau candidates restricted to the barrel region and having an $f_{\mathrm{EM}} > 0.15$. The points represent the individual response measurements, while the solid line represents the final fit. For low p_{T} taus, the dashed line represents the minimum response function that is used to calibrate the tau's energy [50].

identification to reconstructed taus without any other event level cuts, still leaves an impure sample of true hadronic taus. If this impure sample of taus does not show a preference for one or three prong candidates, but does after other event level cuts, then there is strong evidence for the presence of true hadronic taus.

In general, the identification variables computed for tau candidates exploit the collimation of the tau in calorimeter, tracking, and combined tracking and calorimeter variables. The following are a list of the main variables used in identification:

- R_{EM}:

  The electromagnetic radius (R_{EM}) is the E_{T} weighted shower width of the tau candidate as measured in the first three layers of the EM calorimeter (presampler, layer 1, and layer 2):

  $$R_{\mathrm{EM}} = \frac{\Sigma_i E_{\mathrm{T},i} \Delta R_i}{\Sigma_i E_{\mathrm{T},i}}. \tag{5.5}$$

  The index, i, runs over all cells associated to the tau candidates jet seed within $\Delta R < 0.4$ of the uncalibrated jet seed axis, while the distance, ΔR_i, is measured

between the i^{th} cell and the jet axis.

- R_{track}:

  The track radius is the p_{T} weighted track width and is defined as:

$$R_{\text{track}} = \frac{\Sigma_i p_{\text{T},i} \Delta R_i}{\Sigma_i p_{\text{T},i}}. \tag{5.6}$$

  The index, i, runs over all tracks associated to the tau within $\Delta R < 0.4$ of the jet seed axis. Since the width is with respect to the jet seed axis, rather than the leading track, the width is always non-zero as long as there is at least one associated track.

- f_{track}:

  The leading track momentum fraction is the ratio of the p_{T} of the leading track to the p_{T} of the tau candidate.

The above variables are used in three different tau discriminant algorithms: a cut based discriminant, a multi-variate Boosted Decision Tree, and a multi-variate projective likelihood. The cut based discriminant was used in this analysis.

The cut based discriminant is optimized separately for one prong and three prong tau candidates and utilizes the R_{EM}, R_{track}, and the f_{track} identification variables (Figure 5.2). Optimal cut values were chosen by performing a three dimensional grid search on the three identification variables. Grid points were required to achieve a signal efficiency (equation 5.7) of 30 ("Tight"), 50 ("Medium"), or 70% ("Loose"). These points that simultaneously produced the smallest background efficiencies (equation 5.8) were then selected as the discriminant points. As a final requirement, the "Tight" identification was required to be a strict subset of "Medium" identification, and the "Medium" identification was required to be a strict subset of the "Loose" identification. The grid search was performed using signal taus from $W \rightarrow \tau\nu$ and $Z \rightarrow \tau\tau$ samples, and background jets from data using a dijet event selection. To account for the tighter collimation of jets at higher p_{T}, the cuts on R_{EM} and R_{track} were parameterized as a function of p_{T}. Figure 5.3 shows the signal efficiency of the "Tight" tau discriminant for both 1 and 3 pronged tau candidates (see Section 9.2.4 for

discussion on systematic uncertainties). The efficiency is defined as:

$$\varepsilon_{\text{sig}}^{1/3-\text{prong}} = \frac{\begin{pmatrix}\#\text{ of tau candidates with 1/3 reconstructed}\\ \text{track(s), passing ID, and truth-matched to a}\\ \text{simulated 1/3-prong decay}\end{pmatrix}}{\begin{pmatrix}\#\text{ of simulated visible hadronic taus with 1/3}\\ \text{prong(s)}\end{pmatrix}} \tag{5.7}$$

while the background efficiency is defined as:

$$\varepsilon_{\text{bkg}}^{1/3-\text{prong}} = \frac{\begin{pmatrix}\#\text{ of tau candidates with 1/3 reconstructed}\\ \text{track(s), passing ID}\end{pmatrix}}{\begin{pmatrix}\#\text{ of tau candidates with 1/3 reconstructed}\\ \text{track(s)}\end{pmatrix}}. \tag{5.8}$$

The average efficiency for "Tight" identification, measured in MC, for taus with $p_{\text{T}} > 20$ GeV is approximately 30% while approximately 1% of generic jets reconstructed as tau candidates pass the "Tight" identification. Tau candidates with a $p_{\text{T}} > 20$ GeV that pass the "Tight" identification are used in this analysis.

5.6 Missing Energy Reconstruction

For events with no reconstructed muons, the transverse missing energy ($E_{\text{T}}^{\text{miss}}$) is formed by vectorially summing all 3 dimensional topological clusters:

$$E_{x,y}^{\text{miss}}(e) = -\mathbf{\Sigma_i} E_{x,y}^{i} \tag{5.9}$$

(Section 5.2 [46]). All clusters are further split if additional local maxima can be found. On average each cluster, after splitting, represents approximately 1.6 particles [51]. The energy of all clusters are calibrated assuming that all incident particles are electromagnetic in nature. These clusters are then classified as either hadronic or electromagnetic in nature and then re-calibrated if necessary [52].

Events with muons in the final state are further corrected for the momentum of the muon track[s] taking into account any loss in the calorimeter:

$$E_{x,y}^{\text{miss}}(\mu) = -\mathbf{\Sigma_i} E_{x,y}^{i} - \mathbf{\Sigma_i} E_{x,y}^{i}(\text{muon tracks}) + \mathbf{\Sigma_i} E_{x,y}^{i}(\text{energy loss}). \tag{5.10}$$

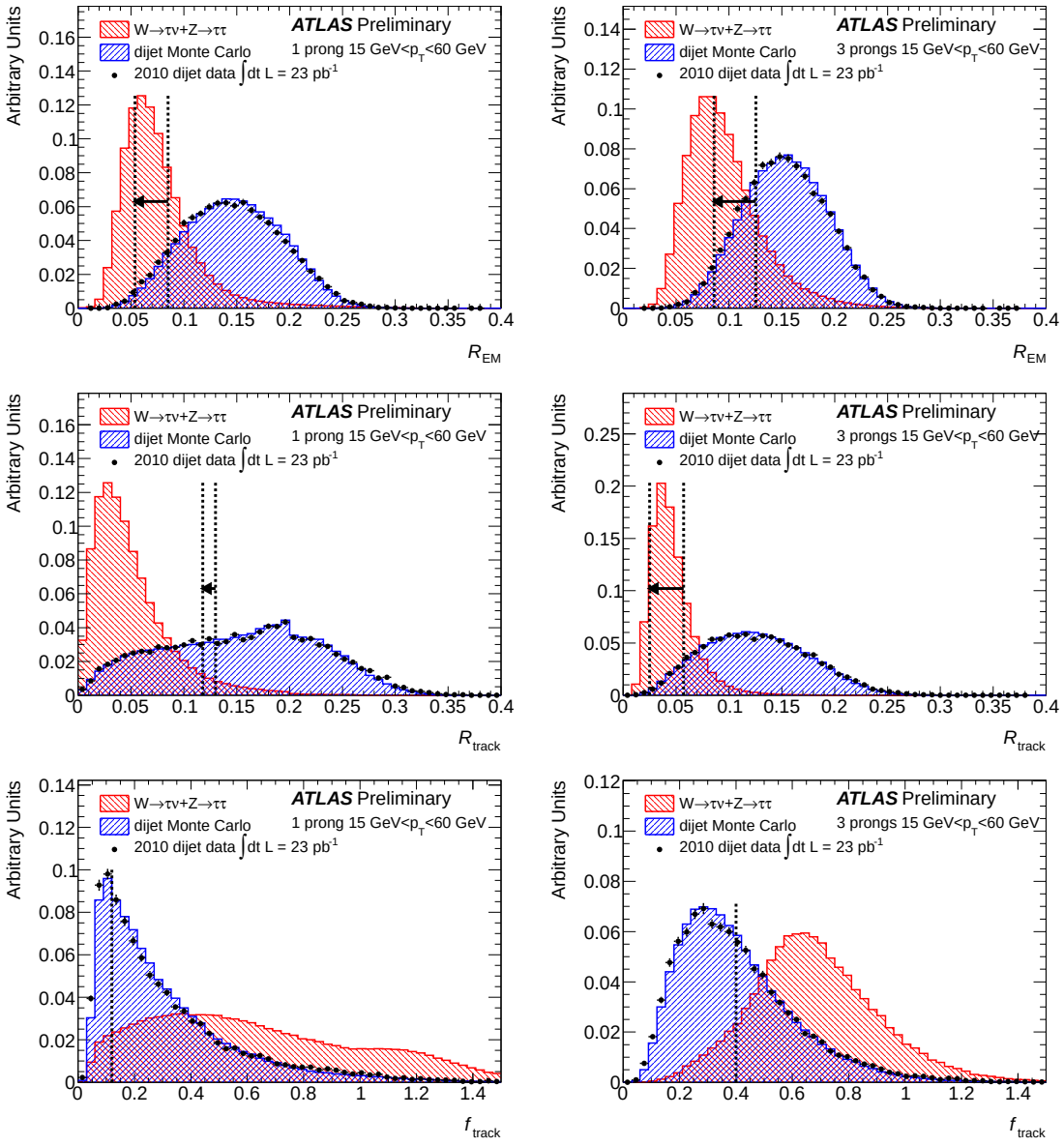

Figure 5.2: The tau identification variables used in the cut base tau discriminant: R_{EM} (top), R_{track} (middle), and f_{track} (bottom). The distributions are displayed both for one prong (left) and multi-prong (right) candidates. The vertical line represents the value at which the particular distribution was cut on for the "Tight" working point. The R_{track} and R_{EM} distributions have two vertical lines which depict the range that the distributions were cut on depending on the E_{T} of the tau candidate [50].

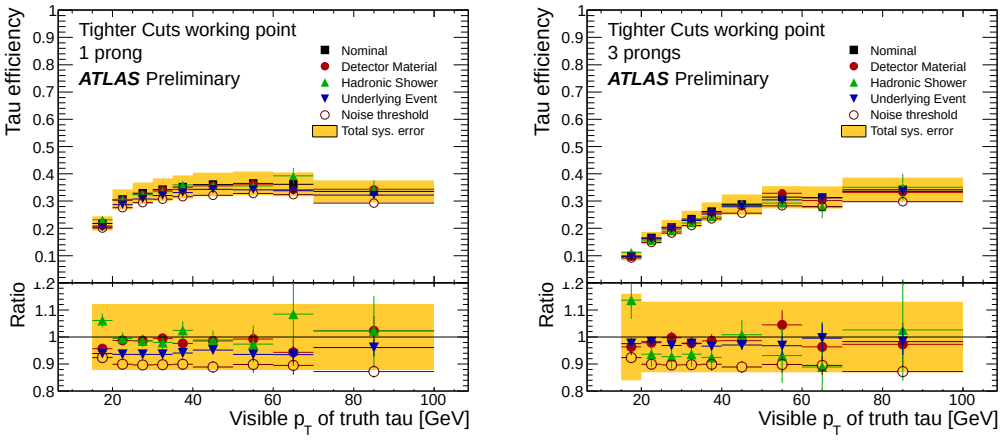

Figure 5.3: The "Tight" tau identification efficiency for one prong (left) and three prong (right) tau candidates. The efficiency, as measured on the default MC samples, is plotted against the efficiency when varying systematic uncertainties due to extra detector material, the hadronic shower shape, the underlying event, and by varying the calorimeter noise threshold. The shaded band represents the total systematic per p_{T} bin. The bottom plot is a ratio of each systematic variation to the nominal result [50].

Chapter 6

EVENT SELECTION

The event selections for $Z \rightarrow \tau\tau$ events are classified based on the decay products of the $\tau\tau$ pair: either to two hadronically decaying taus ($\tau_h\tau_h$), to hadron[s] and an electron ($\tau_h\tau_e$), to hadron[s] and a muon ($\tau_h\tau_\mu$), to two electrons ($\tau_e\tau_e$), to two muons ($\tau_\mu\tau_\mu$), and to an electron and a muon ($\tau_e\tau_\mu$). As discussed in Section 1, the $\tau_h\tau_h$ and $\tau_e\tau_e$ channels were not studied in depth due to overwhelming backgrounds from either multijet events or $\gamma^*/Z \rightarrow ee$ events, respectively. The $\tau_h\tau_e$ and $\tau_h\tau_\mu$ final states are collectively referred to as the semileptonic final states, while the $\tau_e\tau_\mu$ and the $\tau_\mu\tau_\mu$ final states are collectively referred to as the leptonic final states. For all four final states the event selection begins with an event preselection (Section 6.1), followed by an object selection (Section 6.2), and then finally event level cuts (Sections 6.5.1, 6.5.2, and 6.5.3).

6.1 Event Preselection

Events were only considered when the LHC was providing stable beams at 3.5 TeV of energy and when all ATLAS sub-detectors were performing at $> 90\%$ efficiency. In order to further select clean LHC events, a primary vertex (PMV) was required with at least 3 associated tracks and events with out of time jets or tau candidates caused, by cosmic ray events or known defects in the calorimeter, were rejected [53]. Quality criteria applied to reconstructed jets used to determine if an event should be rejected based on a poorly or anomalously reconstructed jet included:

- Ensure that less than 50% of the energy in a reconstructed jet originated from calorimeter cells whose signal shape was abnormal.

- Ensure that the majority of cells contained within a jet had energy deposited in them within 10 ns of the bunch crossing.

- Reject jets that were localized within one layer of the calorimeter.

Most of the above variables were not found to be well modeled by simulation. Thus, this procedure was only performed on data events. In total, less than 1% events were rejected based on this requirement in data. The systematic uncertainty of rejecting events with poorly or anomalously reconstructed jets is evaluated in Section 9.6.

6.2 Object Selection

After an event was preselected, objects ($e/\mu/\tau$/jets) were preselected if they passed minimal kinematic and identification criteria (Table 6.1). These preselected objects were then thinned in order to remove object redundancy (overlap removal); two objects are redundant when they are reconstructed from the same detector signature. Preselected electrons were removed if they were within[1] $\Delta R < 0.2$ of any preselected muons, preselected taus were removed if they were within $\Delta R < 0.4$ of any preselected electrons or muons, and finally any preselected jets were removed if they were within $\Delta R < 0.4$ of any preselected electrons, muons, or taus. The order of object preference was based on the probability that the object could be faked. Minimal preselection was performed before any thinning in order to minimize any instances where, for example, a true hadronic tau was removed by a loosely reconstructed electron candidate, while full object selection was not required in order to maximize the probability of removing reconstructed hadronic tau candidates that were truly electrons.

6.2.1 Electron Selection

The requirements for preselected electrons were identical for all final states. A reconstructed electron was required to have $E_{\mathrm{T}} > 16$ GeV, and $|\eta| < 2.47$. Only electrons with a well reconstructed energy were selected. To that end, electrons within the calorimeter barrel/endcap transition region, $1.37 < |\eta| < 1.52$, in addition to any electrons reconstructed in regions of the calorimeter that suffered from excessive noise, readout problems, or from non-nominal high voltage conditions, were vetoed. Finally, the "Medium" electron identification with

[1] $\Delta R = \sqrt{\Delta(\eta)^2 - \Delta(\phi)^2}$, is a measure of distance between two particles.

track match was required to be true for all preselected electrons (Section 5.3). For the $\tau_h\tau_e$ final state, the "Tight" electron identification was required to be true for the final selected electron candidate, while for the $\tau_e\tau_\mu$ final state, only "Medium" identification was required on the selected electron.

6.2.2 Muon Selection

Selected muons were required to be combined (Section 5.4), have a transverse momentum (p_{T}) > 15 GeV, a pseudorapidity ($|\eta|$) < 2.4, a longitudinal impact parameter, from the Muon Spectrometer track, (z_0(MS)) < 10 mm and the following quality criteria on the ID track:

- Number of hits in the first layer of the pixel detector ≥ 1
- Number of total pixel hits in all layers ≥ 2
- Number of SCT hits ≥ 6
- (Number of TRT high threshold hits)/(Number TRT Hits) < 0.9 ($|\eta| < 1.9$)

in order to ensure the track was well reconstructed and to minimize fakes from decays in flight. The above track quality criteria would take into account holes due to dead or missing detector modules in the SCT and TRT, however, only one hole was allowed per track.

Each final state had slight modifications to the muon selection requirements. The $\tau_e\tau_\mu$ final state allowed muons to have $p_{\mathrm{T}} > 10$ GeV since events were triggered by an electron trigger. The $\tau_\mu\tau_\mu$ final state required that the lead muon have a $p_{\mathrm{T}} > 15$ GeV, while the second muon was allowed to have a $p_{\mathrm{T}} > 10$ GeV. Neither semileptonic final state modified the above selection, however, the selection was performed in two steps: a preselection that had no requirements on the ID track, and a final selection which imposed all selection criteria. By relaxing the requirements on the preselected muon, more muons that faked a hadronic tau signature were removed at the overlap removal stage.

6.2.3 Tau Selection

Hadronically decaying tau candidates were used only in the $\tau_h\tau_e$ and $\tau_h\tau_\mu$ final states. All hadronic tau candidates were required to have $p_{\mathrm{T}} > 20$ GeV, and $|\eta| < 2.47$ (excluding the same transition region as electrons, $1.37 < |\eta| < 1.52$). Additionally, taus with one associated track were required to pass the "Medium" identification, while taus with more than one associated track were required to pass the "Tight" identification (Section 5.5). Finally, any tau that fails the tight electron veto was removed from further consideration. The requirement on the number of tracks associated with the tau candidate was not applied until all other event level cuts were applied in order to produce an unbiased track distribution (Section 6.5).

6.2.4 Jet Selection

Jets were used directly only in the $\tau_e\tau_\mu$ final state. The jets used in this analysis, like the jet seeds used to seed hadronic tau candidates, were reconstructed from three-dimensional topological clusters using the anti-k_{T} algorithm with distance parameter $R = 0.4$. Jets used in this analysis were further required to have $p_{\mathrm{T}} > 20$ GeV and $|\eta| < 4.5$. The jet energy scale was calibrated at the EM scale with MC derived multiplicative factors to account for hadronic response (Section 5.2).

6.3 Lepton Isolation

The methods used to reconstruct and identify leptons (e/μ), mentioned above and in Section 5, were primarily intended to veto pions and π/K in flight decays, rather than real leptons from heavy flavor decays (such as c/b meson decays). Generally leptons resulting from heavy flavor meson decays are accompanied with multiple charged and neutral pions that will deposit extra energy in the calorimeter and produce spurious tracks in the ID. These two detector signatures were exploited in two isolation variables: the relative p_{T} fraction of tracks around the lepton candidate in a ΔR cone of size X ($I^X_{p_{\mathrm{T}}}$), and the excess E_{T} relative to the lepton's E_{T} deposited in the calorimeter in a ΔR cone of size X ($I^X_{E_{\mathrm{T}}}$). The values chosen for the four different final states were optimized using MC signal and

multijet enriched data (Figure 6.1). The data vs MC scale factor derivations and systematic uncertainties, for the selections used, are discussed in Section 9.2.3.

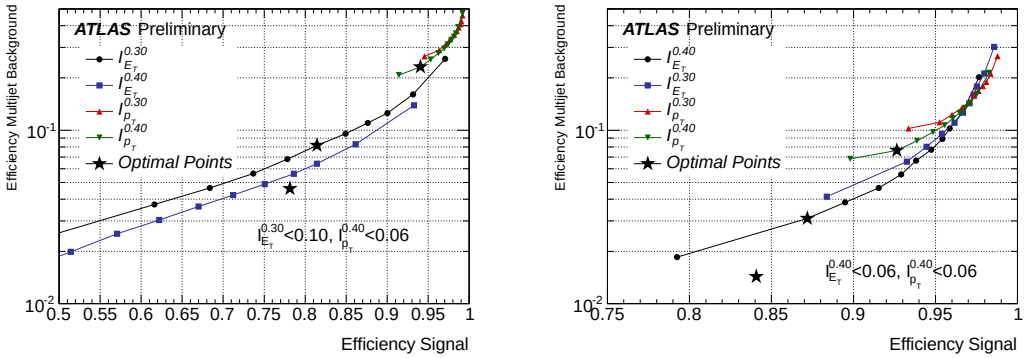

(a) $\tau_h\tau_e$ (b) $\tau_h\tau_\mu$

Figure 6.1: Isolation optimization curves are shown for the $\tau_h\tau_e$ ($\tau_h\tau_\mu$) final state in Figure a (b). The signal efficiency was computed using the default MC signal samples, while the background efficiency was computed using a multijet enriched control region in data. The plot shows relative calorimeter and tracker isolation in ΔR cones of both 0.3 and 0.4. The stars represent the value chosen in this analysis and the third star shows the signal efficiency and background rejection for the combined calorimeter and tracker isolation.

6.4 Final Object Selection

6.4.1 $\tau_h\tau_e$ Final State

The $\tau_h\tau_e$ final state candidate events were selected with a 15 GeV "Medium" single electron trigger. After event preselection, a 16 GeV "Tight" electron candidate was required to match the trigger object and pass the tracking isolation of $I^{0.4}_{p_{\mathrm{T}}} < 0.06$ and the calorimeter isolation of $I^{0.3}_{E_{\mathrm{T}}} < 0.10$. A "Tight" tau candidate with $p_{\mathrm{T}} > 20$ GeV that satisfied the tight electron veto requirement was also required. Data vs MC distributions for lepton isolation can be found in Figure 6.2, while the electron and tau kinematic distributions, after lepton isolation, can be found in Figure 6.3.

Object	$\tau_h\tau_e$	$\tau_h\tau_\mu$	$\tau_e\tau_\mu$	$\tau_\mu\tau_\mu$
Electrons	$p_{\mathrm{T}} > 16$ GeV $\lvert\eta\rvert < 1.37$ or $1.52 < \lvert\eta\rvert < 2.47$ "Tight" ID $I^{0.3}_{E_{\mathrm{T}}} < 0.10$ $I^{0.4}_{p_{\mathrm{T}}} < 0.06$	-	$p_{\mathrm{T}} > 16$ GeV $\lvert\eta\rvert < 1.37$ or $1.52 < \lvert\eta\rvert < 2.47$ "Medium" ID $I^{0.3}_{E_{\mathrm{T}}} < 0.10$ $I^{0.4}_{p_{\mathrm{T}}} < 0.06$	-
Muons	-	$p_{\mathrm{T}} > 15$ GeV $\lvert\eta\rvert < 2.4$ Combined $I^{0.4}_{E_{\mathrm{T}}} < 0.06$ $I^{0.4}_{p_{\mathrm{T}}} < 0.06$	$p_{\mathrm{T}} > 10$ GeV $\lvert\eta\rvert < 2.4$ Combined $I^{0.4}_{E_{\mathrm{T}}} < 0.06$ $I^{0.4}_{p_{\mathrm{T}}} < 0.06$	$p_{\mathrm{T}} > 15(10)$ GeV $\lvert\eta\rvert < 2.4$ Combined $I^{0.4}_{E_{\mathrm{T}}} < 0.20$ $I^{0.4}_{p_{\mathrm{T}}} < 0.15$
Taus	$p_{\mathrm{T}} > 20$ GeV $\lvert\eta\rvert < 1.37$ or $1.52 < \lvert\eta\rvert < 2.47$ "Tight" ID		-	-
Jets	-	-	$p_{\mathrm{T}} > 20$ GeV $\lvert\eta\rvert < 4.5$	-

Table 6.1: All kinematic, identification, and isolation requirements imposed on each object type for each $\tau\tau$ final state.

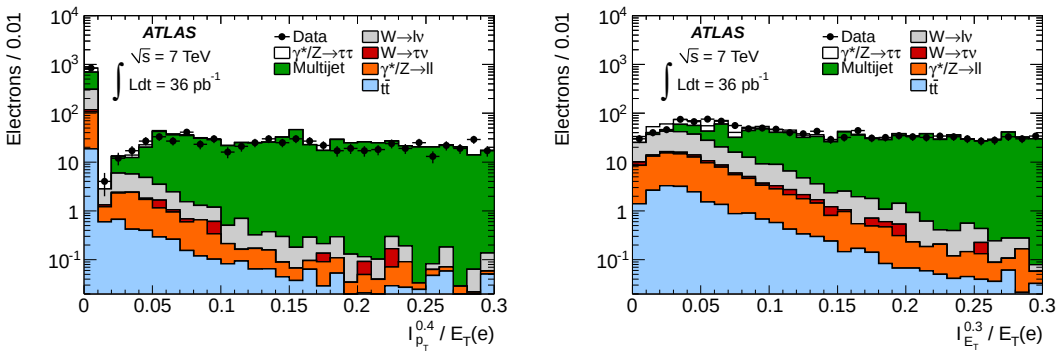

(a) (b)

Figure 6.2: The tracker isolation (left) and calorimeter isolation (right) variables used to suppress electrons resulting from the decays of heavy flavor mesons. Both data and MC are displayed for each plot.

6.4.2 $\tau_h\tau_\mu$ Final State

The trigger selection was slightly more complicated in the $\tau_h\tau_\mu$ final state since as the instantaneous luminosity increased, certain lower p_{T} threshold triggers were prescaled[2] and new higher p_{T} trigger thresholds were introduced. Thus, three separate single muon triggers were used in this analysis in order to maximize the available integrated luminosity. The first trigger had a 10 GeV threshold, while the other triggers had a 13 GeV threshold with differing identification requirements. In order to account for the differing trigger requirements in simulation, a flat random number between 0 and 1 was generated and the specific trigger for an event was then chosen based on the value of the random number:

$$t(r) = \begin{cases} t_1, & r < f_1 \\ t_2, & f_1 \leq r < f_1 + f_2 \\ t_3, & f_1 + f_2 \leq r < 1 \end{cases} \tag{6.1}$$

where r is the random number, t_X is one of the three triggers, and f_X is the fraction of the total integrated luminosity that trigger X represents. After event preselection, a 15

[2]Events that only pass a trigger with a prescale of X are recorded once every X events in order to control the overall event rate.

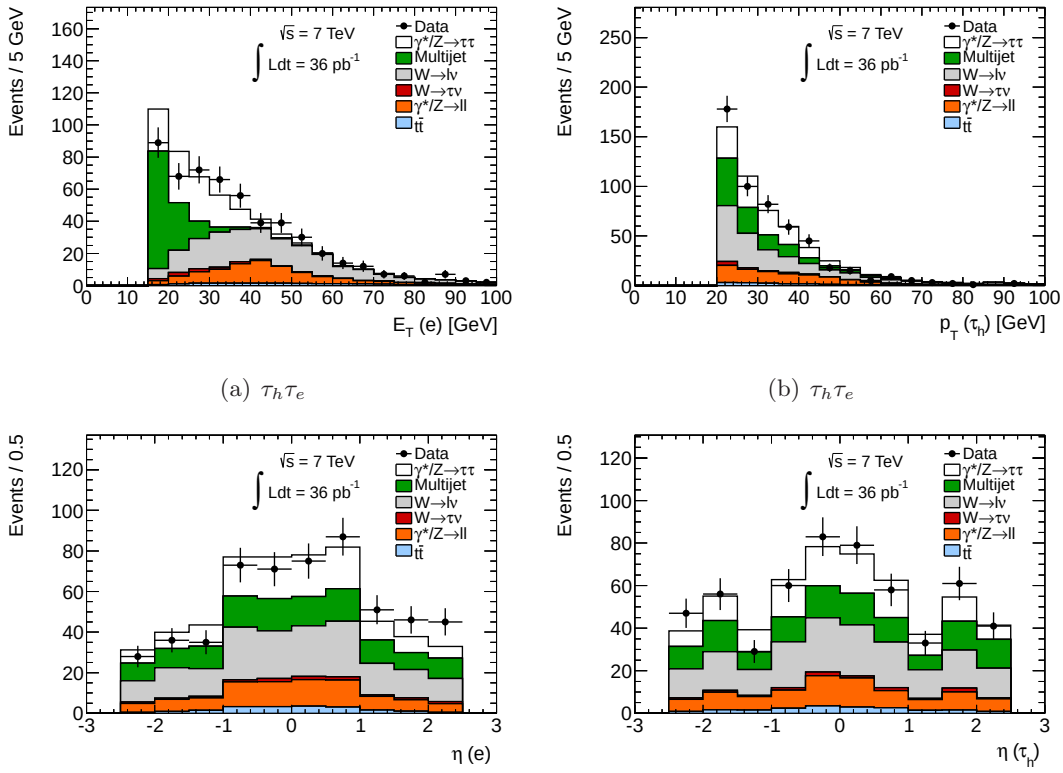

(a) $\tau_h\tau_e$ (b) $\tau_h\tau_e$

(c) $\tau_h\tau_e$ (d) $\tau_h\tau_e$

Figure 6.3: The p_{T} (top) and η (bottom) distributions for electrons (left) and hadronic tau candidates (right) after the requirement of a selected and isolated electron in conjunction with an identified hadronic tau. Both data and MC are displayed for each plot.

GeV "Combined" muon candidate was required to match the trigger object and pass the tracking isolation of $I_{p_{\mathrm{T}}}^{0.4} < 0.06$ and the calorimeter isolation of $I_{E_{\mathrm{T}}}^{0.4} < 0.06$. A "Tight" tau candidate with $p_{\mathrm{T}} > 20$ GeV that satisfied the tight electron veto requirement was also required. Data vs MC distributions for lepton isolation can be found in Figure 6.4, while the muon and tau kinematic distributions, after lepton isolation, can be found in Figure 6.5.

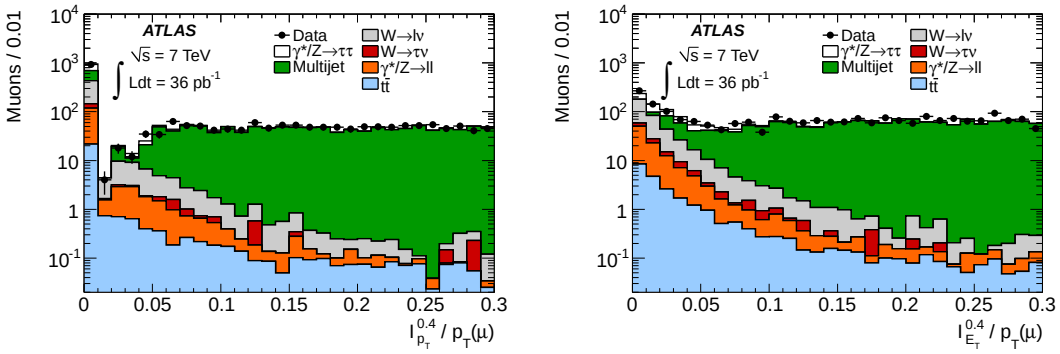

(a) (b)

Figure 6.4: The tracker isolation (left) and calorimeter isolation (right) variables used to suppress muons resulting from the decays of heavy flavor mesons. Both data and MC are displayed for each plot.

6.4.3 $\tau_e\tau_\mu$ Final State

In the $\tau_e\tau_\mu$ final state candidate events were selected with a 15 GeV "Medium" single electron trigger. A single electron trigger was used rather than a single muon trigger since this allowed the minimum p_{T} requirement for muons to be as low as 10 GeV. Using a single muon trigger rather than a single electron trigger, however, would not have allowed us to lower the p_{T} threshold on the electron since the understanding of electron reconstruction and identification performance for candidates with a p_{T} less than 15 GeV was not as well understood as was for muons. Thus, the use of a single electron trigger maximized the signal yield. The selected electron candidate was required to have a $p_{\mathrm{T}} > 16$ GeV, pass the "Medium" electron identification, and satisfy the isolation requirements of $I_{p_{\mathrm{T}}}^{0.4} < 0.06$ and $I_{E_{\mathrm{T}}}^{0.3} < 0.1$, while the selected muon candidate was required to have a $p_{\mathrm{T}} > 10$ GeV, be

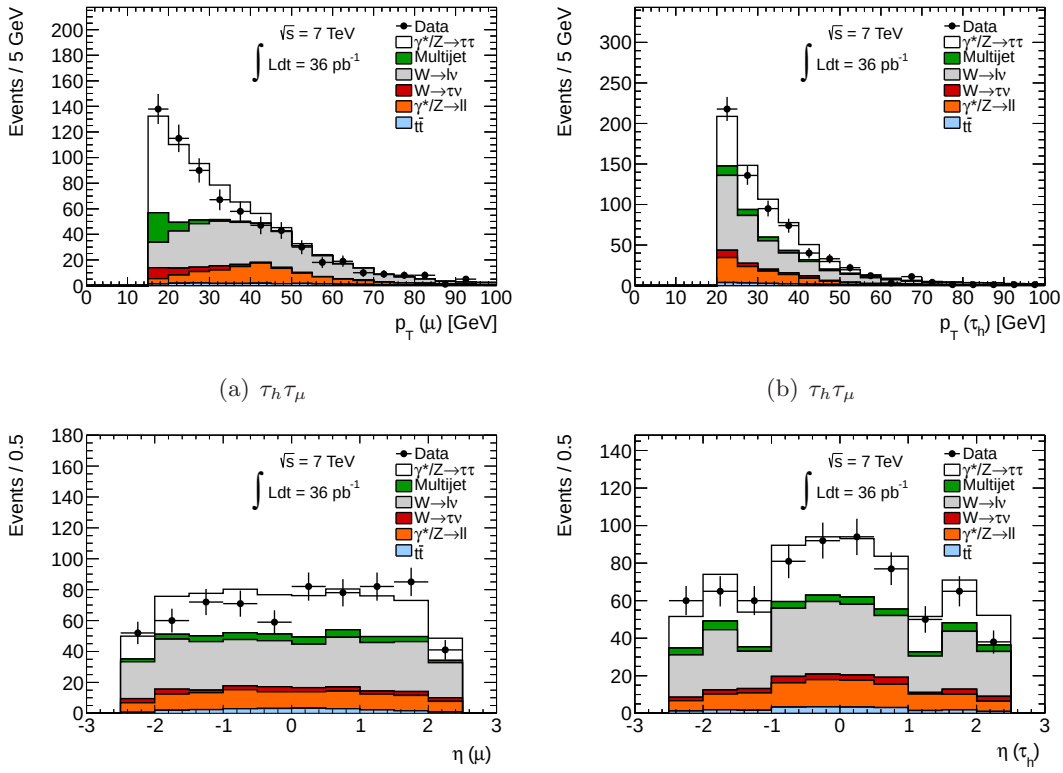

(a) $\tau_h\tau_\mu$ (b) $\tau_h\tau_\mu$

(c) $\tau_h\tau_\mu$ (d) $\tau_h\tau_\mu$

Figure 6.5: The p_{T} (top) and η (bottom) distributions for muons (left) and hadronic tau candidates (right) after the requirement of a selected and isolated muon in conjunction with an identified hadronic tau. Both data and MC are displayed for each plot.

"Combined", and satisfy the isolation requirements of $I_{p_{\mathrm{T}}}^{0.4} < 0.06$ and $I_{E_{\mathrm{T}}}^{0.4} < 0.06$. Distributions of the electron and muon isolation variables can be seen in Figures 6.2 and 6.4, while their kinematic distributions, after the isolation requirements, can be seen in Figure 6.6.

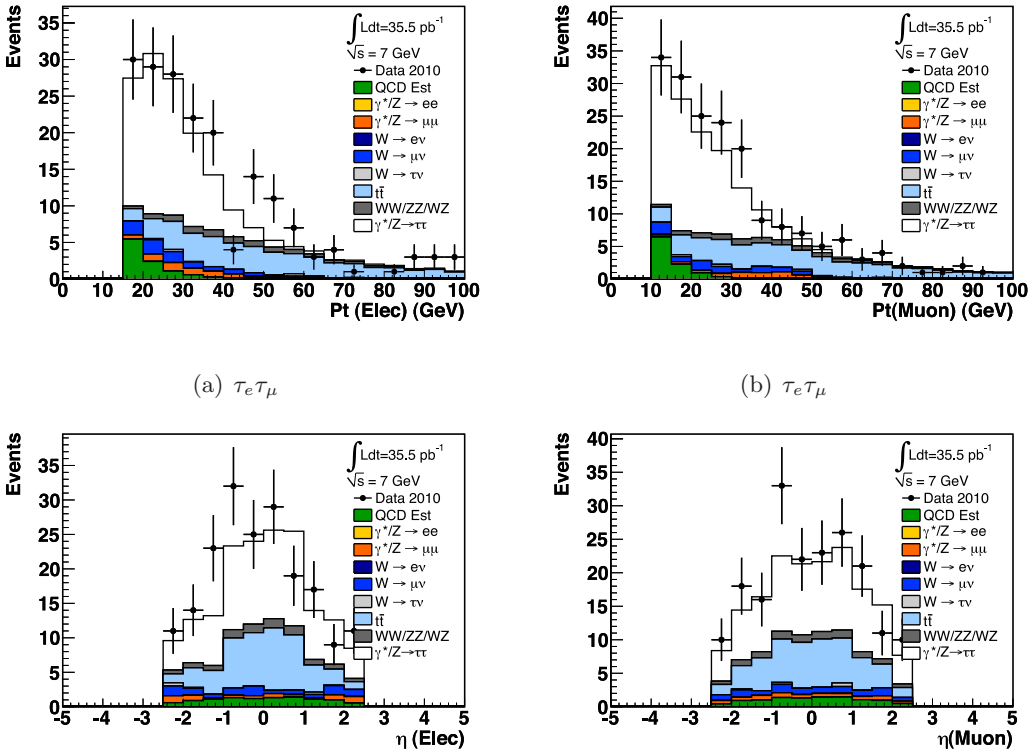

(a) $\tau_e\tau_\mu$ (b) $\tau_e\tau_\mu$

(c) $\tau_e\tau_\mu$ (d) $\tau_e\tau_\mu$

Figure 6.6: The p_{T} (top) and η (bottom) distributions for electrons (left) and muons (right) after the requirement of a selected and isolated electron in conjunction with a selected and identified muon. Both data and MC are displayed for each plot.

6.4.4 $\tau_\mu\tau_\mu$ Final State

The $\tau_\mu\tau_\mu$ final state selection used the same trigger selection as the $\tau_h\tau_\mu$ final state. In addition, exactly two "Combined" muons were required. The lead muon was required to have a p_{T} of at least 15 GeV in accordance with the trigger thresholds, while the second muon was required to have a p_{T} of at least 10 GeV. In order to maximize the signal yield

and since the presence of two muons significantly suppresses the multijet background, looser isolation requirements of $I_{p_{\mathrm{T}}}^{0.4} < 0.15$ and $I_{E_{\mathrm{T}}}^{0.4} < 0.20$ were required for both muons.

6.5 Event Topological Cuts

After the selection of two leptons[3], the multijet background was highly suppressed. The remaining backgrounds were other SM processes, primarily $W \to \ell\nu$, $Z \to \ell\ell(\ell = \mu, e)$, and $t\bar{t}$ processes.

$W \to \ell\nu$+jet[4] events tended to fake the $\tau_h\tau_e$ and $\tau_h\tau_\mu$ final states with the lepton naturally passing the lepton selection criteria, while an associated jet in the event was identified as the hadronic tau candidate. $W \to \mu\nu$+jet events tended to pass the object-selection for the $\tau_e\tau_\mu$ final state when an associated jet was reconstructed as an electron candidate. $W \to e\nu$+jet events would rarely pass full object selection in the $\tau_e\tau_\mu$ final state since jets are rarely reconstructed as muons. Two event level cuts were performed in order to suppress this background: the transverse mass of the lepton and $E_{\mathrm{T}}^{\mathrm{miss}}$ system (m_{T}) defined in equation 6.2, and the angular correlations between the selected objects and the $E_{\mathrm{T}}^{\mathrm{miss}}$ ($\Sigma\cos\Delta(\phi)$) which is defined in equation 6.3.

$$m_{\mathrm{T}} = \sqrt{2p_{\mathrm{T}}(\ell)E_{\mathrm{T}}^{\mathrm{miss}}[1 - \cos(\Delta\phi(\ell, E_{\mathrm{T}}^{\mathrm{miss}}))]} \tag{6.2}$$

$$\Sigma\cos\Delta(\phi) = \cos[\Delta\phi(\ell(e,\mu), E_{\mathrm{T}}^{\mathrm{miss}})] + \cos[\Delta\phi((e/\tau_h), E_{\mathrm{T}}^{\mathrm{miss}})] \tag{6.3}$$

Note that in the second term of equation 6.3, the choice of e vs τ_h is dependent on whether the final state is $\tau_h\tau_e/\tau_h\tau_\mu$or $\tau_e\tau_\mu$.

The $\gamma^*/Z \to \ell\ell$ decays were a major background in all four final states. There were two ways in which $\gamma^*/Z \to \ell\ell$ decays could fake the three non-$\tau_\mu\tau_\mu$ final states: a lepton was reconstructed as a hadronic tau candidate, or an associated jet in the event was reconstructed as a hadronic tau or an electron. The main method to veto hadronic tau candidates that are truly leptons was through the overlap removal procedure (Section 6.2). Additionally there

[3]Here the two leptons refer to the ditau decay products including the hadronic tau.

[4]The lepton may be an electron or muon directly from the W boson, or an electron or muon from a leptonic tau decay which in turn decayed directly from the W. Events where the W boson decays to a hadronic tau were found to be a negligible background.

was a dedicated tight electron veto imposed on all hadronic tau candidates. For the case where an associated jet passes either tau or electron identification, a dilepton veto (DLV) was used to suppress those events. The DLV for the non $\tau_\mu\tau_\mu$ final states, along with the dimuon requirement for the $\tau_\mu\tau_\mu$ final state, was defined as:

- $\tau_h\tau_e$, $\tau_h\tau_\mu$[5]: $N_e + N_\mu = 1$
- $\tau_e\tau_\mu$: $N_e = 1$ and $N_\mu = 1$
- $\tau_\mu\tau_\mu$: $N_\mu = 2$

By ensuring consistent definitions of N_e and N_μ among the four final states, the DLV also ensured that each final state selection was mutually exclusive.

The $\gamma^*/Z \to \mu\mu$ background was overwhelming in the $\tau_\mu\tau_\mu$ final state due to the presence of two isolated muons. This background was suppressed with a boosted decision tree (Section 6.5.3).

$t\bar{t}$ decays also proved to be a substantial background when one of the W bosons would decay leptonically, providing events rich with isolated leptons and jets that could potentially be reconstructed as hadronic taus or electrons. The $\tau_e\tau_\mu$ final state suffered the most from this background. To remove these events, the scalar sum of transverse energy, ΣE_{T}, was constructed out of the selected leptons, jets, and the $E_{\mathrm{T}}^{\mathrm{miss}}$:

$$\Sigma E_{\mathrm{T}} = E_{\mathrm{T}}(e) + p_{\mathrm{T}}(\mu) + \Sigma_{\mathrm{jets}} p_{\mathrm{T}} + E_{\mathrm{T}}^{\mathrm{miss}} \tag{6.4}$$

and required to be less than 150 GeV. There were no dedicated cuts to remove $t\bar{t}$ events in the $\tau_h\tau_e$, $\tau_h\tau_\mu$, and $\tau_\mu\tau_\mu$ final states since its background levels were relatively small. Table 6.2 summarizes the different event level cuts that were applied in each final state.

6.5.1 $\tau_h\tau_e$ and $\tau_h\tau_\mu$ Final States

After the lepton and hadronic tau selection, events were further selected if the DLV was satisfied, if the $m_{\mathrm{T}} < 50$ GeV, if the $\Sigma\cos\Delta(\phi) > -0.15$, and if the visible mass (m_{vis}) of

[5]Preselected, rather than selected, lepton objects are counted in the DLV in order to maximize the $Z \to \ell\ell$ rejection.

Final State	Event Requirements
$\tau_h\tau_\ell$	$N_e + N_\mu = 1$
	$m_{\mathrm{T}} < 50$ GeV
	$\Sigma\cos\Delta(\phi) > -0.15$
	$35 < m_{\mathrm{vis}} < 75$ GeV
	$N_{\mathrm{trk}} = 1$ or 3
$\tau_e\tau_\mu$	$N_e = 1$ and $N_\mu = 1$
	$\Sigma\cos\Delta(\phi) > -0.15$
	$25 < m_{\mathrm{vis}} < 80$ GeV
$\tau_\mu\tau_\mu$	$N_\mu = 2$
	$25 < m_{\mathrm{vis}} < 65$ GeV

Table 6.2: All event level cut requirements imposed on each $\tau\tau$ final state. In addition each final state requires that the two selected leptons have opposite electric charge.

the lepton tau pair fell with the range $35 < m_{\mathrm{vis}} < 75$ GeV. Further cuts were then made on the hadronic tau candidate to ensure that it had a unit charge and either one or three associated tracks. The final requirement for an event passing the $\tau_h\tau_\ell$ selection was that the electric charge of the hadronic tau and the lepton had opposite signs. A total of 151 and 213 data events were selected in the $\tau_h\tau_e$ and $\tau_h\tau_\mu$ final states, respectively. Data vs MC distributions of the lepton and hadronic tau kinematic distributions are shown in Figure 6.7, while the m_{T} and the $\Sigma\cos\Delta(\phi)$ distributions are shown in Figure 6.8. In addition, the final hadronic tau track distributions, which highlight the signal purity, as well as the m_{vis} distributions are shown in Figure 6.9. All figures are displayed after the full selection, except for the specific variable that was plotted. The multijet background, displayed along with the MC, was determined from data, while the $W \to \ell\nu$ background shape was taken from simulation but scaled to data (Section 7).

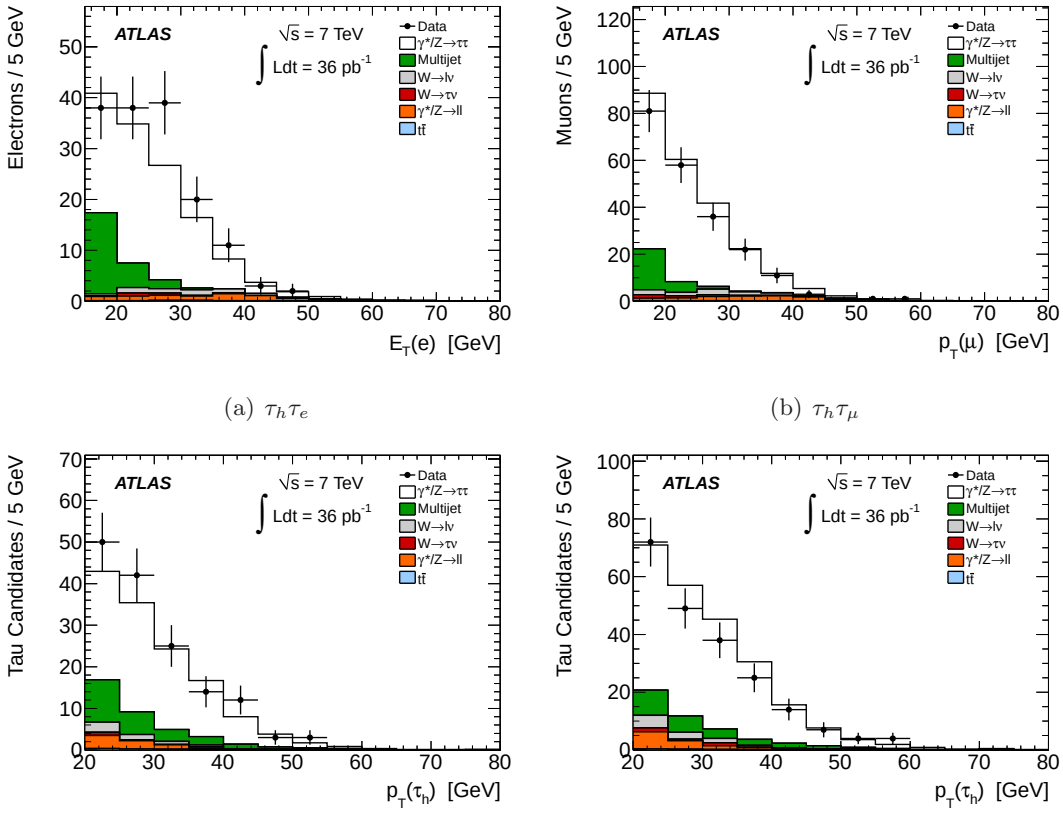

(a) $\tau_h\tau_e$ (b) $\tau_h\tau_\mu$

(c) $\tau_h\tau_e$ (d) $\tau_h\tau_\mu$

Figure 6.7: The final p_{T} distributions for leptons (e/μ) (top) and hadronic tau candidates (bottom) after full event selection in the $\tau_h\tau_e$ final state (left) and the $\tau_h\tau_\mu$ final state (right). Both data and MC are displayed for each plot.

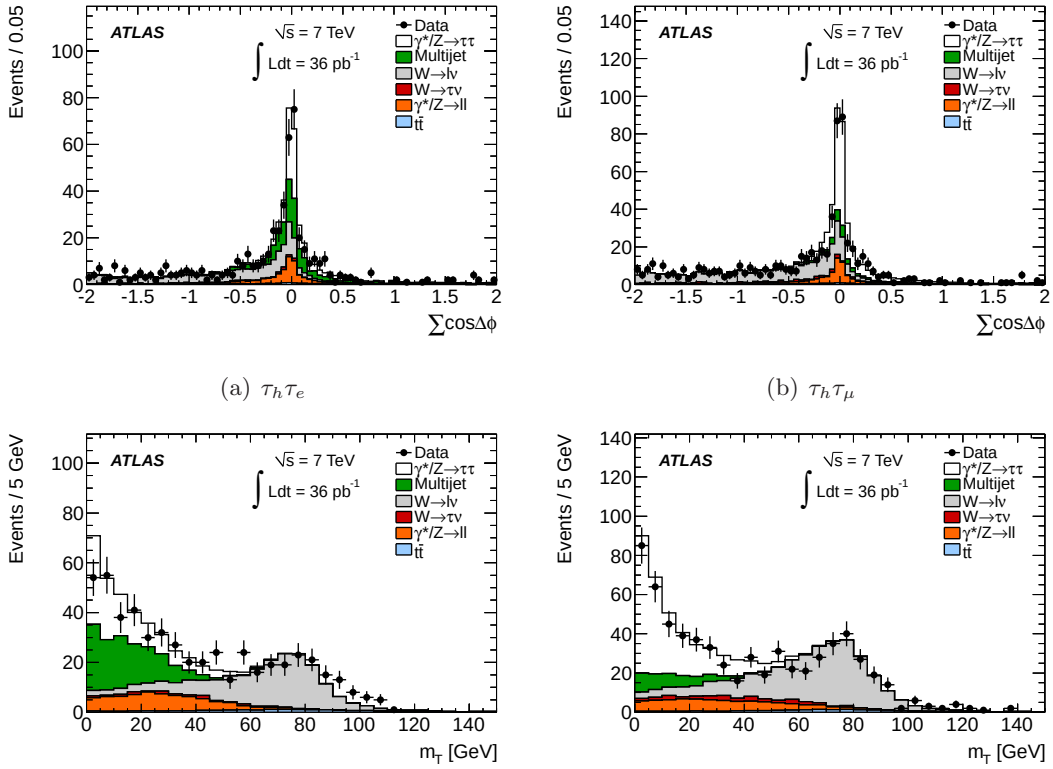

(a) $\tau_h\tau_e$ (b) $\tau_h\tau_\mu$

(c) $\tau_h\tau_e$ (d) $\tau_h\tau_\mu$

Figure 6.8: Distributions of the $\Sigma\cos\Delta(\phi)$ (top) and m_{T} (bottom) in the $\tau_h\tau_e$ (left) and $\tau_h\tau_\mu$ (right) final states after full event selection, except for a cut on the specific variable itself. These two variables are used to suppress contamination from $W \to \ell\nu$+Jets events. Both data and MC are displayed for each plot.

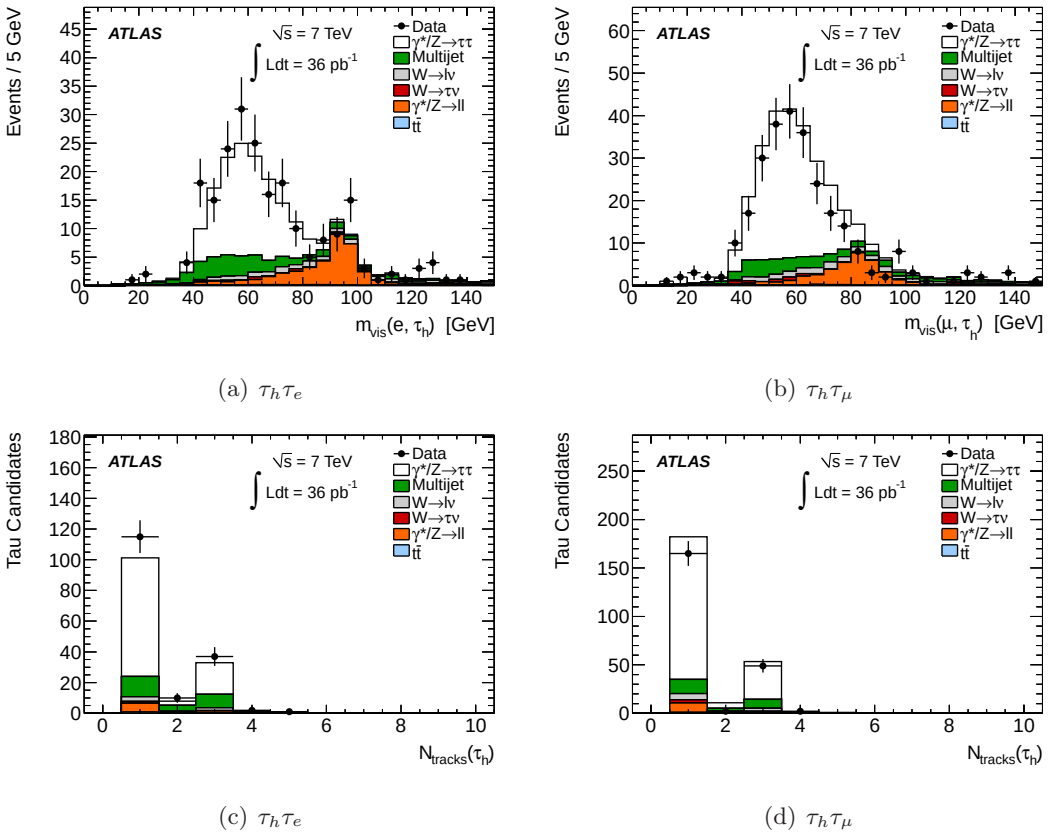

(a) $\tau_h\tau_e$ (b) $\tau_h\tau_\mu$

(c) $\tau_h\tau_e$ (d) $\tau_h\tau_\mu$

Figure 6.9: The m_{vis} (top) and tau track (bottom) distributions in the $\tau_h\tau_e$ (left) and $\tau_h\tau_\mu$ (right) final states after full event selection, except for a cut on the specific variable itself. Both data and MC are displayed for each plot.

6.5.2 $\tau_e\tau_\mu$ Final State

After the selection of an isolated electron and muon with opposite charge, events were further required to have no additional preselected leptons. The main backgrounds remaining were the $t\bar{t}$, diboson, and W/Z+jets backgrounds. The $t\bar{t}$ backgrounds were highly suppressed with a cut on the $\Sigma E_{\mathrm{T}} < 150$ GeV, while a cut on $\Sigma\cos\Delta(\phi) > -0.15$ removed most of the W/Z+jets background. All candidate events were further required to have a dilepton visible mass within $25 < m_{\mathrm{vis}} < 80$ GeV. A total of 85 events passed all signal selection. The $\Sigma\cos\Delta(\phi)$, ΣE_{T}, and m_{vis} distributions are shown in Figure 6.11, while the basic kinematic distributions of the leptons are shown in Figure 6.10. Determination of the multijet background, and MC background validation is discussed in Section 7.

6.5.3 $\tau_\mu\tau_\mu$ Final State

After the selection of two isolated muons with opposite charge, the overwhelming background for the $\tau_\mu\tau_\mu$ final state came from $\gamma^*/Z \to \mu\mu$ events (Figure 6.13). Two methods were investigated to suppress this background: a simple cuts analysis and a Boosted Decision Tree (BDT) [54]. The BDT was ultimately chosen since there was little statistical significance in the simple cuts analysis. The variables used in both methods were (in decreasing order of BDT rank), labeling the leading muon as μ_1 and the sub-leading muon as μ_2:

- $|d_0(\mu_1)| + |d_0(\mu_2)|$**:**
  The d_0 is a measure of the point of closest approach in the plane transverse to the beam of the muons track with the reconstructed PMV. Since the tau lepton will travel a short distance before decay, the measured d_0 of the reconstructed track of its decay should, on average, be larger than the d_0 of a track resulting from the decay of a muon directly from the γ^*/Z.

- $\Delta p_{\mathrm{T}}(\mu_1, \mu_2)$**:**
  Since the boost of $\gamma^*/Z \to \mu\mu$ events is small in the plane transverse to the beam, the difference in p_{T} of the two muons should be small, while the difference in p_{T} of the

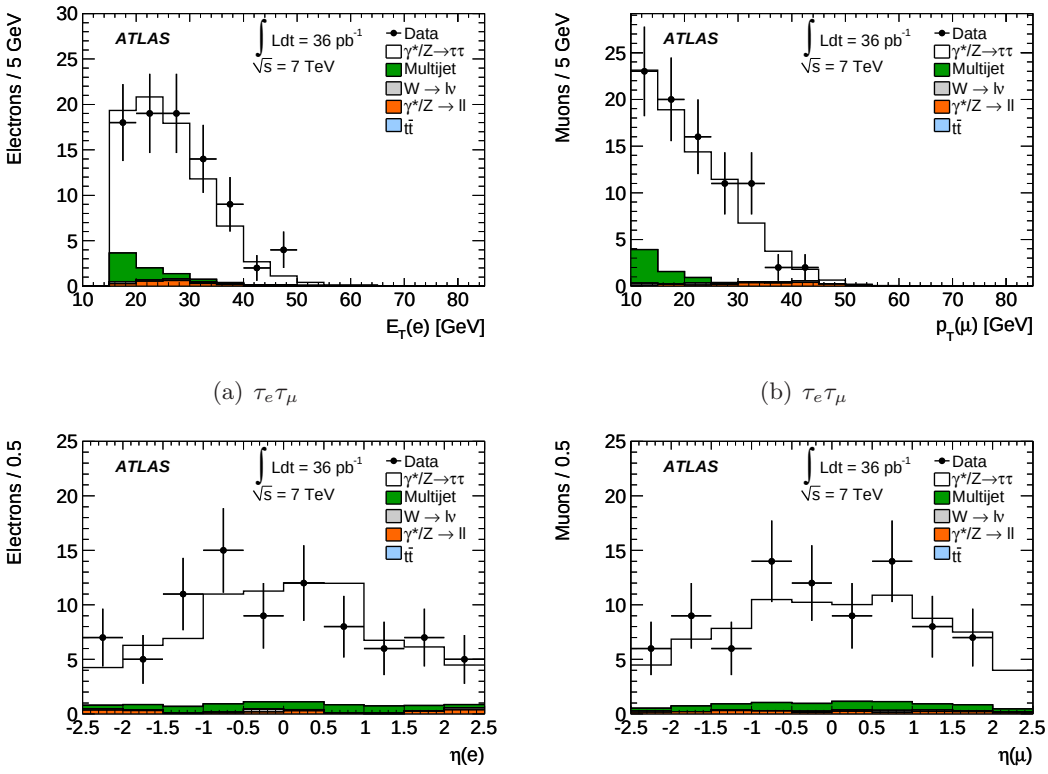

(a) $\tau_e\tau_\mu$

(b) $\tau_e\tau_\mu$

(c) $\tau_e\tau_\mu$

(d) $\tau_e\tau_\mu$

Figure 6.10: The electron (left) and muon (right) p_{T} (top) and η (bottom) distributions after full event selection in the $\tau_e\tau_\mu$ final state. Both data and MC are displayed for each plot.

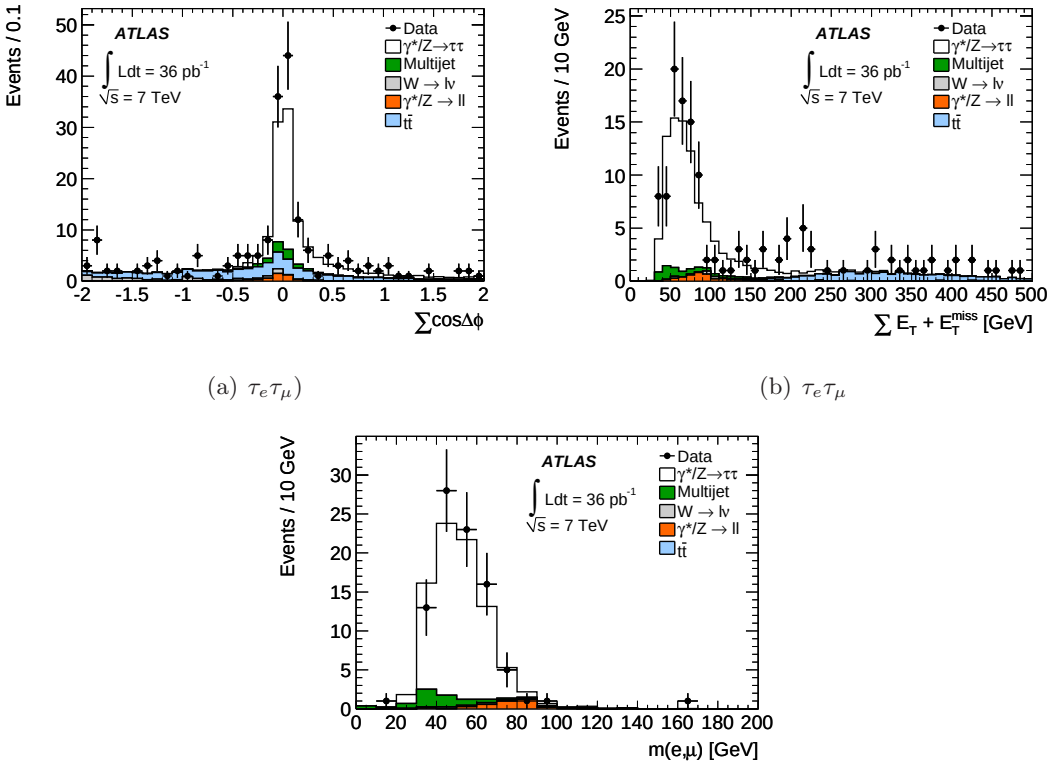

(a) $\tau_e\tau_\mu$)

(b) $\tau_e\tau_\mu$

(c) $\tau_e\tau_\mu$

Figure 6.11: The $\Sigma\cos\Delta(\phi)$ (top left), the ΣE_{T} (top right), and the m_{vis} (bottom) distributions in the $\tau_e\tau_\mu$ final state after full event selection, except for a cut on the specific variable itself. Both data and MC are displayed for each plot.

two muons in $Z \rightarrow \tau_\mu \tau_\mu$ events can differ depending on the momentum fraction the original tau lepton imparts on the muon due to the nature of the three body decay $\tau \rightarrow \mu \nu_\tau \nu_\mu$.

- $p_{\mathrm{T}}(\mu_1)$**:**
  The p_{T} of muons decaying directly from the Z boson will, on average, by larger than that of tau leptons decaying to muons.

- $\Delta\phi(\mu_1, E_{\mathrm{T}}^{\mathrm{miss}})$**:**
  The $E_{\mathrm{T}}^{\mathrm{miss}}$ in $\gamma^*/Z \rightarrow \mu\mu$ events is largely fake and caused by detector effects and should be randomly distributed in ϕ, while the $E_{\mathrm{T}}^{\mathrm{miss}}$ in $Z \rightarrow \tau_\mu \tau_\mu$ events is real and tends to be either aligned or anti-aligned with the leading muon.

- $\Delta\phi(\mu_1, \mu_2)$**:**
  Although weakest in BDT rank, this variable still provided some separation power between signal and $\gamma^*/Z \rightarrow \mu\mu$.

Distributions of $\Delta\phi(\mu_1, E_{\mathrm{T}}^{\mathrm{miss}})$, $\Delta\phi(\mu_1, \mu_2)$, $\Delta p_{\mathrm{T}}(\mu_1, \mu_2)$, and $|d_0(\mu_1)| + |d_0(\mu_2)|$ are depicted in Figure 6.12

The BDT was trained using only $Z \rightarrow \tau_\mu \tau_\mu$ and $\gamma^*/Z \rightarrow \mu\mu$ MC as inputs in order to maximize the separation power. The events entering the BDT were only required to have two selected muons with opposite sign whose invariant mass fell in the window $25 < m_{\mu\mu} < 65$ GeV. The training was done on a subset of MC events, and validated on another set of events. The BDT output distribution is shown in Figure 6.14 along with the final invariant mass distribution after a cut on the BDT score of 0.07. In all a total of 90 data events passed all signal selection requirements.

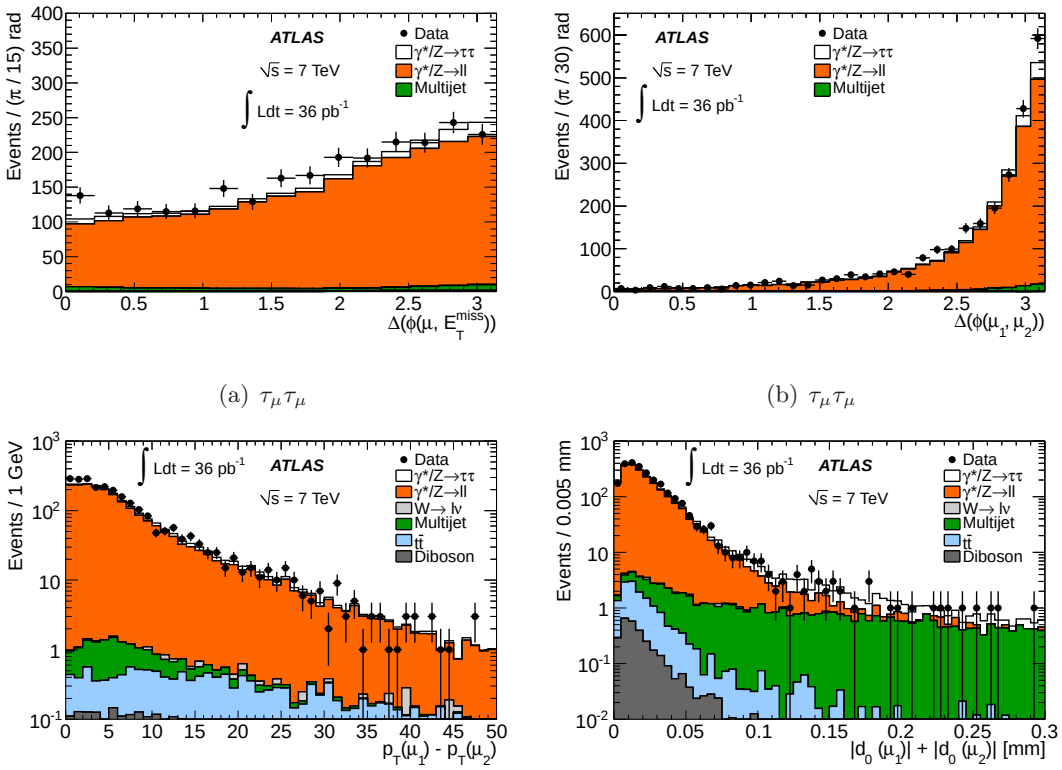

(a) $\tau_\mu\tau_\mu$ (b) $\tau_\mu\tau_\mu$

(c) $\tau_\mu\tau_\mu$ (d) $\tau_\mu\tau_\mu$

Figure 6.12: Variables used as input to the BDT used to separate $\gamma^*/Z \to \mu\mu$ events from $\tau_\mu\tau_\mu$ final state events. Going in order from (a) through (d): $\Delta\phi(\mu_1, E_{\mathrm{T}}^{\mathrm{miss}})$, $\Delta\phi(\mu_1, \mu_2)$, $\Delta p_{\mathrm{T}}(\mu_1, \mu_2)$, and $|d_0(\mu_1)| + |d_0(\mu_2)|$. Not shown is the lead μ p_{T}. Both data and MC are displayed for each plot.

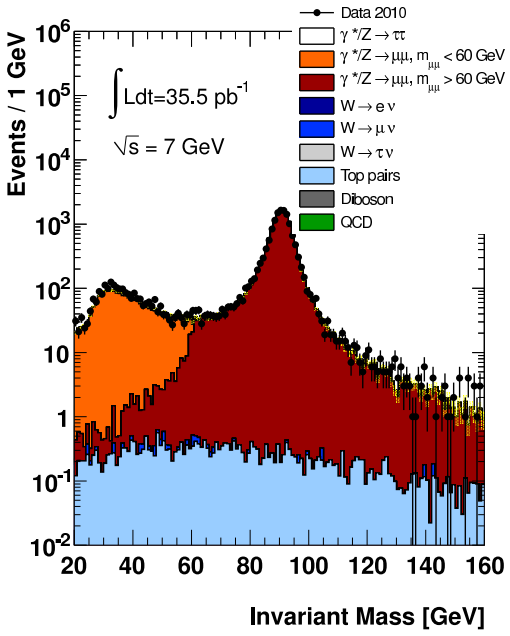

Figure 6.13: The m_{vis} distribution in the $\tau_\mu\tau_\mu$ final state after the selection of two isolated muons with opposite electric charge. The vast majority of events are from $\gamma^*/Z \to \mu\mu$ processes. Both data and MC are displayed for each plot.

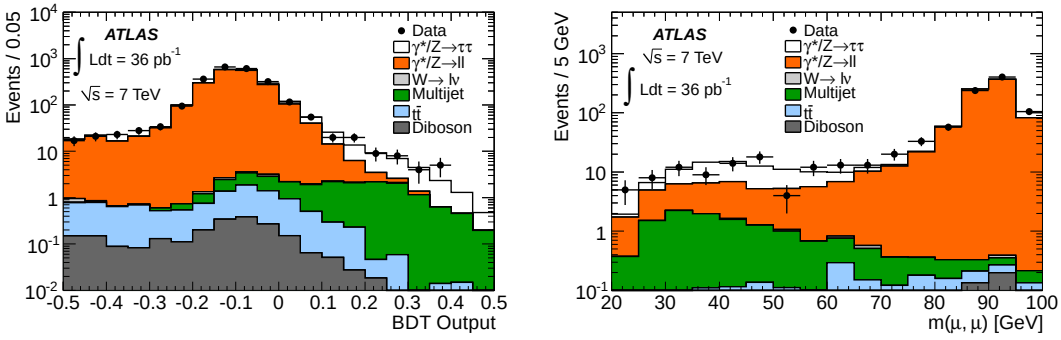

(a) $\tau_\mu\tau_\mu$ (b) $\tau_\mu\tau_\mu$

Figure 6.14: Figure (a) shows the final BDT output score for all data and MC in the $\tau_\mu\tau_\mu$ final state, while figure (b) shows the final invariant mass distribution of the two muons after a cut on the BDT score of 0.07. Both data and MC are displayed for each plot.

Chapter 7

BACKGROUND ESTIMATION

The cross-section for multijet events is more than a million times greater than the expected $Z \rightarrow \tau\tau$ cross-section making it technically difficult to fully simulate a statistically significant number of multijet events. Further, the absolute scale of the multijet cross-section was not well understood at the time of this study. Rather than relying on simulated MC samples, a data-driven two-dimensional side-band method (ABCD) was employed to determine the multijet background in all four final states. In an ABCD method, four regions are defined: a signal region (A), and three control regions (BCD) based on the distributions of two variables (Figure 7.1).

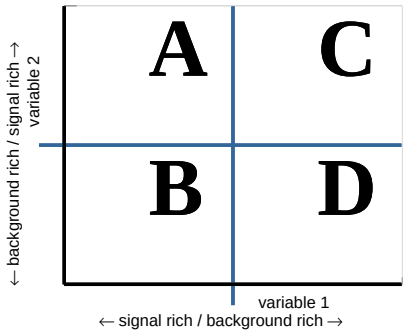

Figure 7.1: In an ABCD method data events are split into four regions: a signal rich region (A) and three background rich control regions (BCD). The ratio of events in background rich regions C and D is extrapolated to the number of events in region A normalized to the number of events in region B assuming that the two variables are independent.

Assuming that the four regions are defined by two independent variables, then the ratio of the number of background events in regions C to D should equal the ratio of the number of background events in regions A to B:

$$\frac{N_{\mathrm{A}}}{N_{\mathrm{B}}} = \frac{N_{\mathrm{C}}}{N_{\mathrm{D}}} \tag{7.1}$$

Thus if the signal and EWK contamination in regions BCD is negligible, the total number of multijet (MJ) events in region A can be estimated as:

$$N_{\mathrm{MJ}} = N_{\mathrm{A}} = \frac{N_{\mathrm{B}} N_{\mathrm{C}}}{N_{\mathrm{D}}}. \tag{7.2}$$

In practice, the three control regions contain some signal and EWK background. Taking into account the signal and EWK contamination, equation 7.2 can be rewritten as:

$$N_{\mathrm{MJ}} = N_{\mathrm{A}} = \frac{(N_{\mathrm{B}} - N_{\mathrm{B}}^{\mathrm{EWK}} - N_{\mathrm{B}}^{\mathrm{signal}})(N_{\mathrm{C}} - N_{\mathrm{C}}^{\mathrm{EWK}} - N_{\mathrm{C}}^{\mathrm{signal}})}{N_{\mathrm{D}} - N_{\mathrm{D}}^{\mathrm{EWK}} - N_{\mathrm{D}}^{\mathrm{signal}}} \tag{7.3}$$

The events in the two $\tau_h\tau_\ell$ final states were split into four regions depending on whether the lepton was isolated or anti-isolated and whether the $\tau_h\tau_\ell$ pair had opposite-signed (OS) electric charges or same-signed (SS) electric charges (Figure 7.2(a)). The events in the $\tau_e\tau_\mu$ final state, likewise, were split into four regions based on whether the $\tau_e\tau_\mu$ pair was OS or SS and whether both leptons were isolated, or whether both leptons were anti-isolated. Since the requirement of two muons in the $\tau_\mu\tau_\mu$ final state enriched events containing heavy flavor decays, the events were instead split into four regions depending upon whether the lead muon (μ_1) was isolated or anti-isolated and whether the sub-leading muon (μ_2) was isolated or anti-isolated (Figure 7.2(b)). In all cases, for a lepton to be isolated it must have passed both the calorimeter ($I^X_{E_{\mathrm{T}}}$) and the tracker ($I^X_{p_{\mathrm{T}}}$) isolation cuts, while to be anti-isolated, the lepton must have simultaneously failed both isolation requirements described in Sections 6.4.1-6.4.4.

The following three sections describe in more detail the background estimation methods used in the two semileptonic final states, the $\tau_e\tau_\mu$ final state, and finally the $\tau_\mu\tau_\mu$ final state.

7.1 $\tau_h\tau_\ell$ *Final State Background Estimation*

7.1.1 W+Jets Normalization

In addition to determining the multijet background, MC simulation is also verified for the W+Jets backgrounds. It was found that the rate of generic jets passing hadronic tau identification was underestimated in simulation due primarily to the width of the hadronic tau candidate measured in the EM calorimeter (R_{EM}) being more narrow in data than in

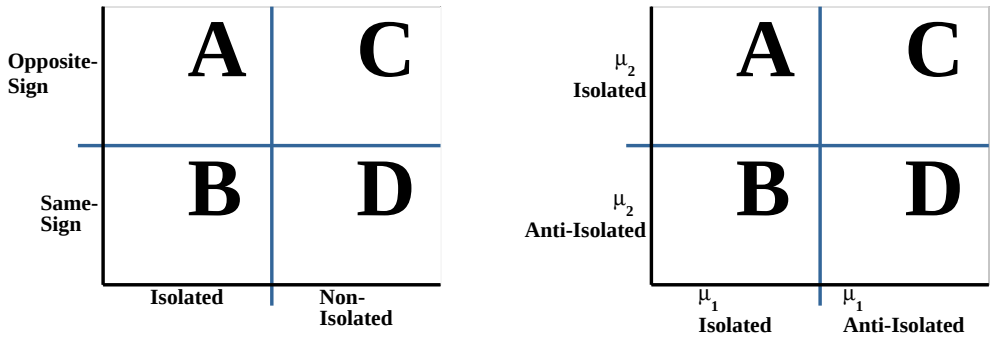

(a) (b)

Figure 7.2: The figure on the left shows the signal region (A) and the 3 control regions (BCD) that were used to estimate the multijet background in the $\tau_h\tau_e$, $\tau_h\tau_\mu$, and $\tau_e\tau_\mu$ final states, while the figure on right shows the four regions for the $\tau_\mu\tau_\mu$ final state.

simulation [55]. In order to correct for this effect, a W control region was defined in which the cuts on m_{T} and $\Sigma\cos\Delta(\phi)$ were inverted, while all other cuts, save the m_{vis} window, were kept. A correction factor, k_w, was then defined as the ratio of events that pass "Tight" tau identification in the W control region in data versus MC (equation 7.4).

$$k_w = \frac{N_W^{\tau-\mathrm{id}}(\mathrm{Data})}{N_W^{\tau-\mathrm{id}}(\mathrm{MC})} \tag{7.4}$$

The k_w values were computed for the case where the hadronic tau candidate had one associated track, three associated tracks, or one or three associated tracks. No deviation larger than the statistical uncertainty on each measurement was observed. The k_w was observed, however, to depend on whether the event was OS or SS.

Figure 7.3 shows the muon and hadronic tau p_{T} distributions before and after the application of "Tight" tau identification in the W control region. Although the overall scale

is low, the shape seems to agree well with the data. This allows the use of the k_w factors:

$$\begin{aligned} k_w^{\mathrm{OS}}(\tau_h\tau_e) &= 0.63 \pm 0.07 \\ k_w^{\mathrm{SS}}(\tau_h\tau_e) &= 0.83 \pm 0.15 \\ k_w^{\mathrm{OS}}(\tau_h\tau_\mu) &= 0.73 \pm 0.06 \\ k_w^{\mathrm{SS}}(\tau_h\tau_\mu) &= 0.94 \pm 0.13 \end{aligned} \tag{7.5}$$

to normalize the W background.

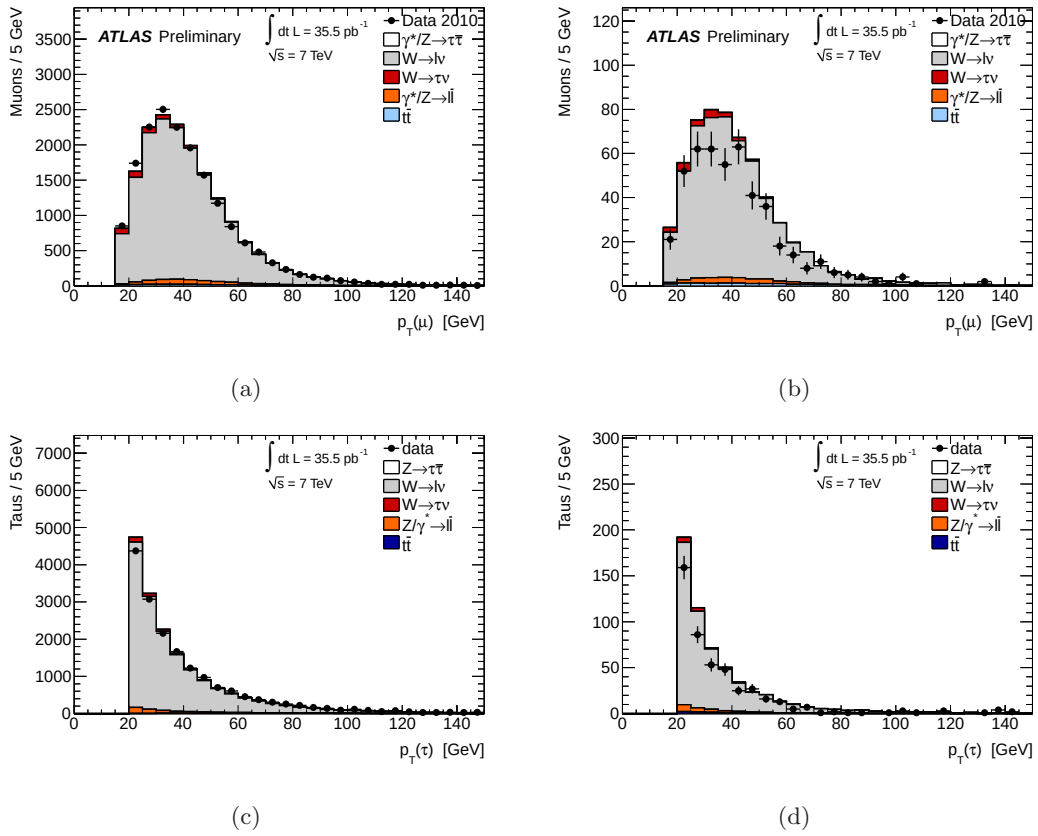

Figure 7.3: The muon (top) and hadronic tau candidate (bottom) p_{T} distributions before (left) and after (right) the application of "Tight" tau identification. The data MC agreement is reasonable before tau identification, however, the simulation predicts that too many events will pass tau identification. The k_w were factors used to correct for this discrepancy.

7.1.2 Multijet Estimation

Figure 7.4 shows the events, after all cuts in the $\tau_h\tau_\mu$ final state, split into four regions depending on whether the muon and the hadronic tau candidate have the same or opposite electric charge and whether the muon is isolated or not isolated. The isolation/non-isolation definition in Figure 7.4(b), discussed above, produced a discontinuous structure between the boundaries since events where a muon satisfied one isolation requirement, but not the other fit into neither category. Figure 7.4(a) shows how the events would be dispersed based on a continuous variable ($I^{0.4}_{E_T}$). In either case the relative signal contributions were small in regions BC and D which in turn minimized the dependence of the background estimation method on the cross-section of the process we measured.

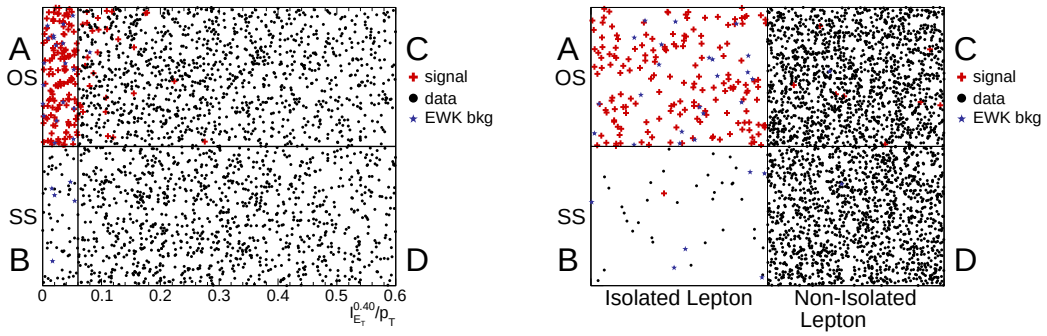

(a) (b)

Figure 7.4: The left figure displays all events split into four regions depending on whether the lepton and tau have the same or opposite electric charge and by the relative calorimeter isolation. The ABCD method used in this analysis, however, split events based on whether the selected lepton passed both tracker and calorimeter isolation or failed both isolation requirements (right). In both plots, the points can either be signal, electroweak background, or multijet background (actually simply data). The data points are not shown in region A since it will be dominated by signal and EWK backgrounds. To estimate the multijet background in region A, the ratio of data events in regions C to D normalized to the number of events in region B, after signal and electroweak subtraction, is computed.

The multijet background was predicted after all selection requirements since region B, isolated lepton/SS events, had a reasonable amount of statistics. Equation 7.2 can be

rewritten as:

$$N_{\mathrm{MJ}}^{\mathrm{A}} = N_{\mathrm{MJ}}^{\mathrm{B}} * R_{\mathrm{OS/SS}}$$
$$N_{\mathrm{MJ}}^{\mathrm{OS}} = N_{\mathrm{MJ}}^{\mathrm{SS}} * R_{\mathrm{OS/SS}} \tag{7.6}$$

where $R_{\mathrm{OS/SS}}$ is the predicted ratio of OS to SS multijet events in data as measured in the anti-isolated regions, C and D. For clarity, $N_{\mathrm{MJ}}^{\mathrm{A/B}}$ has been replaced by $N_{\mathrm{MJ}}^{\mathrm{OS/SS}}$. The measured values of $R_{\mathrm{OS/SS}}$ for the $\tau_h\tau_e$ and $\tau_h\tau_\mu$ channels were:

$$R_{\mathrm{OS/SS}} = \begin{cases} 1.07 \pm 0.07 \text{ (stat.)} \ \pm 0.07 \text{ (sys.)}, & \tau_h\tau_e \\ 1.07 \pm 0.04 \text{ (stat.)} \ \pm 0.04 \text{ (sys.)}, & \tau_h\tau_\mu. \end{cases} \tag{7.7}$$

The systematic uncertainty on $R_{\mathrm{OS/SS}}$ was estimated by measuring the dependence of $R_{\mathrm{OS/SS}}$ on lepton isolation (Section 9.4).

As can be seen in the 'non-isolated' columns of Table 7.1, the EWK/$t\bar{t}$ contribution was negligible when computing $R_{\mathrm{OS/SS}}$. When finally computing $N_{\mathrm{MJ}}^{\mathrm{OS}}$, all EWK/$t\bar{t}$ background contamination in region B ($N_{\mathrm{MJ}}^{\mathrm{SS}}$) had to be removed using simulation (normalized to data in the case of W+Jets). The effect on the uncertainties of the EWK/$t\bar{t}$ contamination in the three control regions are fully explored in Section 9. The main assumption with the method itself is that the ratio of OS to SS events was independent of whether the lepton was isolated or anti-isolated. This systematic uncertainty is discussed in Section 9.4.

The multijet background in the final signal region was predicted to be:

$$N_{\mathrm{MJ}}^{\mathrm{OS}} = \begin{cases} 25 \pm 6 \text{ (stat.)} \ \pm 3 \text{ (sys.)}, & \tau_h\tau_e \\ 23 \pm 6 \text{ (stat.)} \ \pm 4 \text{ (sys.)}, & \tau_h\tau_\mu. \end{cases} \tag{7.8}$$

All other backgrounds were estimated from simulation (where the W+Jets background was normalized to data).

7.2 $\tau_e\tau_\mu$ Final State Background Estimation

The $\tau_e\tau_\mu$ final state used the same ABCD method as the two semileptonic final states ($\tau_h\tau_\ell$), eqn. 7.6, in order to estimate the multijet background. The actual ABCD calculation was

		$\tau_h\tau_e$ channel		$\tau_h\tau_\mu$ channel	
		isolated lepton	non-isolated lepton	isolated lepton	non-isolated lepton
		region A	region C	region A	region C
	data	151(12)	398(20)	213(15)	1521(39)
	$Z \to \tau\tau$	97(1)	3.2(2)	185(2)	8.4(4)
	$\gamma \to \tau\tau$	0.3(2)	0(0)	0.7(3)	0.05(5)
OS Events	Multijet	23(6)	394(20)	24(6)	1511(39)
+ final selection	$W \to \ell\nu$	4.8(4)	0.2(1)	9.3(7)	0.3(1)
	$W \to \tau\nu$	1.5(4)	0.04(4)	3.6(8)	0.08(8)
	$Z \to \ell\ell$	4.9(2)	0.12(3)	8.7(3)	0.33(6)
	$\gamma \to \ell\ell$	2.0(3)	0.03(3)	2.4(4)	0.16(8)
	$t\bar{t}$	1.02(8)	0.11(3)	1.3(1)	0.99(8)
	Diboson	0.18(1)	0.009(3)	0.28(2)	0.052(8)
		region B	region D	region B	region D
	data	29(5)	367(19)	34(6)	1415(38)
	$Z \to \tau\tau$	1.0(1)	0.23(7)	1.3(2)	0.3(8)
	$\gamma \to \tau\tau$	0.2(1)	0(0)	0.06(6)	0.09(9)
SS Events	Multijet	21(5)	367(19)	22(6)	1413(38)
+ final selection	$W \to \ell\nu$	2.3(3)	0(0)	3.7(5)	0.09(6)
	$W \to \tau\nu$	0.3(3)	0(0)	2.1(7)	0.2(2)
	$Z \to \ell\ell$	2.7(3)	0.05(2)	1.9(1)	0.11(3)
	$\gamma \to \ell\ell$	1.3(3)	0.13(11)	2.5(4)	0.11(8)
	$t\bar{t}$	0.1(3)	0.06(18)	0.21(4)	0.61(6)
	Diboson	0.029(5)	0.005(3)	0.044(7)	0.021(4)

Table 7.1: Number of events in each region for the two semileptonic final states. The numbers in parenthesis are the statistical uncertainties in the least significant digit[s]. The multijet expectations are determined by the data-driven method discussed in that section. All other processes were estimated with Monte Carlo (normalized to data in the case of W+Jets).

not done after full event selection, as was done for the $\tau_h\tau_\ell$ final state, since there were nearly no events in the isolated leptons/SS region after the visible mass requirement. Instead, the multijet contribution in region A was estimated after the dilepton-veto requirement and the contribution after full signal selection was:

$$N_{\rm MJ}^{\rm OS}(\text{full-selection}) = N_{\rm MJ}^{SS} \times R_{\rm OS/SS} \times \epsilon_{\rm MJ} \tag{7.9}$$

where $\epsilon_{\rm MJ}$ was the efficiency for events to pass the $\Sigma\cos\Delta(\phi)$, $\Sigma E_{\rm T}$, and the visible mass window requirements calculated in region D (SS anti-isolated).

All EWK/$t\bar{t}$ samples were estimated from simulation. The normalizations of the two largest backgrounds, W+Jets, and $t\bar{t}$ were verified in data using control regions that enhanced the respective signals. No deviation larger than the statistical uncertainties were observed. Table 7.2 shows the final signal and background contributions in all four regions after the dilepton-veto requirement.

The total multijet contribution in the final signal region was estimated as:

$$N_{\rm MJ}^{\rm OS} = 5.7 \pm 4.1(\text{stat.}) \pm 0.9(\text{sys.}). \tag{7.10}$$

while the measured $R_{\rm OS/SS}$ value was:

$$R_{\rm OS/SS} = 1.55 \pm 0.04(stat.) \pm 0.20(sys.). \tag{7.11}$$

Where the systematic uncertainty on $R_{\rm OS/SS}$, like the $\tau_h\tau_\ell$ final states, was evaluated by measuring the dependence of $R_{\rm OS/SS}$ on the isolation of the two leptons (Section 9.4).

7.3 $\tau_\mu\tau_\mu$ Final State Background Estimation

The $\tau_\mu\tau_\mu$ final state did not use the OS/SS regions since the expected multijet background was mostly from heavy flavor (c/b) meson decays which is OS biased. Instead, the multijet background was predicted based on whether the lead muon was isolated/anti-isolated and whether the sub-leading muon was isolated/anti-isolated (Figure 7.2(b)). The multijet background was predicted before the BDT requirement using:

$$N_A^{\rm MJ} = N_B \times \frac{N_C}{N_D} \times k \tag{7.12}$$

		isolated	non-isolated
		region A	region C
	data	190(14)	22(5)
	$\gamma^*/Z(\tau\tau)$	86.9(1.2)	1.4(2)
OS Events	Multijet	10(7)	6.59
+ dilepton selection	$W(e\nu)$	0.22(11)	0.11(7)
	$W(\mu\nu)$	9.2(6)	9.6(7)
	$W(\tau\nu)$	1.0(4)	0.50(3)
	$\gamma^*/Z(ee)$	0.06(2)	0.05(3)
	$\gamma^*/Z(\mu\mu)$	5.5(2)	2.81(15)
	$t\bar{t}$	48.7(5)	0.38(4)
	Diboson	9.11(13)	0.55(2)
		isolated	non-isolated
		region B	region D
	data	3771(61)	2432(49)
	$\gamma^*/Z(\tau\tau)$	0.61(9)	0.51(14)
SS Events	Multijet	3758.64	2423.35
+ dilepton selection	$W(e\nu)$	1.7(3)	0.40(15)
	$W(\mu\nu)$	4.1(4)	3.5(4)
	$W(\tau\nu)$	0.8(4)	0.7(4)
	$\gamma^*/Z(ee)$	0.3(1)	0.08(3)
	$\gamma^*/Z(\mu\mu)$	0.28(4)	0.26(4)
	$t\bar{t}$	4.57(15)	3.15(12)
	Diboson	0.11(1)	0.05(1)

Table 7.2: The number of data and MC events (for the significant backgrounds) for the four regions of the multijet background estimation after the dilepton selection [56] in the $\tau_e\tau_\mu$ final state.

Isolation requirement	μ_1 isolated	μ_1 non-isolated	k
$\epsilon(\mu_2) I^{0.4}_{E_{\mathrm{T}}} < 0.20$	0.38(3)	0.110(4)	3.4(3)
$\epsilon(\mu_2) I^{0.4}_{p_{\mathrm{T}}} < 0.20$	0.37(3)	0.110(4)	3.5(3)
Isolation requirement	μ_2 isolated	μ_2 non-isolated	k
$\epsilon(\mu_1) I^{0.4}_{E_{\mathrm{T}}} < 0.20$	0.53(4)	0.180(6)	2.9(2)
$\epsilon(\mu_1) I^{0.4}_{p_{\mathrm{T}}} < 0.20$	0.44(4)	0.136(4)	3.2(3)

Table 7.3: The efficiency that one muon passes the given isolation requirement when the other muon is either isolated and when it is not isolated. The ratio of efficiencies, the k value, is presented in the last column.

where k is a factor that corrects for any observed correlations between the isolation of the two selected muons.

Four k factors were computed by measuring the ratio of the efficiency of the leading (sub-leading) muon to pass either calorimeter ($I^{0.4}_{E_{\mathrm{T}}} < 0.20$) or tracking ($I^{0.4}_{p_{\mathrm{T}}} < 0.15$) isolation when the sub-leading (leading) muon was isolated verse anti-isolated. The final k value was taken as the simple average of the four measured k values:

$$k = 3.26 \pm 0.55 \text{ (stat.)}. \tag{7.13}$$

The individual k measurements can be found in Table 7.3.

The number of multijet events measured in data before the BDT requirement was, using eqn. 7.12:

$$N^A_{MJ} = 69 \pm 12 \text{ (stat.)} \pm 11 \text{ (sys.)}, \tag{7.14}$$

while the final number of multijet events, after the entire event selection, was obtained by multiplying N^A_{MJ} by the efficiency for events in region C to pass the BDT selection. The final multijet contribution after the entire event selection was measured as:

$$N^A_{MJ} = 10.1 \pm 2.5 \text{ (stat.)} \pm 1.6 \text{ (sys.)}. \tag{7.15}$$

The systematic uncertainties on the final event yields were evaluated by varying the measured k values within their uncertainties (Section 9.4).

		μ_1 isolated	μ_1 non-isolated
		region A	region C
	data	2491(50)	366(19)
	$Z \to \tau\tau$	115.1(1.4)	3.2(2)
μ_2 isolated	Multijet	69(12)	305(18)
+ Visible Mass Selection	$W \to e\nu$	0.0	0.0
	$W \to \mu\nu$	1.5(3)	4.0(4)
	$W \to \tau\nu$	0.0	0.2(2)
	$\gamma* /Z \to \mu\mu$	2140(10)	49(1.7)
	$\gamma* /Z \to ee$	0.0	0.0
	$t\bar{t}$	12.4(4)	4.9(3)
		region B	region D
	data	766(28)	6550(81)
	$Z \to \tau\tau$	9.2(4)	0.4(1)
μ_2 non-isolated	Multijet	460(20)	6530(80)
+ Visible Mass Selection	$W \to e\nu$	0.0	0.0
	$W \to \mu\nu$	43.9(1.5)	2.3(4)
	$W \to \tau\nu$	2.7(7)	1.2(5)
	$\gamma^*/Z \to ee$	0.0	0.2(1)
	$\gamma^*/Z \to \mu\mu$	231(3)	9.5(8)
	$t\bar{t}$	22.7(6)	4.3(2)

Table 7.4: The number of events in each region for the multijet estimation method before the BDT requirement in the $\tau_\mu\tau_\mu$ final state.

Chapter 8

CROSS-SECTION MEASUREMENT

The $Z \rightarrow \tau\tau$ production cross-section for each final state was measured within the fiducial volume of the ATLAS detector using:

$$\sigma_{\text{fid}} = \frac{N - N_{\text{bkgrd}}}{C_Z \mathcal{L}} \tag{8.1}$$

where σ represents the cross-section, C_Z represents the detector acceptance, and $\mathcal{L}$ the total integrated luminosity. The total cross-section was then measured, after extrapolating to the entire phase space, using[1]:

$$\sigma_{\text{tot}} = \frac{N - N_{\text{bkgrd}}}{C_Z A_Z \mathcal{L} B} \tag{8.2}$$

where A_Z is the measured extrapolation factor that represents the geometrical and kinematic acceptance and B is the branching ratio for $Z \rightarrow \tau\tau \rightarrow \tau_x\tau_y$. The combined total cross-section is then derived using the Best Linear Unbiased Estimate (BLUE) Method [57, 58] to combine the individual cross-section measurements, taking correlations into account, in a manner that minimizes the combined uncertainty.

Section 8.1 discusses the geometric and kinematic correction factor, followed by Section 8.2 which discusses the detector efficiency, and finally Section 8.3 discusses the combination procedure.

8.1 Geometrical Acceptance

The geometric and kinematic acceptance factor, A_Z, was defined as the ratio:

$$A_Z = \frac{N_{\text{dressed}}^{\text{gen kin}}}{N_{\text{Born}}^{\text{gen m}_{\text{inv}}}} \tag{8.3}$$

[1]This is not quite true. There is still a phase space cut on the true invariant mass of the ditau pair: $66 < m_{\tau\tau} < 116$ GeV

where $N_{\text{Born}}^{\text{gen m}_{\text{inv}}}$ was the number of events at Born[2] level whose $\tau\tau$ invariant mass fell within the window [66,116] GeV and $N_{\text{dressed}}^{\text{gen kin}}$ is the number of events at generator level that fell within the fiducial regions described in Table 8.1. The generator level tau lepton decay products in the $N_{\text{dressed}}^{\text{gen kin}}$ term were further "dressed" by combining their 4-vectors with any photons radiated, either from the original tau or from its subsequent decay products, in order to correct for any final state radiation. Since there was no invariant mass requirement on the $N_{\text{dressed}}^{\text{gen kin}}$ term, events that passed the fiducial cuts, but not the invariant mass cut at Born level, were accounted for. The nominal A_Z values were computed using the default `PYTHIA` MC sample generated with the modified LO parton distribution function (PDF) MRSTLO [36] and the ATLAS Monte Carlo tune [38] (Section 4.2). The central values for A_Z, along with their total uncertainties are reported in Table 8.2. A discussion on the systematic uncertainty is given in Section 9.8.

8.2 Detector Acceptance

The detector acceptance factor, C_Z, takes into account the full trigger, reconstruction, and identification efficiencies within the fiducial volume of the ATLAS detector. C_Z was defined as:

$$C_Z = \frac{N^{\text{reco pass}}}{N_{\text{dressed}}^{\text{gen kin}}} \tag{8.4}$$

where $N^{\text{reco pass}}$ represents the number of events that pass the full offline selection, including all correction factors, as described in Chapters 6 and 9. Since the $N^{\text{reco pass}}$ term did not have a requirement on the generator level fiducial cuts, events that migrated from the defined fiducial regions at generator level, were accounted for. Table 8.2 presents the final C_Z measurements along with their total uncertainty. The total uncertainty is a quadratic sum of each individual source discussed in Chapter 9 together with the MC statistical uncertainties, of approximately 1%, in each channel.

---

[2]Born level refers to the state of the lepton before any final state radiation.

Final State	Fiducial Region	
$\tau_h\tau_\ell$	Electron:	$p_{\mathrm{T}} > 16$ GeV, $\lvert\eta\rvert < 2.47$
		Excluding $1.37 < \lvert\eta\rvert < 1.52$
	Muon:	$p_{\mathrm{T}} > 15$ GeV, $\lvert\eta\rvert < 2.4$
	Tau:	$p_{\mathrm{T}} > 20$ GeV, $\lvert\eta\rvert < 2.47$
		Excluding $1.37 < \lvert\eta\rvert < 1.52$
	Event:	$\Sigma\cos\Delta(\phi) > -0.15, m_{\mathrm{T}} < 50$ GeV
		$35 < m_{\mathrm{vis}} < 75$ GeV
$\tau_e\tau_\mu$	Electron:	$p_{\mathrm{T}} > 16$ GeV, $\lvert\eta\rvert < 2.47$
		Excluding $1.37 < \lvert\eta\rvert < 1.52$
	Muon:	$p_{\mathrm{T}} > 10$ GeV, $\lvert\eta\rvert < 2.4$
	Event:	$\Sigma\cos\Delta(\phi) > -0.15$
		$25 < m_{\mathrm{vis}} < 80$ GeV
$\tau_\mu\tau_\mu$	Leading Muon:	$p_{\mathrm{T}} > 15$ GeV, $\lvert\eta\rvert < 2.4$
	Sub-Leading Muon:	$p_{\mathrm{T}} > 10$ GeV, $\lvert\eta\rvert < 2.4$
	Event:	$25 < m_{\mathrm{vis}} < 65$ GeV

Table 8.1: The definition of the fiducial regions used for the cross-section measurements in each $\tau\tau$ final state.

	$\tau_e\tau_h$	$\tau_\mu\tau_h$	$\tau_e\tau_\mu$	$\tau_\mu\tau_\mu$
N_{obs}	151	213	85	90
$N_{\text{obs}} - N_{\text{bkgrd}}$	$114 \pm 14 \pm 3$	$164 \pm 16 \pm 4$	$76 \pm 10 \pm 1$	$43 \pm 10 \pm 3$
A_Z	0.101 ± 0.003	0.117 ± 0.004	0.114 ± 0.003	0.156 ± 0.006
C_Z	0.12 ± 0.02	0.20 ± 0.03	0.29 ± 0.02	0.27 ± 0.02
B	0.2313 ± 0.0009	0.2250 ± 0.0009	0.0620 ± 0.0002	0.0301 ± 0.0001
$\mathcal{L}$	35.7 ± 1.2 pb^{-1}	35.5 ± 1.2 pb^{-1}	35.5 ± 1.2 pb^{-1}	35.5 ± 1.2 pb^{-1}

Table 8.2: The components of the $Z \to \tau\tau$ cross-section calculations for each final state. For $N_{\text{obs}} - N_{\text{bkgrd}}$ the first uncertainty is statistical and the second systematic. For all other values, the total uncertainty is given. The systematic uncertainty for all C_Z values was obtained by adding each of the individual sources in quadrature.

8.3 Cross-Section Measurement and Combination

By inputting the results from Table 8.2 into equations 8.1 and 8.2, the total and fiducial cross-sections were computed, respectively. The measured fiducial and total cross-sections for each final state are presented in Table 8.3. The total systematic uncertainties were determined by adding, in quadrature, the effect of each individual systematic uncertainty on the final measured cross-section, as described in Chapter 9, rather than using the total systematic uncertainties on C_Z and $N - N_{\text{bkgrd}}$ directly.

In the absence of any correlations between n measurements of the cross-section ($\sigma_{\text{x.s.}}$), a combined cross-section can be computed by weighting each individual measurement by its variance (uncertainty squared σ^2):

$$\sigma_{\text{x.s.}} = \frac{1}{\sigma^2}\Sigma_i\left(\frac{\sigma_{\text{x.s.},i}}{\sigma_i^2}\right) \tag{8.5}$$

where $\sigma_{\text{x.s.},i}$ are the individual cross-section measurement, σ_i the respective uncertainties, and σ^2 is the total uncertainty ($1/\sigma^2 = \Sigma(1/\sigma_i^2)$).

Fiducial Cross-Section	
	$\sigma \pm \Delta(stat.) \pm \Delta(sys.) \pm \Delta(lumi)[nb]$
$\tau_h\tau_e$	$27 \pm 3 \pm 5 \pm 1$
$\tau_h\tau_\mu$	$23 \pm 2 \pm 3 \pm 1$
$\tau_e\tau_\mu$	$7.5 \pm 1.0 \pm 0.5 \pm 0.3$
$\tau_\mu\tau_\mu$	$4.5 \pm 1.1 \pm 0.6 \pm 0.2$
Total Cross-Section	
$\tau_h\tau_e$	$1.14 \pm 0.14 \pm 0.20 \pm 0.04$
$\tau_h\tau_\mu$	$0.86 \pm 0.08 \pm 0.12 \pm 0.03$
$\tau_e\tau_\mu$	$1.06 \pm 0.14 \pm 0.08 \pm 0.04$
$\tau_\mu\tau_\mu$	$0.96 \pm 0.22 \pm 0.12 \pm 0.03$
Total Combined Cross-Section	
Combined	$0.97 \pm 0.07 \pm 0.06 \pm 0.03$

Table 8.3: The fiducial and individual cross-sections, including all uncertainties, for all four final states. The combined total cross-section is found using the Best Linear Unbiased Estimate (BLUE) method.

8.3.1 BLUE Method

Since each measurement used the same data-set, the same detector, and the same reconstruction and identification techniques, we cannot assume that uncertainties on each final state are uncorrelated. The BLUE method assumes that an experiment has n unbiased measurements y_i, and a corresponding symmetric $n \times n$ error (uncertainty) matrix where the diagonal elements represent the variance for each measurement y_i, while the off-diagonal elements represent the correlations between pairs of measurements. The BLUE method [57, 58] attempts to find the best estimate y which:

- is a linear combination of each of the individual estimates
- is unbiased
- provides the smallest possible variance (error/uncertainty) for the estimate y

From the first condition we can write the best estimate y as:

$$y = \Sigma \alpha_i * y_i \tag{8.6}$$

whereby the second condition, the weighting factors, α_i, must satisfy $1 = \Sigma \alpha_i$. From equation 8.6, we can compute the combined variance as:[3]

$$\sigma^2 = \vec{\alpha}^{\mathrm{T}} E \vec{\alpha} \tag{8.7}$$

where $\vec{\alpha}$ is a vector of the weighting factors, $\vec{\alpha}^{\mathrm{T}}$ is its transpose, and E is the matrix. The computation of the error matrix is described further in Section 8.3.2. Thus, by minimizing the variance (equation 8.7), we can solve for $\vec{\alpha}$. Lagrangian multipliers can be used to find the $\vec{\alpha}$ that minimizes the variance:

$$\begin{aligned} \boldsymbol{\nabla}(\vec{\alpha}^{\mathrm{T}} E \vec{\alpha}) &= \lambda \boldsymbol{\nabla}(\Sigma \alpha_i - 1) \\ \Sigma \alpha_i &= 1. \end{aligned} \tag{8.8}$$

[3]Note that if we ignore correlations, E is a diagonal matrix whose elements are the variance for each measurement, then the vector, $\vec{\alpha}$, would have elements of $1/\sigma_i^2$ leading to the naive uncertainty estimate of $\sigma^2 = \frac{1}{\Sigma 1/\sigma_i^2}$.

Since the error matrix, E, is symmetric by construction ($\mathrm{cov}(i,j) = \mathrm{cov}(j,i)$), and by introducing a vector $\vec{u}$ whose elements are all unity, equations 8.8 can be rewritten as:

$$\begin{aligned} \nabla_{\alpha_i}(\vec{\alpha}^{\mathrm{T}} E \vec{\alpha}) &= (E + E^T)\vec{\alpha} \\ &= 2E\vec{\alpha} = \lambda\vec{u} \\ \Sigma\alpha_i &= \vec{u}^{\mathrm{T}}\vec{\alpha} = 1. \end{aligned} \tag{8.9}$$

Solving for the $\vec{\alpha}$ vector:

$$\vec{\alpha} = \frac{\lambda E^{-1}\vec{u}}{2} \tag{8.10}$$

and multiplying both sides of equation 8.10 by the constraint $\vec{u}^{\mathrm{T}}\vec{\alpha} = 1$ to solve for λ:

$$\lambda = \frac{2}{\vec{u}^{\mathrm{T}} E^{-1}\vec{u}} \tag{8.11}$$

and finally substituting λ back into equation 8.10, the weights that minimize the error can be found as:

$$\vec{\alpha} = \frac{E^{-1}\vec{u}}{\vec{u}^{\mathrm{T}} E^{-1}\vec{u}}. \tag{8.12}$$

8.3.2 Computation of Error Matrix

In order to utilize equation 8.12, the error matrix, E, must be constructed. The total error matrix is simply the sum of the error matrices from each individual uncertainty:

$$E = E(\mathrm{stat.}) + \Sigma_i E_{i,(\mathrm{sys.})} + E(\mathcal{L}) \tag{8.13}$$

where the systematic contribution is itself a sum. The diagonal elements represent the variance for a specific uncertainty on a specific final state defined as:

$$\sigma^2 = ((\sigma^-_{\mathrm{x.s.}} - \sigma^+_{\mathrm{x.s.}})/2)^2 \tag{8.14}$$

where the $+/-$ refers to the resultant cross-section when a source of uncertainty is scaled up or down respectively. The off-diagonal elements, on the other hand, represent any correlation that a specific uncertainty has between a pair of final states:

$$\mathrm{cov(i,j)} = \frac{1}{4}(\sigma^-_{\mathrm{x.s.},i} - \sigma^+_{\mathrm{x.s.},i})(\sigma^-_{\mathrm{x.s.},j} - \sigma^+_{\mathrm{x.s.},j})R \tag{8.15}$$

where R represents the correlation factor between the two final states. We can then, for example, construct the error covariance matrix for the systematic uncertainty on the energy scale by looking at Table 9.8 and filling in the corresponding numbers. Table 8.5 (left) depicts this example error matrix.

The correlation factors, for each systematic uncertainty were set to either 1 for fully correlated, or 0 for fully uncorrelated. Since the event selections were mutually exclusive, the statistical error is naturally uncorrelated between channels. The uncertainties on the geometrical acceptance factor, luminosity, the pileup description, and the theoretical cross-sections were considered fully correlated between all channels since any sources of uncertainties in these measurements were common among all the final states. The multijet estimate method is considered fully correlated between the $\tau_h\tau_e$, $\tau_h\tau_\mu$, and $\tau_e\tau_\mu$ final states, but uncorrelated with the $\tau_\mu\tau_\mu$ final state since different methods were used between the two sets of final states. The other partially correlated uncertainties arise when a particular final state had no expected uncertainty due to a specific systematic (i.e. hadronic tau identification efficiency on the $\tau_e\tau_\mu$ final state). Table 8.4 summarizes whether a systematic uncertainty was considered correlated between a pair of final states.

Table 8.5 (right) shows the complete error matrix after considering each source of uncertainty and taking all possible correlations into account. Inserting the full covariance matrix into equation 8.12 gave us the final weighting factors, α (Table 8.6). We then found the combined cross-section by substituting the final state weights into equation 8.6, and the statistical, systematic, and luminosity uncertainties were found by plugging the corresponding error matrices into equation 8.7. The total combined cross-section was determined to be:

$$\sigma = 0.97 \pm 0.07 \text{ (stat.)} \pm 0.06 \text{ (sys.)} \pm 0.03 \text{ (lumi.) nb.} \tag{8.16}$$

which is in agreement with the Next to Next to Leading Order (NNLO) Standard Model prediction of:

$$\sigma(\text{NNLO}) = 0.96 \pm 0.05 \text{ nb,} \tag{8.17}$$

for $\gamma^*/Z \rightarrow \tau\tau$ decays within the invariant mass window of $[66, 116]$ GeV. The combined ATLAS $\gamma^*/Z \rightarrow \tau\tau$ cross-section measurement is compared with the ATLAS combined

Systematic	$\tau_h\tau_e/\tau_h\tau_\mu$	$\tau_h\tau_e/\tau_e\tau_\mu$	$\tau_h\tau_e/\tau_\mu\tau_\mu$	$\tau_h\tau_\mu/\tau_e\tau_\mu$	$\tau_h\tau_\mu/\tau_\mu\tau_\mu$	$\tau_e\tau_\mu/\tau_\mu\tau_\mu$
Muon efficiency	0%	0%	0%	100%	100%	100%
Muon D0	0%	0%	0%	0%	0%	0%
Muon resolution & energy scale	0%	100%	0%	100%	100%	100%
Electron efficiency, resolution	0%	100%	0%	0%	0%	0%
τ_h identification efficiency	100%	0%	0%	0%	0%	0%
τ_h misidentification	100%	0%	0%	0%	0%	0%
e charge misidentification	0%	100%	0%	0%	0%	0%
Energy scale (e/τ/jets/$E_{\mathrm{T}}^{\mathrm{miss}}$)	100%	100%	100%	100%	100%	100%
Multijet Estimate method	100%	100%	0%	100%	0%	0%
W normalization factor	0%	0%	0%	0%	0%	0%
Object Quality Cuts	100%	100%	100%	100%	100%	100%
Pileup description in simulation	100%	100%	100%	100%	100%	100%
Theoret. cross-section	100%	100%	100%	100%	100%	100%
A_Z systematics	100%	100%	100%	100%	100%	100%

Table 8.4: Correlations of systematic uncertainties between the four individual channels.

$[\mathrm{pb}]^2$	$\tau_h\tau_e$	$\tau_h\tau_\mu$	$\tau_e\tau_\mu$	$\tau_\mu\tau_\mu$		$\tau_h\tau_e$	$\tau_h\tau_\mu$	$\tau_e\tau_\mu$	$\tau_\mu\tau_\mu$
$\tau_h\tau_e$	15000	11000	-2300	0		60000	21000	-7100	2600
$\tau_h\tau_\mu$	11000	8000	-1600	0		21000	23000	-710	-770
$\tau_e\tau_\mu$	-2300	-1600	330	0		-7100	-710	28000	4300
$\tau_\mu\tau_\mu$	0	0	0	0		2600	-770	4300	65000

Table 8.5: An example error matrix for the effect of the electron, tau, jet, and $E_{\mathrm{T}}^{\mathrm{miss}}$ energy scale on the cross-section measurement (left) along with the total error matrix (right). The uncertainty on the muon momentum scale is expected to be independent on the uncertainty of the electron, tau, jet, and $E_{\mathrm{T}}^{\mathrm{miss}}$ Energy scale.

$\gamma^*/Z \to ee/\mu\mu$ cross-section measurement and each of the individual final state measurements in Figure 8.1. The NNLO theoretical prediction ($66 < m_{\text{inv}} < 116$ GeV) along with its uncertainty is also displayed. Good agreement, within one standard deviation can be seen amongst all the individual channels. Table 9.8 in Chapter 9 includes the effect that each systematic uncertainty had on the combined cross-section measurement.

	$\tau_h\tau_e$	$\tau_h\tau_\mu$	$\tau_e\tau_\mu$	$\tau_\mu\tau_\mu$
σ (nb)	1.14	0.86	1.06	0.96
Total unc. (nb)	0.24	0.15	0.17	0.25
Weight	0.079	0.394	0.390	0.137
Pull	-0.76	1.02	-0.68	0.06

Table 8.6: The individual final state cross-section measurements along with their total uncertainty, weight in the combination, and pull. The pull is defined as the ratio of the difference between the combined result and the individual result to the error on this difference.

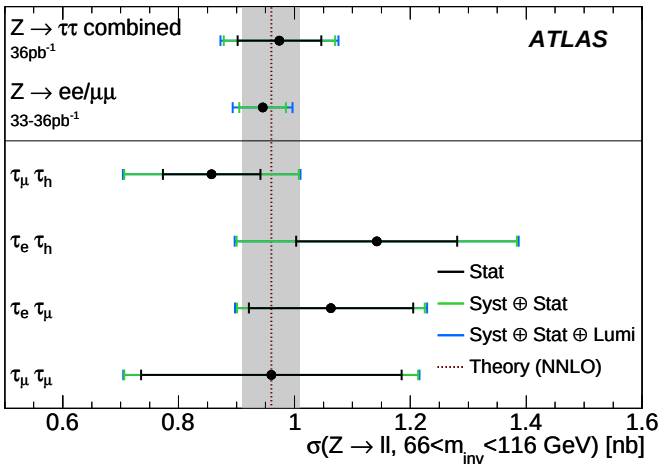

Figure 8.1: The ATLAS combined $Z \rightarrow \tau\tau$ cross-section measurement compared with the ATLAS combined $Z \rightarrow ee$ and $Z \rightarrow \mu\mu$ cross-sections. The vertical dashed line represents the theoretical prediction and the shaded band its uncertainty. The individual $Z \rightarrow \tau\tau$ final states are also shown. Uncertainties for each cross-section measurement include statistical, statistical and systematic, and the total uncertainty.

Chapter 9

SYSTEMATIC UNCERTAINTIES

For each systematic uncertainty considered in this analysis, the full background extraction method discussed in Section 7 was performed, including fluctuating the MC background and signal contributions in the three background regions (B,C, and D) within $\pm 1\sigma$ of the estimated uncertainty. A new cross-section ($\sigma_{\text{x.s.}}$) was then measured, for each systematic uncertainty, by simultaneously fluctuating the correlated detector acceptance factor (C_Z) within in one standard deviation (σ):

$$\sigma^{\pm}_{\text{x.s.}} = \frac{(N - N_{\text{bkgrd}})^{\pm}}{C^{\pm}_{Z}\mathcal{L}}. \tag{9.1}$$

The quoted systematic uncertainty of the cross-section, from each source of uncertainty, was calculated as $\frac{1}{2}(\sigma^{+}_{\text{x.s.}} - \sigma^{-}_{\text{x.s.}})$. The total systematic uncertainty on the measured cross-section, for each final state, was the quadratic sum of the individual uncertainties on each cross-section measurement.

9.1 Pileup Reweighting

Due to the high instantaneous luminosities achieved at the LHC, there are events where multiple hard interactions occur. Such events are referred to as pileup events. The degree of pileup, or the number of hard interactions in the event, can be quantified by measuring the number of reconstructed vertices in an event. On average, there were about 1.6 interactions per event in the 2010 data set. An example of the effect of pileup is shown in Figure 9.1, where the R_{EM}, a variable used in tau identification (Section 5.5.2), and the muon calorimeter isolation variable, $I^{0.4}_{E_{\text{T}}}$, are shown in events with one vertex, two vertices, or 3 or more vertices. In general, events with more pileup exhibit wider distributions in both variables due to extra calorimeter deposits from the pileup events.

In order to simulate the pileup conditions at the LHC, minimum-bias events were overlaid with the event of interest in all default MC samples. For the MC samples used in this

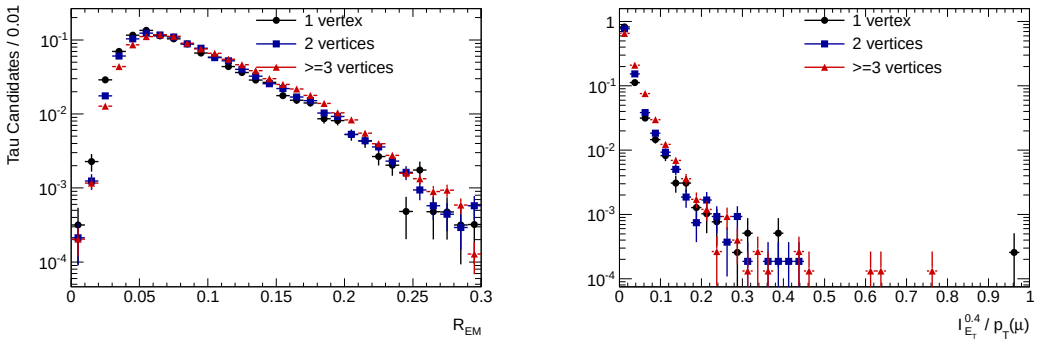

(a) $\tau_h\tau_\mu$ (b) $\tau_h\tau_\mu$

Figure 9.1: The R_{EM} for true hadronic taus from MC (left), and $I^{0.4}_{E_{\mathrm{T}}}$ isolation for real muons from data (right) distributions are plotted in events with one, two, or three or more associated vertices. On average, the distributions become wider with more pileup activity.

analysis, an average of two[1] extra minimum-bias events were overlaid on each hard scattering parton-parton event (Figure 9.2(a)). MC events were further reweighted, based on the number of reconstructed vertices, to match the distributions in data. Separate weights were computed for both data triggered by muons ($\tau_h\tau_\mu$ and $\tau_\mu\tau_\mu$ final states) and data triggered by electrons ($\tau_h\tau_e$ and $\tau_e\tau_\mu$ final states). Similar weights were observed. Thus, in order to use the same weights for all four final states, the two sets of weights were averaged. This averaging procedure produced small discrepancies at high number of vertices (Figure 9.2(b)).

A systematic uncertainty on the reweighting procedure was estimated by rerunning all signal and background MC samples shifting the pileup reweighting factors up and down by one standard deviation. Small shifts of 0.35, 0.35, 0.6, and $< 0.1\%$, were observed in the $\tau_h\tau_e$, $\tau_h\tau_\mu$, $\tau_e\tau_\mu$, and $\tau_\mu\tau_\mu$final states, respectively.

9.2 Physics Object Efficiency

There are four components of the physics object[2] efficiency that could potentially suffer from systematic uncertainty: the trigger efficiency (ϵ_{trig}), reconstruction efficiency (ϵ_{reco}),

[1]The number of overlaid minimum-bias events was determined by a poissonian distribution with a mean of two.

[2]In this analysis, electrons, muons, taus, and jets are considered physics objects.

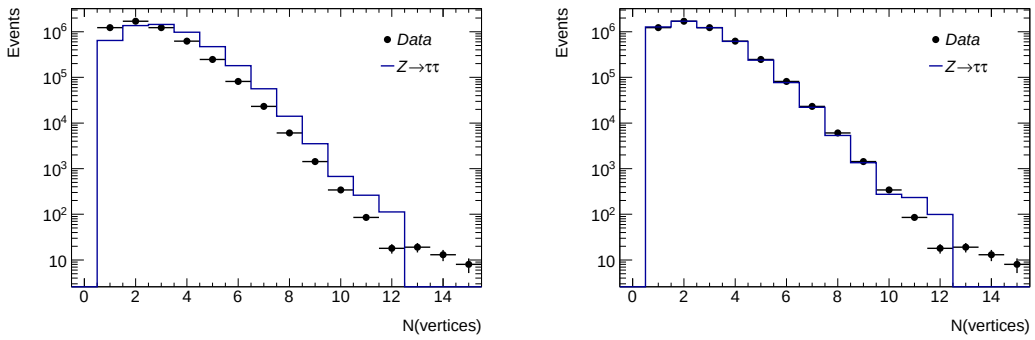

(a) $\tau_e\tau_\mu$ (b) $\tau_e\tau_\mu$

Figure 9.2: The number of vertices before pileup reweighting (left) and after pileup reweighting (right) for data (markers) and MC (lines) are shown. After reweighting, the number of reconstructed vertices in data and MC match. The small differences at high number of vertices are due to the small differences in the overall data distributions for electron triggered data and muon triggered data.

identification efficiency (ϵ_{id}), and the isolation efficiency (ϵ_{isol}). Since single lepton (e/μ) triggers were used in all four final states and no isolation was applied to the tau candidates, only reconstruction and identification efficiency uncertainties were applied to hadronic tau candidates, while electrons and muons were subject to all four sources of uncertainty.

In order to account for differences in object efficiencies between data and MC, scale factors were applied to the MC events in order to ensure that the MC efficiency matched the data efficiency.

$$\epsilon_{\text{s.f.}} = \frac{\epsilon_{\text{data}}}{\epsilon_{\text{MC}}}. \tag{9.2}$$

The efficiency in data (ϵ_{data}) was measured by tagging an object (a lepton or $E_{\text{T}}^{\text{miss}}$) and then probing for an unbiased lepton. The following subsections describe in more detail the different tag probe analyses used to determine the lepton efficiency in both data and MC. The efficiency in data was defined as:

$$\epsilon_{\text{probe}} = \frac{N \text{ probes pass requirement}}{N \text{ probes}}. \tag{9.3}$$

The systematic uncertainty on the object efficiency provides the uncertainty on the derived scale factor. This systematic uncertainty was often dominated by uncertainties in the

background subtraction method and the probe statistics (in data).

The final systematic for the object efficiency was measured by rerunning the entire analysis on all MC signal and background samples with the scale factors shifted up and down by one standard deviation.

9.2.1 Electron Efficiency

Three complementary tag and probe data samples were used to determine the electron reconstruction (ϵ_{reco}), identification (ϵ_{id}), and trigger (ϵ_{trig}) efficiencies: a $Z \to ee$ sample, a $W \to e\nu$ sample, and a J/ψ sample [48]. Due to the 16 GeV p_{T} thresholds imposed on the selected electrons, only the results from the W/Z decays were used in this analysis.

The $W \to e\nu$ sample, used to measure the trigger scale factors, used the expected missing transverse energy ($E_{\text{T}}^{\text{miss}}$) from the neutrino as the tag, and the electron as the probe. In order to eliminate any bias from electron triggers, these events were selected with $E_{\text{T}}^{\text{miss}}$ triggers with thresholds ranging from 20 to 40 GeV, depending on the instantaneous luminosity. These events were further refined to have an offline[3] $E_{\text{T}}^{\text{miss}}$ measurement of at least 25 GeV, and a transverse mass (m_{T}) of at least 40 GeV. In order to reduce backgrounds from multijet events, or events with an electron that converts to a pair of photons due to material interactions in the tracker, the $E_{\text{T}}^{\text{miss}}$ direction was required to be isolated from any jet or lepton in the event ($\Delta\phi(E_{\text{T}}^{\text{miss}}, \ell(j)) > 2.5$). The background in this sample was estimated using the electron's relative calorimeter isolation distribution within a ΔR cone of 0.4, $I_{E_{\text{T}}}^{0.4}$. As discussed in Section 6.3, true prompt electrons should have an $I_{E_{\text{T}}}^{0.4}$ value close to zero, while fake electrons (or true electrons from heavy flavor meson decays) tend to have larger isolation values. A background template $I_{E_{\text{T}}}^{0.4}$ distribution was made by reversing some of the identification requirements used in electron identification. This background template distribution was then scaled to match the number of events with $I_{E_{\text{T}}}^{0.4} > 0.4$ in the signal distribution. Assuming that nearly all events where the probe electron has an $I_{E_{\text{T}}}^{0.4} > 0.4$ are background in the signal distribution, the amount of background in events with $I_{E_{\text{T}}}^{0.4} < 0.4$ can be estimated from the background template distribution.

[3]Offline simply means that the quantity was calculated with access to the entire event record after it was written to disk.

The $Z \to ee$ sample, used for measuring the reconstruction and identification scale factors, required a tag electron passing the "Tight" identification with $p_{\mathrm{T}} > 20$ GeV that was matched to a trigger electron object. A second electron was then probed in the event and required to have a $p_{\mathrm{T}} > 15$ GeV and an opposite charge to the tag electron. The typical signal region was further refined to ensure that the invariant mass of the electron pair was within 10 GeV of the Z boson mass ($80 < m_{ee} < 100$ GeV). For the η-dependent scale factors, the background was estimated with a simple same sign event subtraction method[4], while for the p_{T} dependent scale factors, the background was estimated with separate fits on the dielectron invariant mass in each probe p_{T} bin.

The measured trigger efficiency was found to be 99.0% with respect to offline "Tight" electron selection with an uncertainty of 0.5% for electrons with $p_{\mathrm{T}} > 20$ GeV and an uncertainty of 2% for electrons with $p_{\mathrm{T}} < 20$ GeV. The reconstruction efficiency, measured as the efficiency for a reconstructed cluster in the EM calorimeter to be matched to a quality inner detector track (Section 5.3), was measured as 94.3% with an uncertainty, independent of p_{T} and η, of 1.5%. The "Tight" identification efficiency with respect to a reconstructed electron candidate was found to be 80.7% with uncertainties ranging from 17% for low p_{T} electrons to less than 1% for high p_{T} electrons. The large uncertainty for the electron identification efficiency at low p_{T} is primarily due to low statistics in the probe sample. Electrons with $15 < p_{\mathrm{T}}(e) < 20$ GeV were found to have significantly lower efficiencies in data than in MC (62% in data for "Tight" electrons versus 78.3% in MC) [48].

In order to provide a conservative systematic estimate, the trigger, reconstruction, identification, and isolation (Section 9.2.3) scale factors were simultaneously shifted up and down by one standard deviation. The total systematic on signal MC was found to be 9.1(6.1)% in the $\tau_h\tau_e(\tau_e\tau_\mu)$ final states. The identification uncertainty for low p_{T} electrons dominates the 9.1%. The uncertainty on the W/Z background estimates with direct decays to electrons was somewhat lower ($\sim 4\%$), since these electrons have a higher p_{T}.

[4] Assuming that the background has an equal probability of having electron candidates with the same sign as electron candidates with opposite signs, the number of background events in the opposite sign region should equal the number of events that passes full selection in the same sign region.

9.2.2 Muon Efficiency

The muon efficiency scale factors, ϵ_{trig}, ϵ_{reco}, ϵ_{id}, and ϵ_{isol} (Section 9.2.3), were measured using $Z \rightarrow \mu\mu$ tag and probe samples from data [49]. In all cases, a combined muon candidate with $p_{\text{T}} > 20$ GeV and $|\eta| < 2.4$ was required as the tag muon. In addition, the tagged muon was required to pass the tracker isolation of $I_{p_{\text{T}}}^{0.4} < 0.2$, have $|z_0| < 10$ mm, have at least 2 (6) hits in the pixel (SCT) detector, and satisfy the following TRT hit requirements:

$$\begin{cases} \text{Hits + Outliers} > 5 \;\&\; \dfrac{\text{Outliers}}{\text{Hits + Outliers}} < 0.9, & |\eta| < 1.9 \\ \text{if(Hits + Outliers} > 5\text{):} \; \dfrac{\text{Outliers}}{\text{Hits + Outliers}} < 0.9, & |\eta| > 1.9. \end{cases} \tag{9.4}$$

The probe muon was either an inner detector track or a stand alone muon. In either case, the probe muon candidate must have $p_{\text{T}} > 20$ GeV, $|\eta| < 2.5(2.4)$ ID(MS), $|z_0| < 10$ mm, pass the same ID track requirements (if an ID track), pass the same isolation requirement as the tagged muon, be associated with the same vertex ($|\Delta(z_0)| < 3$mm), be separated in azimuthal angle ($|\Delta(\phi)| > 2.0$), have an opposite charge to the tagged muon, and have an invariant mass within 10 GeVof the Z mass when paired with the tagged muon. By choosing the probe to be either a standalone muon or an ID track, both the efficiency of ID track reconstruction and the efficiency to reconstruct a MS track and match it to the ID track could be estimated. The background in both analyses was small: 0.7% when the probe was an ID track, and $< 0.1\%$ when the probe was a MS track.

The ID track reconstruction efficiency (99.1%) matched that found in MC, so no scale factors were necessary. The MS track reconstruction and matching efficiency($92.8 \pm 0.2\%$), however, does deviate from the MC prediction based on the geometrical region that the muon was reconstructed within the MS. The scale factors have a mean of 0.989 ± 0.003. Since the muon scale factors were not dependent on the p_{T}, the overall systematic uncertainty on muon reconstruction and identification efficiency was not dominated by the low p_{T} muon regime, where data statistics were low. Thus, the overall uncertainty on muon efficiency was less than that for electrons.

The trigger scale factors were obtained using a similar tag and probe analysis. Since the trigger efficiency with respect to offline reconstruction was sought, the requirements on

the probe muon were tightened to be a combined muon, while the tag was required to have fired the trigger. Separate scale factors were then produced as a function of η for the three different triggers used in the analysis (Section 6.4.2). No significant dependence on p_{T} was observed. The scale factors were generally within 5% of unity with an uncertainty between 1 and 2.5%.

As was the case for the electron object systematic uncertainty, all scale factors for muon reconstruction, trigger, and isolation were varied simultaneously up and down by one standard deviation. Total systematic uncertainties of 3.6, 2.6, and 4.7% were observed in the $\tau_h\tau_\mu$, $\tau_e\tau_\mu$, and $\tau_\mu\tau_\mu$ final states, respectively.

9.2.3 Lepton Isolation

Due to the high multijet backgrounds, a very tight isolation was required for both electrons and muons in the $\tau_h\tau_e$, $\tau_h\tau_\mu$, and $\tau_e\tau_\mu$ final states. To calculate the efficiency of these selections, tag and probe analyses were once again performed for both electrons and muons in $Z \to \ell\ell$ events, except that the backgrounds were reduced by allowing the probe lepton to pass full identification. Figure 9.3 shows both the measured isolation efficiencies in data and MC along with the computed scale factors. Scale factors for muon isolation were found to be very near to one and mostly dependent on p_{T}, while the scale factors for electron isolation were seen to depend both on p_{T} and η. The total scale factor for electrons was computed by taking the product of the p_{T} and η dependent scale factors divided by the total measured efficiency in data:

$$\mathrm{sf}_e = \frac{\mathrm{sf}(p_{\mathrm{T}})\mathrm{sf}(\eta)}{\epsilon(\mathrm{data})}. \tag{9.5}$$

Systematic uncertainties on the scale factors were derived by slightly changing the selection required on the tag and probe leptons. The overall muon isolation scale factors were within 1% of unity with an uncertainty never exceeding 1.2%, while the overall electron isolation scale factors ranged from 0.9 to 1.0 with a combined error between 1 and 3%.

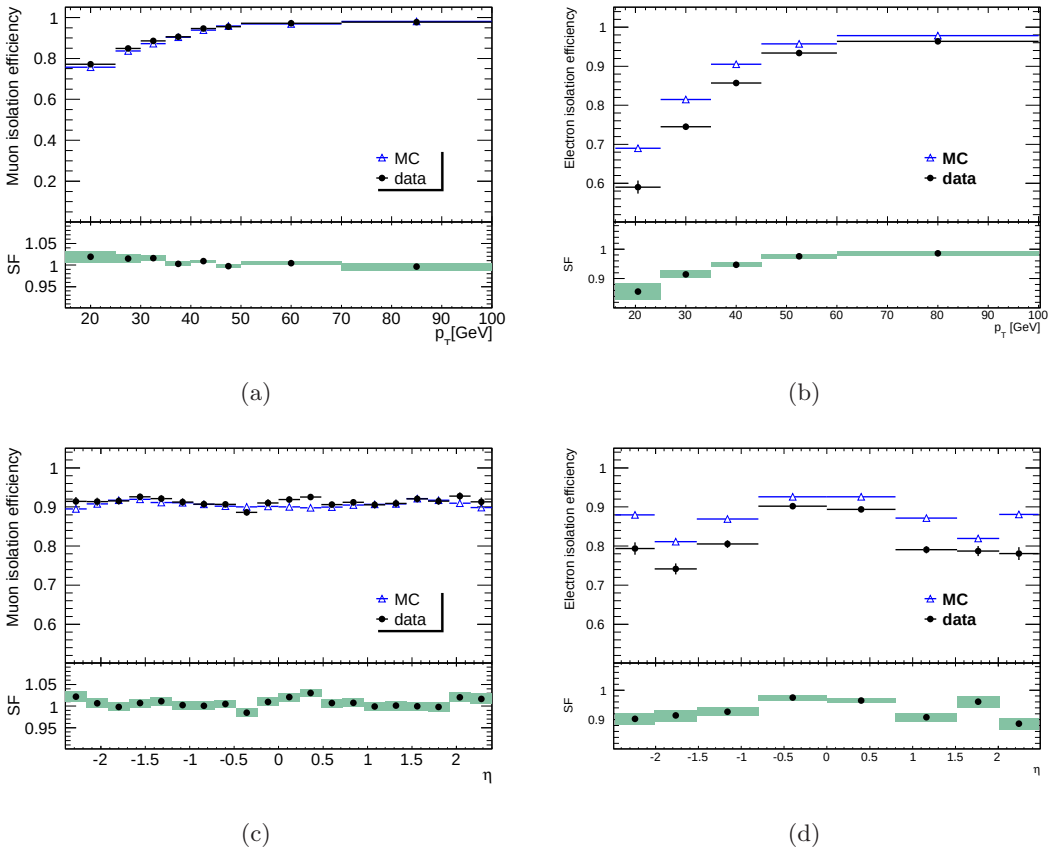

(a) (b)

(c) (d)

Figure 9.3: Isolation efficiency and scale factors measured in data and Monte Carlo. Isolation cut for muons (left): $I_{p_{\mathrm{T}}}^{0.4} < 0.06$ and $I_{E_{\mathrm{T}}}^{0.4} < 0.06$. Isolation cut for electrons (right): $I_{p_{\mathrm{T}}}^{0.4} < 0.06$ and $I_{E_{\mathrm{T}}}^{0.3} < 0.1$

9.2.4 Tau Identification Efficiency

As opposed to electrons and muons, the systematic uncertainty for tau reconstruction and identification was estimated solely with simulation [50] due to the difficulty of obtaining a pure sample of hadronic taus in data. The hadronic tau efficiency and its uncertainty was measured in separate bins of p_{T} ($[15, 30]$, $[30, 40]$, $[40, 100]$ GeV), the true number of stable charged decay products (one or three associated tracks), and whether there were less than three reconstructed vertices or not in the event. A precise definition of the hadronic tau efficiency as a function of p_{T} (or η) can be found in Section 5.5.2. As discussed in Section 9.1, some of the variables used in hadronic tau identification, such as the electromagnetic radius (R_{EM}), were sensitive to multiple interactions. Thus, the uncertainty of hadronic tau identification was also studied with respect to the number of reconstructed vertices. Table 9.1 summarizes the results in each of the bins together with the statistical and systematic uncertainties.

$p_{\mathrm{T}}(\tau)$ [GeV]		[20, 30]	[30, 40]	[40, 100]
$\mathrm{N_{trk}}$	$\mathrm{N_{vxp}}$	ϵ ±stat±sys[%]	ϵ ±stat±sys[%]	ϵ ±stat±sys[%]
1	≤ 2	40.0±0.1±3.5	42.1±0.1±3.7	42.1±0.2±3.9
	≥ 3	31.7±0.1±3.5	34.6±0.1±3.6	35.7±0.1±3.4
3	≤ 2	23.3±0.1±2.9	29.6±0.2±2.6	34.9±0.3±4.2
	≥ 3	18.4±0.1±2.1	24.6±0.1±2.7	30.3±0.2±3.2

Table 9.1: Efficiencies and relative systematic uncertainties for τ lepton identification together with the tight electron veto. The numbers are given with their statistical uncertainties in bins of visible p_{T}, the number of tracks ($\mathrm{N_{trk}}$) of the Monte Carlo truth τ lepton and the number of primary vertices of the event ($\mathrm{N_{vxp}}$).

The systematic uncertainties were determined by varying the event generators and parton distribution functions (Section 4.2), the hadronic shower model (the default `QGSP_BERT` [59, 60, 61] versus `QGSP` and `FTFP_BERT` [62]), the amount of detector material (Section 4.3), jet topological clustering noise thresholds [51], and the EM energy scale (Section 5.2). The individual systematic uncertainties from these sources were added in quadrature to obtain the total systematic uncertainty per bin.

Variations of the underlying event model can influence the calculation of the R_{EM} and, to a lesser extent, the[5] $f_{\mathrm{track}}$by either introducing or removing low p_{T} cells used directly in the computation of the R_{EM} and indirectly in the f_{track}. Different hadronic shower models will also directly influence how the constituent partons in hadronic tau decays are modeled in the calorimeter, and thus influence both the R_{EM} and f_{track} variables. The efficiency was also measured after simulating additional dead material in the detector which can affect the efficiency since the introduction of extra material will affect the uncertainty of the tau's p_{T} and the computation of R_{EM}. Finally, by adjusting the noise threshold on the topological clustering algorithm (Section 5.2) or the EM scale of the calorimeter, the hadronic tau efficiency can be affected mainly by shifts in its reconstructed p_{T} and R_{EM} computation. Figure 5.3 in Section 5.5.2 shows the effect that each systematic variation had on the hadronic tau efficiency.

The hadronic shower model and noise clustering threshold were found to be the dominant systematic for low p_{T} taus, while for high p_{T} taus, only the noise clustering threshold was found to be significant. On average, the systematic uncertainty on hadronic tau identification is found to be about 10% relative to the measured efficiency. In order to find the effect of hadronic tau identification on our event selection, the events are split into bins based on the selected tau's p_{T}, number of tracks, and the number of reconstructed vertices, analogous to Table 9.1. The systematic uncertainties from each bin are then added, weighted by the number of signal sample events that fall in that particular bin. A total systematic uncertainty of 9% was found for $Z \rightarrow \tau\tau$ events.

9.2.5 Tau Fake Rate Systematic Uncertainties

Jets[6] have a relatively high probability to be mis-identified as hadronic taus, especially single isolated charged pions. As was discussed in Section 7.1.1 and [63], having a precise measurement of the hadronic tau mis-identification systematic uncertainty is difficult to

---

[5]The fraction of total momentum belonging the highest p_{T} track of the tau candidate (Section 5.5.2).

[6]Quarks can radiate a gluon which can in turn radiate two gluons, or a quark-antiquark pair. After the quarks and gluons can no longer radiate, the bare quarks hadronize into stable particles. A reconstructed jet is a collection of these stable particles in a conical shape (Section 5.2).

obtain due to the unknown mixture of gluon and quark initiated jets in a given analysis performed on a data sample. This effect was not an issue for the $W \to \ell(e/\mu/\tau)\nu$ samples since the MC was normalized to data. However, for $Z \to \ell\nu$ and $t\bar{t}$ samples, constructing a pure control region is difficult. Additionally, while it is fairly certain that jets are mis-identified as hadronic taus in $W \to \ell\nu$ decays, a second electron (muon) may be mis-identified as a hadronic tau rather than an associated jet in $Z \to \ell\ell$ or $t\bar{t}$ decays. According to simulation, in $Z \to ee$ events, approximately 55% of events passing the full event selection were events where an associated jet passes tau identification, while events in which electrons were reconstructed and identified as hadronic taus make up the remaining 45%.

In order to estimate the mis-identification rate of jets (electrons) in $Z \to \ell\ell$ and $t\bar{t}$ decays, tag and probe analyses were performed in data to select either a pair of leptons (electrons or muons) and a probe jet, or a tight electron and a probe electron that passes tight tau identification. The tag and probe analyses were performed in a similar manner to those discussed in Section 9.2.1. The tau/jet mis-identification rate was then defined as the number of probe jets that pass tight tau identification divided by the number probes. Similarly, the tau/electron mis-identification rate was defined as the number of probe electrons that pass "Tight" tau identification and the electron veto divided by the number of probe electrons that pass "Tight" tau identification. Due to a low number of statistics in both tag and probe analyses, p_{T} dependent scale factors were not used; rather an overall systematic was applied. For MC samples where no real electrons were expected, an overall systematic of 24%, the difference in the overall scale factor from unity combined with its uncertainty in quadrature, was applied. For the $Z \to ee$ and $t\bar{t}$ backgrounds, the overall tau mis-identification uncertainty was the weighted sum of 24% on events where the hadronic tau candidate was truly a jet and 20% on events where the hadronic tau candidate was truly an electron. The overall tau-electron mis-identification uncertainty was estimated by applying η dependent scale factors to events in MC where the reconstructed and identified tau candidate was matched to a true electron.

The uncertainty of the $W \to \ell\nu$ background normalization was obtained by fluctuating the MC within the statistical uncertainty of the measured k_w normalization factors (Section 7.1.1). The statistical uncertainty of the k_w factors ranged from 7 to 15%.

9.3 Energy Scale

The uncertainties due to the energy scale of electrons, muons, hadronic taus, jets, and the $E_{\mathrm{T}}^{\mathrm{miss}}$ were all considered. The details of each are explained in the following sections. However, the effect of the energy scale uncertainty was dependent on the ditau final state:

- $\tau_h\tau_e$**:**
  The uncertainties on the energy scale for electrons, taus, and the $E_{\mathrm{T}}^{\mathrm{miss}}$ were treated as correlated.

- $\tau_h\tau_\mu$**:**
  The uncertainties on the energy scale for taus and $E_{\mathrm{T}}^{\mathrm{miss}}$ were treated as correlated, while the small uncertainty on the muon momentum scale is considered as uncorrelated.

- $\tau_e\tau_\mu$**:**
  The uncertainties on the energy scale for electrons, jets, and $E_{\mathrm{T}}^{\mathrm{miss}}$ were treated as correlated, while the muon momentum scale was considered as uncorrelated.

- $\tau_\mu\tau_\mu$**:**
  The muon momentum scale and $E_{\mathrm{T}}^{\mathrm{miss}}$ were considered.

The final systematic was measured by simultaneously varying each correlated systematic either up or down. Any smearing or scale variation of the muon's momentum was propagated to the final $E_{\mathrm{T}}^{\mathrm{miss}}$ (Section 9.3.5). Since the $E_{\mathrm{T}}^{\mathrm{miss}}$ was reconstructed from all topological clusters rather than from final identified and calibrated physics objects (Section 5.6), any smearing or scale variations to jets, hadronic tau candidates, and electrons was not propagated to the final $E_{\mathrm{T}}^{\mathrm{miss}}$.

9.3.1 Tau Energy Scale

In addition to the systematic uncertainties discussed for hadronic tau efficiency (Section 9.2.4), the systematic on closure is considered. The derived continuous response function (Section

5.5.1) should predict the generator level p_{T} of the true hadronic tau:

$$R_{\tau}^{\mathrm{EM}} = 1 + \frac{a_1}{\ln(p_{\mathrm{T}}^{\mathrm{EM}})} + \frac{a_2}{[\ln(p_{\mathrm{T}}^{\mathrm{EM}})]^2} + \frac{a_3}{[\ln(p_{\mathrm{T}}^{\mathrm{EM}})]^3} \stackrel{?}{=} \frac{p_{\mathrm{T}}^{\mathrm{EM}}}{p_{\mathrm{T}}^{\mathrm{Gen}}}. \tag{9.6}$$

Any discrepancy was assigned as a systematic uncertainty. The main reason for this discrepancy was the assignment of an average response for an entire p_{T} bin. This closure deviated from one at low p_{T}, especially for multi-pronged taus (7%).

The other main contribution to the uncertainty was in the hadronic shower model which yields a maximum uncertainty of 3% (6%) for single (multi-) pronged taus. Variations on the event generator, detector material, EM scale, and on the cell noise threshold for clustering yield uncertainties less than 2%. The overall uncertainties were computed separately for taus binned in p_{T}, η, and number of prongs (Table 9.2).

N_{trk}	η	$p_{\mathrm{T}} < 20$ GeV	$20 < p_{\mathrm{T}} < 30$ GeV	$p_{\mathrm{T}} > 30$ GeV
1	$\lvert\eta\rvert < 1.3$	4.5	3.5	2.5
	$1.3 < \lvert\eta\rvert < 1.6$	7.0	7.0	7.0
	$\lvert\eta\rvert > 1.6$	4.5	4.5	4.5
3	$\lvert\eta\rvert < 1.3$	14	10	8.0
	$1.3 < \lvert\eta\rvert < 1.6$	7.0	7.0	7.0
	$\lvert\eta\rvert > 1.6$	6.5	6.5	6.5

Table 9.2: The uncertainty of the hadronic tau energy scale is shown split into bins of p_{T}, η, and number of tracks associated with the tau candidate (N_{trk}).

Figure 9.4(b) shows the tau p_{T} distribution before and after applying the energy scale variations.

9.3.2 $E_{\mathrm{T}}^{\mathrm{miss}}$ Energy Scale

Early $< E/P >$ studies performed in data and MC showed that the simulation mis-measures the E_{T} of central ($|\eta| < 3.2$) clusters by about 20% for clusters with $E_{\mathrm{T}} < 0.5$ GeV and 5% at high E_{T}. At high rapidity ($|\eta| > 3.2$), the clusters' energies were mis-measured by

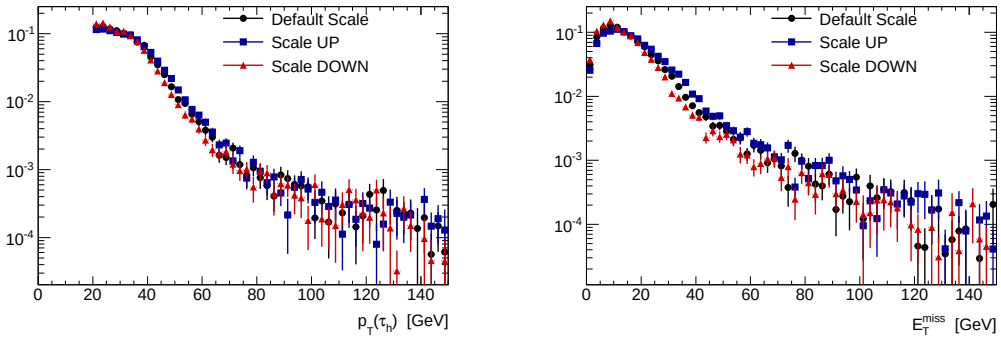

(a) (b)

Figure 9.4: p_{T} distributions for taus (left) and $E_{\mathrm{T}}^{\mathrm{miss}}$(right) for the nominal case where no scaling is done, and when the scale is shifted up and down.

10% [64, 65]. The $E_{\mathrm{T}}^{\mathrm{miss}}$ scale uncertainty was quantified in all final states by scaling all input topological clusters up and down by the following E_{T} dependent scale variations:

$$\mathrm{SV} = \begin{cases} 1 + a(1 + \frac{b}{E_{\mathrm{T}}}) \text{ GeV} & , |\eta| < 3.2 \\ 1 \pm 0.1 & , |\eta| > 3.2 \end{cases} \tag{9.7}$$

The scale variation coefficients, "a" and "b", were chosen to simulate a 20% uncertainty for low E_{T} clusters (~ 0.5 GeV) and an asymptotic 5, 6, or 7% uncertainty for high E_{T} clusters. A flat 10% scale variation was assigned for high pseudorapidity clusters. Figure 9.5 plots the scale variation for central clusters as a function of their E_{T}, while Figure 9.4(b) shows the result of the scaling on the final measured $E_{\mathrm{T}}^{\mathrm{miss}}$.

Table 9.3 shows the effect of scaling the tau, electron ($\tau_h\tau_e$), and $E_{\mathrm{T}}^{\mathrm{miss}}$ energy scale simultaneously on the two semileptonic channels. As was expected, the largest uncertainties occur when the "a" (asymptotic) coefficient is maximal; however, varying the "a" coefficient between 5 and 7% did not greatly change the magnitude of the uncertainty on the signal samples. The background samples have larger uncertainties primarily due to a lack of MC statistics towards the end of the cut-flow. As can be seen in Table 9.6, these uncertainties did not lead to a large uncertainty on the final $N - N_{\mathrm{bkgrd}}$ calculation.

The effect on the $\tau_e\tau_\mu$ final state will be discussed in Section 9.3.3, while this effect on

Shift	$Z \to \tau\tau(e)$	$Z \to ee$	W+Jets	$t\bar{t}$
a=0.07, b=0.93	9.39	29	21.1	10.6
a=0.06, b=1.17	9.21	27	20	11
a=0.05, b=1.50	9.16	24	18.6	10.2
a=-0.05, b=1.50	-9.1	-4.11	-8.74	-12.5
a=-0.06, b=1.17	-9.26	-4.58	-9.07	-12.9
a=-0.07, b=0.93	-9.44	-5.7	-10.1	-13
cluster $\|\eta\| > 3.2$				
a=1.1, b=0	-0.154	1.88	-2.15	1.63
a=0.9, b=0	-0.246	-0.803	-3.36	-0.0744
Shift	$Z \to \tau\tau(\mu)$	$Z \to \mu\mu$	W+Jets	$t\bar{t}$
a=0.07, b=0.93	7.54	24.3	18.1	17.8
a=0.06, b=1.17	7.5	24.1	17.9	17.6
a=0.05, b=1.50	7.4	23.6	18.1	17.9
a=-0.05, b=1.50	-8.24	-17.9	-18.5	-13.5
a=-0.06, b=1.17	-8.42	-19.2	-18.4	-14
a=-0.07, b=0.93	-8.55	-20.1	-18.4	-14.7
cluster $\|\eta\| > 3.2$				
a=1.1, b=0	0.0517	-0.04	-0.0895	0.129
a=0.9, b=0	-0.0501	0.617	-3.71	1.5

Table 9.3: The effect of shifting the cluster energies along with shifting the τ energy on the final event yield. For the electron channel, the electron energy is also scaled up or down depending on the sign of a.

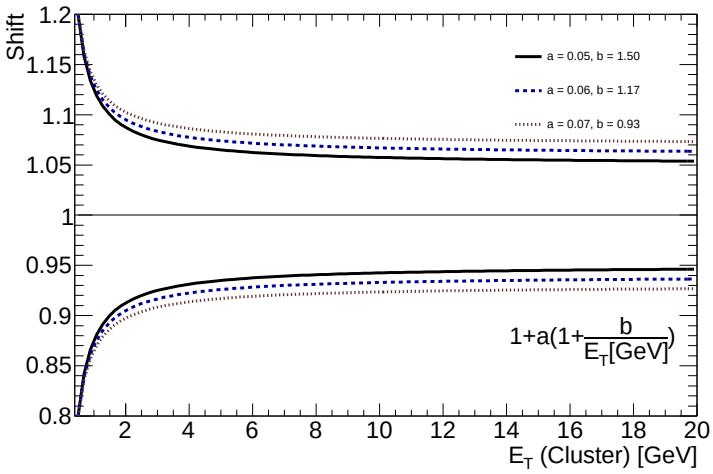

Figure 9.5: The functional form for the scale factors used to scale the constituent clusters of the $E_{\mathrm{T}}^{\mathrm{miss}}$. The "a" factors determine the asymptotic behavior, while the "b" factors are chosen such that the maximum scale factor is 20% for clusters with a E_{T} of 0.5 GeV.

the $\tau_\mu\tau_\mu$ final state is negligible since $E_{\mathrm{T}}^{\mathrm{miss}}$ is only used in the $\Delta\phi(\mu_1, E_{\mathrm{T}}^{\mathrm{miss}})$[7] variable which was ranked low in the BDT used to distinguish $\gamma^*/Z \to \tau\tau$ events from $\gamma^*/Z \to \mu\mu$ events.

9.3.3 Jet Energy Scale

The jet energy scale uncertainty was measured in η bins roughly corresponding to the hadronic calorimeter detector segmentation. The central barrel extends from $0 < |\eta| < 0.8$, the barrel-endcap transition and endcap covers $0.8 < |\eta| < 2.8$, the Hadronic Endcap and Forward Calorimeter transition covers $2.8 < |\eta| < 3.2$, while the Forward Calorimeter covers $3.2 < |\eta| < 4.5$. As a baseline, the uncertainty for all η regions used the measurement in the central region, since the detector geometry is most well understood there, and the test beam measurements measuring calorimeter response only extended over the Tile region of the calorimeter. Six sources of uncertainty were considered for the JES: the uncertainty due to the JES calibration method, calorimeter response, detector simulation, event generator, relative contribution for jets with $|\eta| < 0.8$, and pileup [46]. Each individual component

[7]The difference in azimuthal angle between the direction of the $E_{\mathrm{T}}^{\mathrm{miss}}$ and the leading muon candidate.

was then summed in quadrature to give the total systematic uncertainties per η region (Table 9.4).

η region	Maximum fraction JES Uncertainty		
	$p_{\mathrm{T}}^{\mathrm{Jet}} = 20$ GeV	$p_{\mathrm{T}}^{\mathrm{Jet}} = 200$ GeV	$p_{\mathrm{T}}^{\mathrm{Jet}} = 1.5$ TeV
$0 < \lvert\eta\rvert < 0.3$	4.1 %	2.3%	3.1%
$0.3 < \lvert\eta\rvert < 0.8$	4.3 %	2.4%	3.3%
$0.8 < \lvert\eta\rvert < 1.2$	4.3 %	2.5%	3.5%
$1.2 < \lvert\eta\rvert < 2.1$	5.2 %	2.6%	3.6%
$2.1 < \lvert\eta\rvert < 2.8$	8.2 %	2.9%	
$2.8 < \lvert\eta\rvert < 3.2$	10.1%	3.5%	
$3.2 < \lvert\eta\rvert < 3.6$	10.3%	3.7%	
$3.6 < \lvert\eta\rvert < 4.5$	13.8%	5.3%	

Table 9.4: The overall systematic uncertainties of jets of 20, 200, and 1500GeV divided in bins of pseudorapidity [46].

The $\tau_e\tau_\mu$ final state, which was the only analysis to use jets directly, measured a total systematic on the jet, $E_{\mathrm{T}}^{\mathrm{miss}}$, and electron energy scale by varying all three uncertainties simultaneously both up and down by one σ. Shifts on the energy of the electron were propagated to the $E_{\mathrm{T}}^{\mathrm{miss}}$ while those for jets were not, since the $E_{\mathrm{T}}^{\mathrm{miss}}$ was not measured using fully reconstructed jets. The effect on the signal sample averaged 1.7% relative to the default event selection.

9.3.4 Electron Energy Scale

The electromagnetic (EM) response of the LAr calorimeter has been calibrated using test beam data [66] with an uncertainty less than 3% in the barrel region, and about 5% in the high $|\eta|$ regions [48]. The test beam analysis approximated the ATLAS environment by placing pixel, SCT, and TRT modules upstream of the LAr module. The majority of the calibration uncertainty arises from extrapolating the results of the test beam setup to

the actual ATLAS detector environment. The EM calibration scale was further refined after a sufficient data set of $Z \to ee$ and J/ψ events could be collected. Recalibrating the EM scale with Z bosons in collision data provides the advantage of being able to perform the calibration using particles of a well-known mass and within the true ATLAS detector environment. Uncertainties on the electron energy scale were found to be between $0.3-1.6\%$ in the barrel region and between $2-3\%$ in the forward regions.

The energy of electrons in data events was rescaled to match the results of the $Z \to ee$ calibration, while the electron energy in MC events was smeared so that the $Z \to ee$ width in MC matched that found in data. The effect of the uncertainty of the electron energy scale on our analysis was evaluated by rerunning over all MC samples both scaling the electrons energy up and down depending on the electron's energy and pseudorapidity. The electron energy scale along with the tau, jet, and $E_{\mathrm{T}}^{\mathrm{miss}}$ scale were all varied in a correlated manner.

9.3.5 Muon Momentum Scale and Resolution

The muon momentum in MC, like that of the electron energy, was smeared such that the $Z \to \mu\mu$ mass peak in MC matched that observed in data events [67]. In order to study the effect of the uncertainty of the smearing, the muon momentum in MC was smeared by $\pm 1\sigma$ of the uncertainty. The effect of the smearing was simultaneously propagated to the $E_{\mathrm{T}}^{\mathrm{miss}}$. An uncertainty never exceeding 0.2% was estimated for the muon momentum scale.

9.4 Background Estimation

The main assumption applied in the estimation of the multijet background for the two semileptonic and the $\tau_e\tau_\mu$ final states is that the $R_{\mathrm{OS/SS}}$ ratio does not depend on the isolation of the selected lepton(s). By tightening the isolation on the selected lepton, more true leptons arising from heavy flavor (c, b) meson decays tend to be removed than fake leptons (or muons from charged π/K decays in flight). If the selected leptons (or selected lepton and hadronic tau) are truly from heavy flavor meson decays, then their charges will tend to be opposite to each other. Thus, by tightening the isolation, the number of OS sign events may be suppressed in a different proportion to SS events, making the measured $R_{\mathrm{OS/SS}}$ dependent on the isolation of the lepton.

In order to measure the potential dependence on the isolation of the selected lepton in the semileptonic final states, the $R_{\mathrm{OS/SS}}$ ratio was measured in bins of lepton isolation. In order to increase the statistics in each of the isolation bins and to suppress the signal at low lepton isolation, the identification on the hadronic tau candidate was reversed. To ensure that there was not an additional dependence on the ratio as a function of hadronic tau identification, the $R_{\mathrm{OS/SS}}$ was again measured in bins of hadronic tau identification in the anti-isolated lepton region. Figure 9.6 summarizes the results. In all sub-figures, the solid line represents the measured nominal value of the ratio, the dashed lines represent one standard deviation in statistical uncertainty, while the boxes around each point estimate signal/EWK/$t\bar{t}$ contamination. The two data points in each bin represent the raw data value of $R_{\mathrm{OS/SS}}$ and the value when all EWK, signal, and $t\bar{t}$ processes were subtracted.

No dependence significantly greater than the statistical uncertainty on $R_{\mathrm{OS/SS}}$ was observed as a function of hadronic tau identification or lepton isolation. The maximal deviation from the nominal measured $R_{\mathrm{OS/SS}}$ as a function of the isolation was taken as a systematic uncertainty. A similar procedure was used for the $\tau_e\tau_\mu$ final state, except that dependencies on the isolation were measured for both leptons. The measured systematic uncertainties were 7, 4, and 13% for the $\tau_h\tau_e$, $\tau_h\tau_\mu$, and $\tau_e\tau_\mu$ final states, respectively.

An additional systematic was considered in the $\tau_e\tau_\mu$ final state since the multijet contribution was estimated only after the dilepton veto and then extrapolated to the final signal region. The assumption is that the cut efficiency for the $\Sigma\cos\Delta(\phi)$, the ΣE_{T}, and the m_{vis} window is independent of lepton isolation. Once again this assumption was tested as a function of the lepton isolation. Figure 9.7 shows the cut efficiency as a function of the lepton isolation for both electrons and muons and both track and calorimeter isolation. When measuring the dependence as a function of muon (electron) isolation, the electron (muon) isolation is not applied to increase the data statistics and decrease signal, EWK, and $t\bar{t}$ contamination. A linear regression was performed on each of the plots, where the first bin, due to large signal contamination, was not included in the fit. If the slope of the regression, together with the fit uncertainty was not consistent with 0, then a systematic

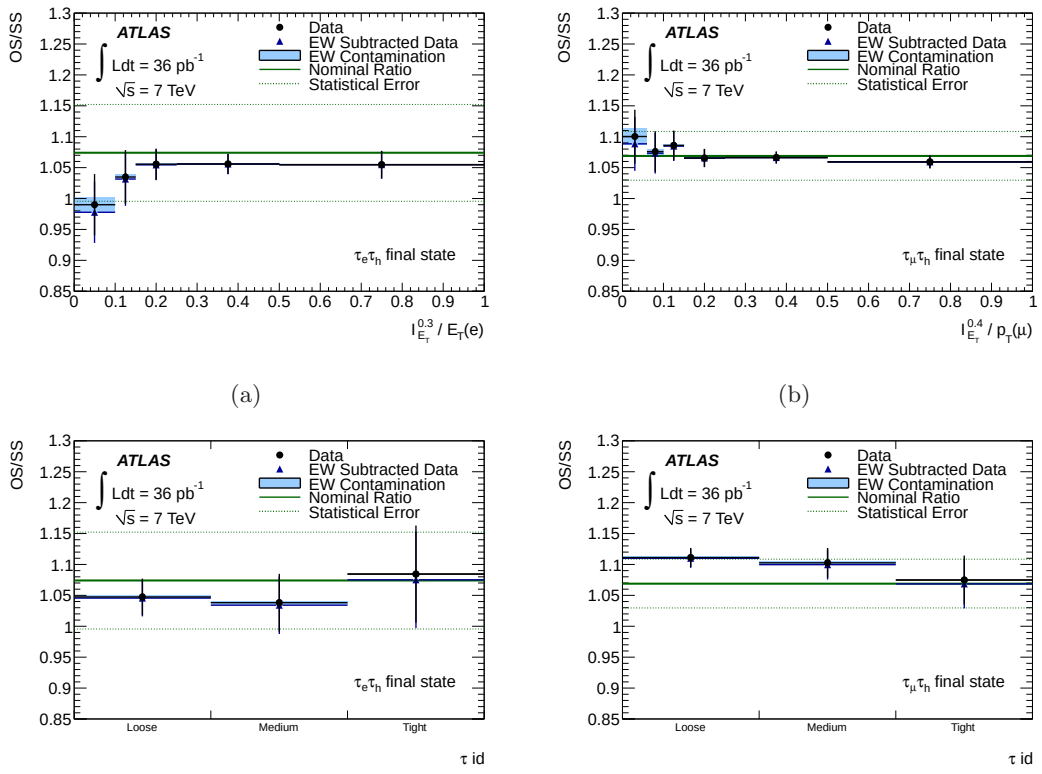

Figure 9.6: R_{OSSS} as a function of calorimeter isolation on the top and as a function of tau identification on the bottom for the $\tau_h\tau_e$ final state (left) and the $\tau_h\tau_\mu$ final state (right). The solid line represents the nominal measured R_{OSSS}, while the dashed lines mark one sigma in statistical uncertainty. The estimated electroweak contribution is shown as the solid box over each point.

was derived by

$$\frac{R_{\rm ex}}{R^{'}_{\rm OS/SS}} - 1 \tag{9.8}$$

where $R_{\rm ex}$ is the extrapolation of the linear fit to the first bin (signal region) and $R^{'}_{\rm OS/SS}$ is the cumulative measured $R_{\rm OS/SS}$ in the remaining bins. The largest systematic uncertainty, was measured in the cut efficiency as a function of the electron calorimeter isolation (Figure 9.7(a)). This systematic uncertainty, 3%, was added in quadrature with the uncertainty on $R_{\rm OS/SS}$ to yield the final uncertainty of 13% on the multijet background estimate method.

The systematic uncertainty on the multijet estimate for the $\tau_\mu\tau_\mu$ final state was derived by fluctuating the measured correlation "k"[8] factors within their uncertainties and was measured to be 6.5% (Table 7.3).

9.5 Muon d_0 Simulation ($\tau_\mu\tau_\mu$)

The variable that provided the best separation between $\gamma^*/Z \to \mu\mu$ and $\gamma^*/Z \to \tau\tau$ events was the sum of the absolute values of the transverse impact parameters of the muon track ($d_0(\mu_i)$) extrapolated to the reconstructed primary vertex ($|d_0(\mu_1)| + |d_0(\mu_2)|$). The d_0 is expected to be larger, on average, in $\gamma^*/Z \to \tau\tau$ events than in $\gamma^*/Z \to \mu\mu$ events due to the secondary decay vertex from the tau lepton decay (Figure 6.12 in Section 6.5.3). In order to effectively use this variable, the d_0 distribution must be accurately modeled in the MC simulation. Figure 9.8 shows the lead muon d_0 distribution before and after muon d_0 smearing in a $\gamma^*/Z \to \mu\mu$ rich control region. The d_0 distribution was generally wider in MC than in data.

Both the data and MC d_0 distributions were fit to a double Gaussian distribution where the separate Gaussians are known as either "inner" or "outer" (shown in Figure 9.9). The MC d_0 distribution was then smeared for both the lead and sub-leading muon in each event by:

$$d_0({\rm MC})_{\rm smeared} = d_0({\rm MC}) + G(\mu, \sigma), \tag{9.9}$$

[8]The factor intended to correct for any correlations between the isolation of the two selected muons in the ABCD method used to estimate the multijet background in the $\tau_\mu\tau_\mu$ final state (Section 7.3).

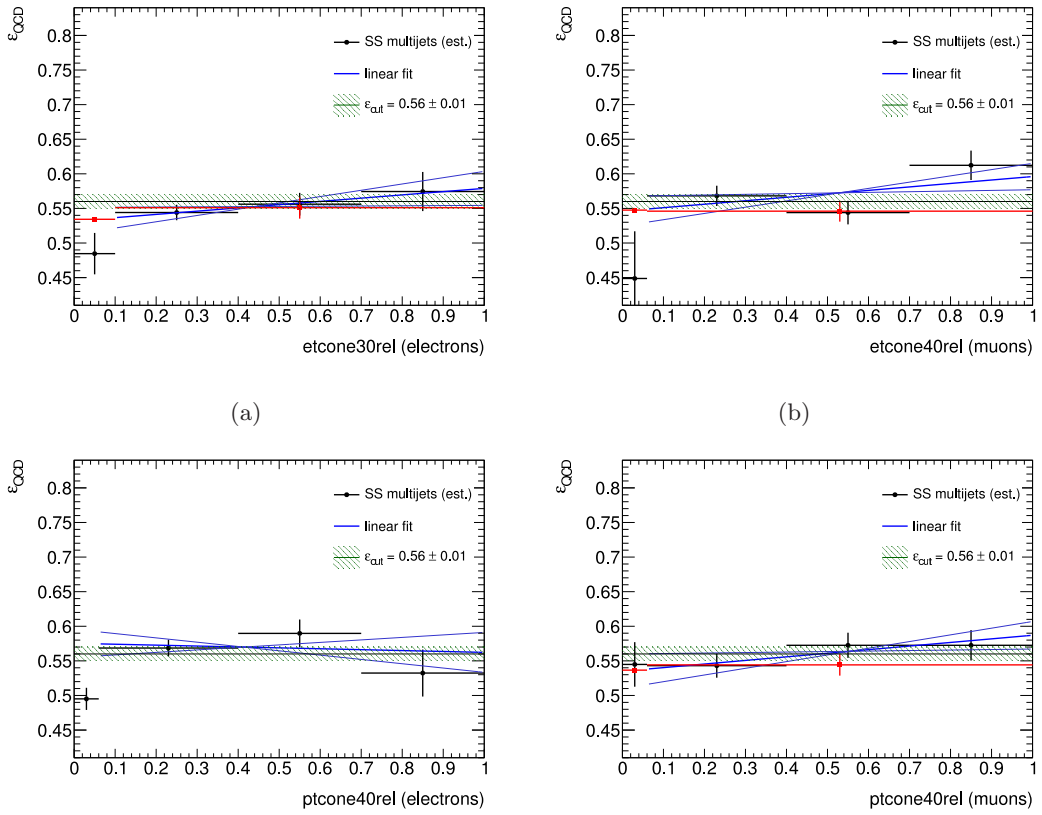

(a) (b)

(c) (d)

Figure 9.7: The cut efficiency as a function of calorimeter isolation on the top and as a function of tracker isolation on the bottom for the electrons on the left and muons on the right in the $\tau_e\tau_\mu$ final state. The solid line represents the nominal measured ϵ(Multijet), the dashed region represents its statistical uncertainty, the solid circles the measured ratio per isolation bin, the solid sloped lines represent a linear fit together with $\pm 1\sigma$ of the fit uncertainty, and the solid squares, when present either represent the extrapolation of the linear fit to the signal region bin or the cumulative average of the anti-isolated bins. Any EWK/$t\bar{t}$/signal contamination is removed.

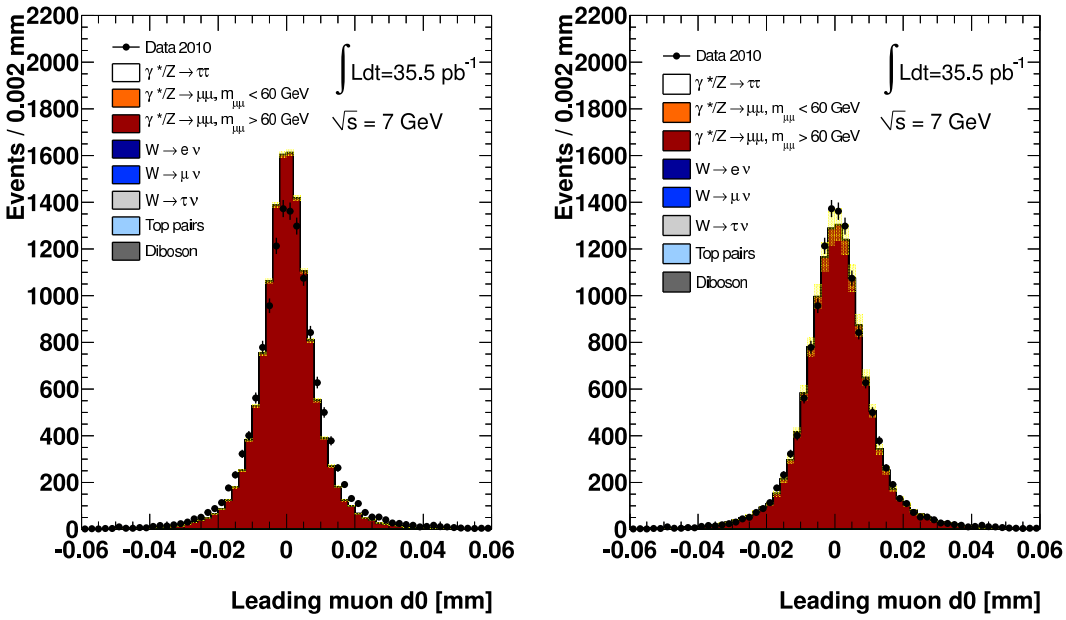

(a) (b)

Figure 9.8: The lead muon d_0 distribution before (left) and after (right) smearing in MC.

where $G(\mu, \sigma)$ is a normal distribution with a mean of μ and width of σ. The mean of G was constructed as the difference of the data double Gaussian mean by the MC double Gaussian mean (The mean of the double Gaussian was defined as the weighted sum of the "inner" and "outer" means). The width of G was defined as (using i for "inner" and o for "outer"):

$$\sigma(i,o) = \sqrt{\sigma^2_{\text{data}}(i,o) - \sigma^2_{\text{MC}}(i,o)} \tag{9.10}$$

where the choice of $\sigma(i,o)$ was made randomly, muon by muon, based on the relative weights of the "inner" and "outer" Gaussians in the MC distribution at a particular d_0 value.

Three systematic uncertainties were considered for the d_0 smearing procedure: the muon d_0 width, the muon d_0 shape, and the muon d_0 scale. The uncertainty on the width of the smearing function, G, was evaluated by adjusting the widths by $\pm 1\sigma$ and observing the relative change in the event counts. The shape uncertainty was evaluated by smearing the d_0 using a single Gaussian which was a weighted sum of the "inner" and "outer" Gaussians. Finally, the scale uncertainty was evaluated by comparing the tails of the data and the smeared MC d_0 distributions ($|d_0| > 4$ mm). Uncertainties of 0.5, 1.1, and 2.0% were observed for the width, shape, and scale uncertainties, respectively.

9.6 Object Quality

As mentioned in Section 6.1, since the variables used to reject events based on poorly or anomalously reconstructed jets was not well modeled in simulation, jet object quality requirements were only applied to data events. To evaluate this effect on the simulated samples, an efficiency function, parameterized in jet rapidity and transverse momentum, was applied to each jet in the simulated samples. Events with jets that failed the efficiency function were subsequently vetoed. The effect of this modified jet object quality procedure on MC signal samples was 1.8, 0.4, and 0% in the two semileptonic final states, the $\tau_e\tau_\mu$ final state, and the $\tau_\mu\tau_\mu$ final state, respectively. The effect on the background samples ranged from 2% for $\gamma^*/Z \to \ell\ell$ events to 5% for the busier $t\bar{t}$ events.

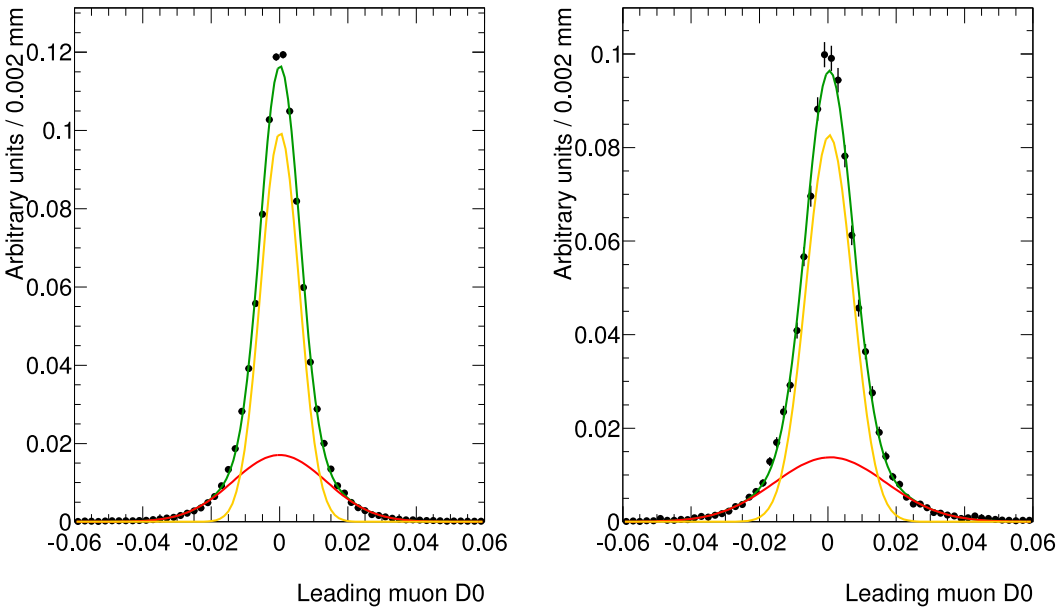

(a) (b)

Figure 9.9: The lead muon d_0 distribution fit to a double Gaussian in data (left) and MC (right). The wider Gaussian is referred to as the "outer" Gaussian, while the narrower Gaussian is referred to as the "inner" Gaussian.

9.7 Theoretical Cross-Section

The extraction of the multijet background (Chapter 7) relied on MC predictions for estimating both EWK/$t\bar{t}$ and signal impurities in the control regions. In addition, all EWK/$t\bar{t}$ backgrounds were directly subtracted in the final mass windows. Thus, the final cross-section measurement was dependent on the predicted theoretical cross-section for each of the background processes. In order to measure this dependence, the entire background extraction and cross-sections were measured while simultaneously scaling all cross-sections up and down by their uncertainties (Table 4.2). The uncertainties on the $Z \to \ell\ell$, $W \to \ell\nu$, and $t\bar{t}$ cross-sections were considered as correlated since they largely depended on the same PDF sets and programs. Since the $W \to \ell\nu$ MC was scaled to match data in the two semileptonic channels, the uncertainty of the $W \to \ell\nu$ cross-section was not considered.

9.8 Geometric and Kinematic Acceptance

The uncertainty on the geometric and kinematic acceptance factor (A_Z) arises primarily from the uncertainty in the parton distribution function (PDF) used to generate the $\gamma^*/Z \to \tau\tau$ events and the by the modeling of the subsequent parton shower.

The uncertainty on the PDF set was analyzed both within a single PDF set, and amongst multiple PDF sets. To quantify the uncertainty within a given PDF set, the `CTEQ6.6` next-to-leading order (NLO) PDF set was used along with its 22 error eigenvectors. These eigenvectors are meant to cover the uncertainties of the parton parameter space resulting from the input experimental uncertainties [37]. The default signal sample was then reweighted according to each eigenvector and the resulting differences were added in quadrature to yield an uncertainty of 1.2%. The uncertainty due to PDF choice was evaluated by measuring the difference between the acceptance factor when using `CTEQ6.6` or `HERAAPDF1.0` [68] and when using the default PDF set of `MRSTLO*`. A maximal difference of 1.8% was observed between choices of PDF sets.

The uncertainty due to the parton showering model was performed by generating events with `MC@NLO` interfaced with `HERWIG` using the `CTEQ6.6` PDF set and the additional `ATLAS MC` tune [38]. The default parton showering was performed with `PYTHIA` using the `MRSTLO*`

PDF set and the additional `ATLAS MC` tune. The default case was reweighted to the `CTEQ6.6` PDF set in order to perform a fair comparison between the two parton showering models. Differences of less than 2% were observed in both semileptonic final states.

Variation	$\tau_h\tau_e$	$\tau_h\tau_\mu$
Variation w/i PDF set	1.2%	1.2%
Different PDF sets	1.9%	1.9%
Model dependence	1.8%	1.6%
Total	2.9%	2.8%

Table 9.5: The individual components to the uncertainty on the theoretical acceptance for the two semileptonic final states.

The relative contributions from each source of uncertainty are shown in Table 9.5 for the two semileptonic final states. The total uncertainty on A_Z was derived by adding the individual components in quadrature. The total uncertainty on A_Z was measured as 2.9, 2.8, 2.9, and 4.0% in the $\tau_h\tau_e$, $\tau_h\tau_\mu$, $\tau_e\tau_\mu$, and $\tau_\mu\tau_\mu$ final states, respectively.

9.9 Luminosity

An explanation of the ATLAS luminosity calculation can be found in Appendix A. The main uncertainties in the luminosity calculation arose from:

- **beam intensities:**

  Having a precise knowledge of the number of protons in each colliding bunch.

- **Length-Scale Calibration**

  Having a precise knowledge of the distance between the two beams during each (vdM) scan.

- **Imperfect Beam Centering**

  Slight deviations from zero separation in the direction transverse to the scan direction

will systematically lower the measured interaction rate in all separation points in the scan direction.

- **Choice of Fit Model**

  A double Gaussian fit was used in preference to a single Gaussian fit for the extraction of the horizontal and vertical beam profiles due to a lower $\chi^2/NDoF$. A cubic spline fit model was used as an alternative to the double Gaussian.

All systematic uncertainties, except for the beam intensity measurement, were estimated to be less than 1% [69]. The beam intensity uncertainty was measured as 3.1%. Combining all systematic uncertainties, the relative uncertainty on the luminosity was estimated to be 3.4%.

9.10 Summary

Table 9.6 summarizes the effect that each systematic uncertainty had on the detector acceptance (C_Z), the predicted number of events after full background subtraction ($N - N_{\text{bkgrd}}$), and on the final cross-section measurement, for the two semileptonic final states. Table 9.7 provides the analogous information for the two leptonic final states. If the uncertainties on C_Z and on $N - N_{\text{bkgrd}}$ shift in the same direction (positively correlated), then the relative uncertainty on the cross-section is approximately the difference of the relative uncertainties on C_Z and $N - N_{\text{bkgrd}}$, while if C_Z and $N - N_{\text{bkgrd}}$ shift in opposite directions (negatively correlated), the relative uncertainty on the cross-section is approximately the sum of the relative uncertainties on C_Z and $N - N_{\text{bkgrd}}$. The $\tau_h\tau_e$, $\tau_h\tau_\mu$, and $\tau_\mu\tau_\mu$ final states all had systematic uncertainties on C_Z and $N - N_{\text{bkgrd}}$ that tended to be negatively correlated resulting in larger uncertainties on the corresponding cross-sections, while the $\tau_e\tau_\mu$ final state tended to have uncertainties that were positively correlated allowing the uncertainties on C_Z and $N - N_{\text{bkgrd}}$ to partially compensate each other, leading to a smaller uncertainty on the resultant cross-section.

Table 9.8 summarizes the effect that each systematic uncertainty had on the cross-section measurement in each final state. The second to last column in the Table 9.8 describes whether the systematic uncertainty was considered to be correlated amongst the four final

	$\tau_h\tau_e$			$\tau_h\tau_\mu$		
Systematic Uncertainty	C_Z	$N - N_{\text{bkgrd}}$	σ	C_Z	$N - N_{\text{bkgrd}}$	σ
Electron efficiency	9.2%	0.31%	9.6%	–	–	–
Electron charge mis-id.	0.2%	0.014%	0.2%	–	–	–
Muon efficiency	–	–	–	3.6%	0.24%	3.8%
Muon resolution & energy scale	–	–	–	0.2%	0.018%	0.2%
τ_h identification efficiency	8.6%	0.11%	8.6%	8.6%	0.078%	8.6%
τ_h mis-identification	–	0.66%	0.7%	–	1.1%	1.1%
Energy scale (e/τ/jets/$E_{\text{T}}^{\text{miss}}$)	9.4%	1.3%	11%	8.6%	1.7%	10%
Multijet estimate method	–	2%	2%	–	0.76%	0.8%
W normalization factor	–	0.18%	0.2%	–	0.12%	0.1%
Object quality cuts	1.8%	0.07%	1.9%	1.8%	0.07%	1.9%
pile-up description in sim.	0.4%	0.02%	0.4%	0.4%	0.029%	0.4%
Theoret. cross-section	–	0.12%	0.1%	–	0.2%	0.2%
A_Z systematics	–	–	3%	–	–	3%
Total Systematic uncertainty	16%	2.5%	17%	13%	2.2%	15%
Statistical uncertainty	1.4%	12%	12%	1.2%	9.8%	9.8%
Luminosity	–	–	3.4%	–	–	3.4%

Table 9.6: A summary of the effect of each systematic uncertainty on the measured C_Z, predicted $N - N_{\text{bkgrd}}$, and the measured cross-section. The systematic uncertainty on the cross-section from each source is computed by fully accounting for correlations between the measured C_Z and the $N - N_{\text{bkgrd}}$. The total systematic on the cross-section measurement is obtained by adding each individual source in quadrature.

	$\tau_e\tau_\mu$			$\tau_\mu\tau_\mu$		
Systematic Uncertainty	C_Z	$N - N_{\text{bkgrd}}$	σ	C_Z	$N - N_{\text{bkgrd}}$	σ
Electron efficiency	6.1%	0.20%	5.9%	–	–	–
Electron charge mis-id.	0.28%	0.016%	0.3%	–	–	–
Muon efficiency	2.6%	0.33%	2.2%	4.7%	3.9%	8.6%
Muon d0 (shape and scale)	–	–	–	2.2%	4.8%	6.2%
Muon resolution & energy scale	0.05%	0.00%	0.1%	0.46%	0.59%	1.0%
Energy scale (e/jets/$E_{\text{T}}^{\text{miss}}$)	1.7%	0.03%	1.7%	–	–	–
Multijet estimate method	0%	0.97%	1.0%	0%	1.7%	1.7%
Object quality cuts	0.35%	0.015%	0.4%	0.23%	0.12%	0.4%
pile-up description in sim.	0.57%	0.034%	0.5%	0%	0.1%	0.1%
Theoret. cross-section	0%	0.30%	0.3%	0%	4.3%	4.3%
A_Z systematics	–	–	3%	–	–	4%
Total Systematic uncertainty	7.1%	1.1%	7.3%	5.2%	7.4%	14%
Statistical uncertainty	1.2%	13%	13%	2.0%	23%	23%
Luminosity	–	–	3.4%	–	–	3.4%

Table 9.7: A summary of the effect of each systematic uncertainty on the measured C_Z, predicted $N - N_{\text{bkgrd}}$, and the measured cross-section. The systematic uncertainty on the cross-section from each source is computed by fully accounting for correlations between the measured C_Z and the $N - N_{\text{bkgrd}}$. The total systematic on the cross-section measurement is obtained by adding each individual source in quadrature.

Systematic uncertainty	$\tau_h\tau_e$	$\tau_h\tau_\mu$	$\tau_e\tau_\mu$	$\tau_\mu\tau_\mu$	Correlation	Combined
Electron efficiency, resolution &						
e charge mis-identification	9.6%	–	5.9%	–	✓	1.6%
Muon efficiency	–	3.8%	2.2%	8.6%	✓	0.80%
Muon d_0 (shape and scale)	–	–	–	6.2%	X	0.83%
Muon resolution & energy scale	–	0.2%	0.1%	1.0%	✓	0.09%
τ_h identification efficiency	8.6%	8.6%	–	–	✓	3.8%
τ_h mis-identification	0.7%	1.1%	–	–	✓	0.43%
Energy scale (e/τ/jets/$E_{\mathrm{T}}^{\mathrm{miss}}$)	11%	10%	1.7%	0.0%	✓	3.9%
Multijet estimate method	2%	0.8%	1.0%	1.7%	(✓)	0.23%
W normalization factor	0.2%	0.1%	–	–	X	0.05%
Object quality cuts	1.9%	1.9%	0.4%	0.4%	✓	0.63%
pile-up description in simulation	0.4%	0.4%	0.5%	0.1%	✓	0.06%
Theoret. cross-section	0.1%	0.2%	0.3%	4.3%	✓	0.53%
A_Z systematics	3%	3%	3%	4%	✓	3.1%
Total Systematic uncertainty	17%	15%	7.3%	14%		6.6%
Statistical uncertainty	12%	9.8%	13%	23%	X	7.4%
Luminosity	3.4%	3.4%	3.4%	3.4%	✓	3.4%

Table 9.8: Relative statistical and systematic uncertainties in % on the total cross-section measurement. The electron and muon efficiency terms include the lepton trigger, reconstruction, identification and isolation uncertainties, as described in the text. The last column indicates whether a given systematic uncertainty is treated as correlated (✓) or uncorrelated (X) among the relevant channels when combining the results, as described in Section 8.3.1. For the multijet background estimation method, the uncertainties in the $\tau_h\tau_e$, $\tau_h\tau_\mu$, and $\tau_e\tau_\mu$ channels are treated as correlated while the $\tau_\mu\tau_\mu$ uncertainty is treated as uncorrelated, since a different method is used, as described in Section 7. The final column lists the effect of each uncertainty on the final combined cross-section.

states (Section 8.3.2) or not. The last column shows the effect that the uncertainty had on the combined cross-section measurement (Section 8.3.1). The two largest contributors to the total combined systematic uncertainty are the hadronic tau identification efficiency and the energy scale for electrons, taus, jets, and the missing energy. Overall, the largest source of uncertainty in the cross-section measurement was statistical.

Chapter 10

SUMMARY

The $Z \rightarrow \tau\tau$ combined cross-section was measured to be:

$$\sigma = 0.97 \pm 0.07 \text{ (stat.)} \pm 0.06 \text{ (sys.)} \pm 0.03 \text{ (lumi.) nb.} \tag{10.1}$$

This is in good agreement with the next-to-next-to-leading order prediction of:

$$\sigma(\text{NNLO}) = 0.96 \pm 0.05\text{nb.} \tag{10.2}$$

The majority of the uncertainty in the cross-section measurement was statistical in the two leptonic channels, while the majority of the uncertainty in the two hadronic channels was due to the systematic uncertainty of the tau identification efficiency and energy scale efficiency. In addition the electron identification efficiency proved to be a major contribution in the $\tau_h\tau_e$ final state.

In order to discover the Standard Model Higgs (or other new physics) with two tau leptons in the final state, the $Z \rightarrow \tau\tau$ background must be very well understood. Figure 10.1 [70] shows the invariant mass distribution[1] of the candidate ditau pair after a $H \rightarrow \tau\tau \rightarrow \tau_h\tau_\ell$ event selection. It is evident that the overwhelming background arises from the $Z \rightarrow \tau\tau$ background. Our $Z \rightarrow \tau\tau$ cross-section measurement shows that a ditau event selection can be performed. In addition, continued studies of $Z \rightarrow \tau\tau$ events will allow us to minimize the systematic uncertainties on the hadronic tau energy scale and identification efficiency allowing us to make a definitive claim on a discovery or refutation of a low mass SM Higgs.

[1] After this analysis was completed, a new method was introduced to reconstruct the invariant mass of the ditau pair accounting for the energy of the neutrinos in the final state. This is called the missing mass calculator (MMC) [71]

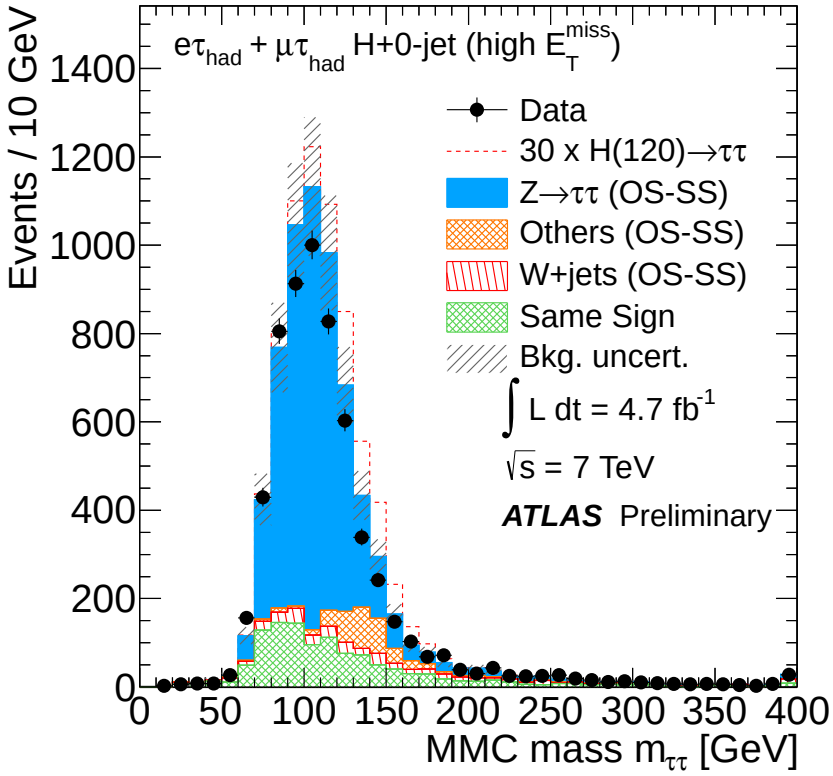

Figure 10.1: The invariant mass of the selected $\tau\tau$ pair in the $H \to \tau\tau \to \tau_h\tau_\ell$ analysis [70] using the missing mass calculator MMC [71]. The mass distribution is shown when no additional jets in the event are selected. A $H(120) \to \tau\tau$ signal is also shown. As was done in the $Z \to \tau\tau$ cross-section analysis, the multijet background was estimated from data and all other backgrounds were estimated from MC (with the W+jets background scaled to data).

BIBLIOGRAPHY

[1] D. M. Fradkin, "Comments on a paper by majorana concerning elementary particles," *American Journal of Physics*, vol. 34, no. 4, pp. 314–318, 1966.

[2] W. Rodejohann, "Neutrino-less Double Beta Decay and Particle Physics," *Int. J. Mod. Phys.*, vol. E20, pp. 1833–1930, 2011.

[3] S. L. Glashow, "Partial Symmetries of Weak Interactions," *Nucl. Phys.*, vol. 22, pp. 579–588, 1961.

[4] S. Weinberg, "A model of leptons," *Phys. Rev. Lett.*, vol. 19, pp. 1264–1266, Nov 1967.

[5] The ATLAS Collaboration, "Combination of Higgs Boson Searches with up to 4.9 fb^{-1} of pp Collisions Data Taken at a center-of-mass energy of 7 TeV with the ATLAS Experiment at the LHC," Tech. Rep. ATLAS-CONF-2011-163, CERN, Geneva, Dec 2011.

[6] The CMS Collaboration, "Combination of SM Higgs Searches," no. CMS-PAS-HIG-11-032, 2011.

[7] R. Barate *et al.*, "Search for the Standard Model Higgs boson at LEP," *Physics Letters B*, vol. 565, pp. 61 – 75, 2003.

[8] M. L. Perl, G. S. Abrams, A. M. Boyarski, M. Breidenbach, D. D. Briggs, F. Bulos, W. Chinowsky, J. T. Dakin, G. J. Feldman, C. E. Friedberg, D. Fryberger, G. Goldhaber, G. Hanson, F. B. Heile, B. Jean-Marie, J. A. Kadyk, R. R. Larsen, A. M. Litke, D. Lüke, B. A. Lulu, V. Lüth, D. Lyon, C. C. Morehouse, J. M. Paterson, F. M. Pierre, T. P. Pun, P. A. Rapidis, B. Richter, B. Sadoulet, R. F. Schwitters, W. Tanenbaum, G. H. Trilling, F. Vannucci, J. S. Whitaker, F. C. Winkelmann, and J. E. Wiss, "Evidence for anomalous lepton production in $e^+ - e^-$ annihilation," *Phys. Rev. Lett.*, vol. 35, pp. 1489–1492, Dec 1975.

[9] K. Nakamura *et al.*, "Review of particle physics," *J. Phys.*, vol. G37, p. 075021, 2010.

[10] S. Dittmaier, C. Mariotti, G. Passarino, R. Tanaka, S. Alekhin, J. Alwall, E. A. Bagnaschi, A. Banfi, J. Blumlein, S. Bolognesi, N. Chanon, T. Cheng, L. Cieri, A. M. Cooper-Sarkar, M. Cutajar, S. Dawson, G. Davies, N. De Filippis, G. Degrassi, A. Denner, D. D'Enterria, S. Diglio, B. Di Micco, R. Di Nardo, R. K. Ellis, A. Farilla, S. Farrington, M. Felcini, G. Ferrera, M. Flechl, D. de Florian, S. Forte,

S. Ganjour, M. V. Garzelli, S. Gascon-Shotkin, S. Glazov, S. Goria, M. Grazzini, J.-P. Guillet, C. Hackstein, K. Hamilton, R. Harlander, M. Hauru, S. Heinemeyer, S. Hoche, J. Huston, C. Jackson, P. Jimenez-Delgado, M. D. Jorgensen, M. Kado, S. Kallweit, A. Kardos, N. Kauer, H. Kim, M. Kovac, M. Kramer, F. Krauss, C.-M. Kuo, S. Lehti, Q. Li, N. Lorenzo, F. Maltoni, B. Mellado, S. O. Moch, A. Muck, M. Muhlleitner, P. Nadolsky, P. Nason, C. Neu, A. Nikitenko, C. Oleari, J. Olsen, S. Palmer, S. Paganis, C. G. Papadopoulos, T. C. Petersen, F. Petriello, F. Petrucci, G. Piacquadio, E. Pilon, C. T. Potter, J. Price, I. Puljak, W. Quayle, V. Radescu, D. Rebuzzi, L. Reina, J. Rojo, D. Rosco, G. P. Salam, A. Sapronov, J. Schaarschmidt, M. Schonherr, M. Schumacher, F. Siegert, P. Slavich, M. Spira, I. W. Stewart, W. J. Stirling, F. Stockli, C. Sturm, F. J. Tackmann, R. S. Thorne, D. Tommasini, P. Torrielli, F. Tramontano, Z. Trocsanyi, M. Ubiali, S. Uccirati, M. Vazquez Acosta, T. Vickey, A. Vicini, W. J. Waalewijn, D. Wackeroth, M. Warsinsky, M. Weber, M. Wiesemann, G. Weiglein, J. Yu, and G. Zanderighi, "Handbook of LHC Higgs Cross Sections: 2. Differential Distributions," Tech. Rep. arXiv:1201.3084, Jan 2012. Comments: to be submitted to CERN Report. Working Group web page: https://twiki.cern.ch/twiki/bin/view/LHCPhysics/CrossSections.

[11] F. Hasert, H. Faissner, W. Krenz, J. V. Krogh, D. Lanske, J. Morfin, K. Schultze, H. Weerts, G. Bertrand-Coremans, J. Lemonne, J. Sacton, W. V. Doninck, P. Vilain, C. Baltay, D. Cundy, D. Haidt, M. Jaffre, P. Musset, A. Pullia, S. Natali, J. Pattison, D. Perkins, A. Rousset, W. Venus, H. Wachsmuth, V. Brisson, B. Degrange, M. Haguenauer, L. Kluberg, U. Nguyen-Khac, P. Petiau, E. Bellotti, S. Bonetti, D. Cavalli, C. Conta, E. Fiorini, M. Rollier, B. Aubert, L. Chounet, P. Heusse, A. Lagarrigue, A. Lutz, J. Vialle, F. Bullock, M. Esten, T. Jones, J. McKenzie, A. Michette, G. Myatt, J. Pinfold, and W. Scott, "Search for elastic muon-neutrino electron scattering," *Physics Letters B*, vol. 46, no. 1, pp. 121 – 124, 1973.

[12] F. J. Hasert *et al.*, "Observation of neutrino-like interactions without muon or electron in the Gargamelle neutrino experiment," *Phys. Lett.*, vol. B46, pp. 138–140, 1973.

[13] F. J. Hasert *et al.*, "Observation of neutrino-like interactions without muon or electron in the Gargamelle neutrino experiment," *Nucl. Phys.*, vol. B73, pp. 1–22, 1974.

[14] G. Arnison *et al.*, "Experimental observation of lepton pairs of invariant mass around 95 GeV/c^2 at the CERN SPS collider," *Phys. Lett.*, vol. B126, pp. 398–410, 1983.

[15] P. Bagnaia *et al.*, "Evidence for $Z^o \to e^+e^-$ at the CERN $\bar{p}p$ collider," *Phys. Lett.*, vol. B129, pp. 130–140, 1983.

[16] ALEPH, DELPHI, L3, OPAL and SLD, "Precision electroweak measurements on the Z resonance," *Phys. Rept.*, vol. 427, p. 257, 2006.

[17] The CDF Collaboration, "Measurement of $\sigma(p\bar{p} \to \mathrm{Z})\cdot\mathrm{Br}(\mathrm{Z} \to \tau\tau)$ in $p\bar{p}$ Collisions at $\sqrt{s} = 1.96$ TeV," *Phys. Rev.*, vol. D75, p. 092004, 2007.

[18] The D0 Collaboration, "Measurement of $\sigma(p\bar{p} \to \mathrm{Z} + \mathrm{X}) \cdot \mathrm{Br}(\mathrm{Z} \to \tau^+\tau^-)$ at $\sqrt{s} = 1.96$ TeV," *Phys. Lett.*, vol. B670, pp. 292–299, 2009.

[19] P. M. Nadolsky, "Theory of W and Z boson production," *AIP Conf.Proc.*, vol. 753, pp. 158–170, 2005.

[20] S. Catani, L. Cieri, G. Ferrera, D. de Florian, and M. Grazzini, "Vector boson production at hadron colliders: a fully exclusive QCD calculation at NNLO," *Phys. Rev. Lett.*, vol. 103, p. 082001, 2009.

[21] CERN, *oai:cds.cern.ch:1344820. EuCARD-AccNet-EuroLumiWorkshop: The High-Energy Large Hadron Collider*, (Geneva), CERN, 2011.

[22] S. Baird, "Accelerators for pedestrians; rev. version," Tech. Rep. AB-Note-2007-014. CERN-AB-Note-2007-014. PS-OP-Note-95-17-Rev-2. CERN-PS-OP-Note-95-17-Rev-2, CERN, Geneva, Feb 2007.

[23] The ATLAS Collaboration, "The ATLAS Experiment at the CERN Large Hadron Collider," *J. Instrum.*, vol. 3, p. S08003. 437 p, 2008. Also published by CERN Geneva in 2010.

[24] T. Akesson, H. Carling, B. Dolgoshein, C. Fabjan, P. Farthouat, D. Froidevaux, W. Funk, S. Furletov, I. Gavrilenko, M. Holder, V. Ivochkin, S. Jagielski, O. Kondratiev, S. Konovalov, A. Konstantinov, M. Kopitin, P. Lichard, S. Muraviev, A. Nadtochi, P. Nevski, P. Norton, V. Peshekhonov, V. Polychronakos, M. Potekhin, V. Radeka, R. Richter, A. Ramaniouk, D. Saxon, V. Schegelsky, J. Shank, A. Shmeleva, S. Smirnov, V. Sosnovtsev, E. Spiridenkov, M. Stavrianakou, D. Stephani, V. Tcherniatin, L. Vassilieva, J. Whitaker, and N. Zaganidis, "Particle identification performance of a straw transition radiation tracker prototype," *Nuclear Instruments and Methods in Physics Research Section A: Accelerators, Spectrometers, Detectors and Associated Equipment*, vol. 372, no. 1-2, pp. 70 – 84, 1996.

[25] N. Metropolis and S. Ulam, "The Monte Carlo Method," *Journal of the American Statistical Association*, vol. 44, pp. 335–341, 1949.

[26] V. N. Gribov and L. N. Lipatov, "Deep inelastic e p scattering in perturbation theory," *Sov. J. Nucl. Phys.*, vol. 15, pp. 438–450, 1972.

[27] Y. L. Dokshitzer, "Calculation of the Structure Functions for Deep Inelastic Scattering and e+ e- Annihilation by Perturbation Theory in Quantum Chromodynamics," *Sov. Phys. JETP*, vol. 46, pp. 641–653, 1977.

[28] G. Altarelli and G. Parisi, "Asymptotic Freedom in Parton Language," *Nucl. Phys.*, vol. B126, p. 298, 1977.

[29] W. Stirling Tech. Rep. private communication. http://www.hep.phy.cam.ac.uk/ wjs/plots/plots.html.

[30] The ATLAS Collaboration, "The atlas simulation infrastructure," *The European Physical Journal C - Particles and Fields*, vol. 70, pp. 823–874, 2010. 10.1140/epjc/s10052-010-1429-9.

[31] T. Sjostrand, S. Mrenna, and P. Skands, "PYTHIA 6.4 physics and manual," *JHEP*, vol. 05, p. 026, 2006.

[32] S. Frixione and B. R. Webber, "Matching NLO QCD computations and parton shower simulations," *JHEP*, vol. 0206, p. 029, 2002.

[33] G. Corcella *et al.*, "HERWIG 6.5," *JHEP*, vol. 0101, p. 010, 2001.

[34] S. Jadach, Z. Was, R. Decker, and J. H. Kühn, "The τ decay library TAUOLA, version 2.4," *Comput. Phys. Commun.*, vol. 76, pp. 361–380, 1993.

[35] P. Golonka and Z. Was, "PHOTOS Monte Carlo: a precision tool for QED corrections in Z and W decays," *The European Physical Journal C - Particles and Fields*, vol. 45, pp. 97–107, 2006. 10.1140/epjc/s2005-02396-4.

[36] A. Sherstnev and R. S. Thorne, "Parton Distributions for LO Generators," *Eur. Phys. J.*, vol. C55, pp. 553–575, 2008.

[37] P. M. Nadolsky *et al.*, "Implications of CTEQ global analysis for collider observables," *Phys. Rev.*, vol. D78, p. 013004, 2008.

[38] The ATLAS Collaboration, "Charged particle multiplicities in pp interactions at $\sqrt{s} = 0.9$ and 7 TeV in a diffractive limited phase-space measured with the ATLAS detector at the LHC and new `PYTHIA6` tune," Tech. Rep. ATLAS-CONF-2010-031, CERN, Geneva, Jul 2010.

[39] S. Frixione, P. Nason, and B. R. Webber, "Matching NLO QCD and parton showers in heavy flavour production," *Journal of High Energy Physics*, vol. 2003, no. 08, p. 007, 2003.

[40] S. Agostinelli, J. Allison, K. Amako, J. Apostolakis, H. Araujo, P. Arce, M. Asai, D. Axen, S. Banerjee, G. Barrand, F. Behner, L. Bellagamba, J. Boudreau, L. Broglia, A. Brunengo, H. Burkhardt, S. Chauvie, J. Chuma, R. Chytracek, G. Cooperman, G. Cosmo, P. Degtyarenko, A. Dell'Acqua, G. Depaola, D. Dietrich, R. Enami, A. Feliciello, C. Ferguson, H. Fesefeldt, G. Folger, F. Foppiano, A. Forti, S. Garelli, S. Giani, R. Giannitrapani, D. Gibin, J. G. Cadenas, I. Gonzlez, G. G. Abril, G. Greeniaus, W. Greiner, V. Grichine, A. Grossheim, S. Guatelli, P. Gumplinger, R. Hamatsu, K. Hashimoto, H. Hasui, A. Heikkinen, A. Howard, V. Ivanchenko, A. Johnson,

F. Jones, J. Kallenbach, N. Kanaya, M. Kawabata, Y. Kawabata, M. Kawaguti, S. Kelner, P. Kent, A. Kimura, T. Kodama, R. Kokoulin, M. Kossov, H. Kurashige, E. Lamanna, T. Lampn, V. Lara, V. Lefebure, F. Lei, M. Liendl, W. Lockman, F. Longo, S. Magni, M. Maire, E. Medernach, K. Minamimoto, P. M. de Freitas, Y. Morita, K. Murakami, M. Nagamatu, R. Nartallo, P. Nieminen, T. Nishimura, K. Ohtsubo, M. Okamura, S. O'Neale, Y. Oohata, K. Paech, J. Perl, A. Pfeiffer, M. Pia, F. Ranjard, A. Rybin, S. Sadilov, E. D. Salvo, G. Santin, T. Sasaki, N. Savvas, Y. Sawada, S. Scherer, S. Sei, V. Sirotenko, D. Smith, N. Starkov, H. Stoecker, J. Sulkimo, M. Takahata, S. Tanaka, E. Tcherniaev, E. S. Tehrani, M. Tropeano, P. Truscott, H. Uno, L. Urban, P. Urban, M. Verderi, A. Walkden, W. Wander, H. Weber, J. Wellisch, T. Wenaus, D. Williams, D. Wright, T. Yamada, H. Yoshida, and D. Zschiesche, "Geant4-a simulation toolkit," *Nuclear Instruments and Methods in Physics Research Section A: Accelerators, Spectrometers, Detectors and Associated Equipment*, vol. 506, no. 3, pp. 250 – 303, 2003.

[41] The ATLAS Collaboration, "Measurement of the inclusive $W^{\pm}$ and Z/γ^{*} cross sections in the electron and muon decay channels in pp collisions at $\sqrt{s} = 7$ TeV with the ATLAS detector," 2011. arXiv:1109.5141 [hep-ex], Accepted for publication by PRD.

[42] The ATLAS Collaboration, "Measurement of the $W \to l\nu$ and $Z/\gamma* \to ll$ production cross sections in proton-proton collisions at $\sqrt{s} = 7$ TeV with the ATLAS detector," *JHEP*, vol. 12, p. 060, 2010.

[43] T. Cornelissen, M. Elsing, S. Fleischmann, W. Liebig, E. Moyse, and A. Salzburger, "Concepts, Design and Implementation of the ATLAS New Tracking (NEWT)," Tech. Rep. ATL-SOFT-PUB-2007-007. ATL-COM-SOFT-2007-002, CERN, Geneva, Mar 2007.

[44] T. Cornelissen, M. Elsing, I. Gavrilenko, W. Liebig, E. Moyse, and A. Salzburger, "The new ATLAS track reconstruction (NEWT)," *Journal of Physics: Conference Series*, vol. 119, no. 3, p. 032014, 2008.

[45] M. Cacciari, G. P. Salam, and G. Soyez, "The anti-k$_T$ jet clustering algorithm," *JHEP*, vol. 04, p. 063, 2008.

[46] The ATLAS Collaboration, "Jet energy scale and its systematic uncertainty in proton-proton collisions at $\sqrt{s} = 7$ TeV in ATLAS 2010 data," Tech. Rep. ATLAS-CONF-2011-032, CERN, Geneva, Mar 2011.

[47] The ATLAS Collaboration, "Electron and photon reconstruction and identification in ATLAS: expected performance at high energy and results at 900 GeV," Tech. Rep. ATLAS-CONF-2010-005, CERN, Geneva, Jun 2010.

[48] ATLAS Collaboration, "Electron performance measurements with the atlas detector using the 2010 lhc proton-proton collision data. oai:cds.cern.ch:1390635," Tech. Rep. arXiv:1110.3174. CERN-PH-EP-2011-117, CERN, Geneva, Oct 2011. Accepted for publication by Eur. Phys. J. C.

[49] The ATLAS Collaboration, "Muon reconstruction efficiency in reprocessed 2010 LHC proton-proton collision data recorded with the ATLAS detector," Tech. Rep. ATLAS-CONF-2011-063, CERN, Geneva, Apr 2011.

[50] The ATLAS Collaboration, "Reconstruction, Energy Calibration, and Identification of Hadronically Decaying Tau Leptons," Tech. Rep. ATLAS-CONF-2011-077, CERN, Geneva, May 2011.

[51] W. Lampl *et al.*, "Calorimeter Clustering Algorithms: Description and Performance," Tech. Rep. ATL-LARG-PUB-2008-002. ATL-COM-LARG-2008-003, CERN, Geneva, Apr 2008.

[52] T. Barillari *et al.*, "Local Hadronic Calibration," Tech. Rep. ATL-LARG-PUB-2009-001-2. ATL-COM-LARG-2008-006. ATL-LARG-PUB-2009-001, CERN, Geneva, Jun 2008. Due to a report-number conflict with another document, the report-number ATL-LARG-PUB-2009-001-2 has been assigned.

[53] The ATLAS Collaboration, "Data-Quality Requirements and Event Cleaning for Jets and Missing Transverse Energy Reconstruction with the ATLAS Detector in Proton-Proton Collisions at a Center-of-Mass Energy of $\sqrt{s} = 7$ TeV," Tech. Rep. ATLAS-CONF-2010-038, CERN, Geneva, Jul 2010.

[54] A. Hcker, J. Stelzer, F. Tegenfeldt, H. Voss, K. Voss, A. Christov, S. Henrot-Versill, M. Jachowski, A. Krasznahorkay, Y. Mahalalel, X. Prudent, and P. Speckmayer, "TMVA - Toolkit for Multivariate Data Analysis. oai:cds.cern.ch:1023102," Tech. Rep. physics/0703039. CERN-OPEN-2007-007, Mar 2007.

[55] The ATLAS Collaboration, "Tau Reconstruction and Identication Performance in ATLAS," Tech. Rep. ATLAS-CONF-2010-086, CERN, Geneva, Oct 2010.

[56] E. Barberio, M. Beckingham, D. Capriotti, S. Consonni, C. Gumpert, A. Kaczmarska, M. Kobel, S. Kuehn, K. Leonhardt, W. Mader, J. Novakova, X. Prudent, M. Schumacher, T. Shao, and N. Utecht, "Measurment of the cross section $\sigma \times \mathrm{BR}(Z \to \tau\tau)$ in the dilepton channel with the ATLAS detector: Supporting Note," Tech. Rep. ATL-COM-PHYS-2011-418, CERN, Geneva, Apr 2011.

[57] L. Lyons, D. Gibaut, and P. Clifford, "HOW TO COMBINE CORRELATED ESTIMATES OF A SINGLE PHYSICAL QUANTITY," *Nucl. Instrum. Meth.*, vol. A270, p. 110, 1988.

[58] A. Valassi, "Combining correlated measurements of several different physical quantities," *Nucl. Instrum. Meth.*, vol. A500, pp. 391–405, 2003.

[59] M. Blann, B. L. Berman, and T. T. Komoto, "Precompound-model analysis of photonuclear reactions," *Phys. Rev. C*, vol. 28, pp. 2286–2298, Dec 1983.

[60] H. W. BERTINI, "Intranuclear-cascade calculation of the secondary nucleon spectra from nucleon-nucleus interactions in the energy range 340 to 2900 mev and comparisons with experiment," *Phys. Rev.*, vol. 188, pp. 1711–1730, Dec 1969.

[61] G. Folger and J. Wellisch, "String parton models in GEANT4," *eConf*, vol. C0303241, p. MOMT007, 2003.

[62] B. Andersson, G. Gustafson, and B. Nilsson-Almqvist, "A model for low-p_{T} hadronic reactions with generalizations to hadron-nucleus and nucleus-nucleus collisions," *Nuclear Physics B*, vol. 281, no. 12, pp. 289 – 309, 1987.

[63] The ATLAS Collaboration, "Measurement of the Mis-identification Probability of τ Leptons from Hadronic Jets and from Electrons," Tech. Rep. ATLAS-CONF-2011-113, CERN, Geneva, Aug 2011.

[64] C. Bertella, A. Buckley, S. Chekanov, P. Giovaninni, G. A. Hare, N. Kanaya, D. Kar, S. Menke, J. Nielsen, J. Proudfoot, C. Roda, P. Starovoitov, I. Vivarelli, R. Yoshida, S. Wahrmund, and J. Zhang, "Studies of particle flow using calorimeter clusters in pp collisions at 900 GeV and 7 TeV with the ATLAS detector at the LHC." ATL-COM-PHYS-2010-440, 2010. Supporting notes can be found in ATL-COM-PHYS-2010-210, ATL-COM-PHYS-2010-293, ATL-COM-PHYS-2010-351, ATL-COM-PHYS-2010-367.

[65] The ATLAS Collaboration, "In-situ pseudo-rapidity inter-calibration to evaluate jet energy scale uncertainty and calorimeter performance in the forward region," Tech. Rep. ATLAS-CONF-2010-055, CERN, Geneva, Jul 2010.

[66] M. Aharrouche *et al.*, "Measurement of the response of the ATLAS liquid argon barrel calorimeter to electrons at the 2004 combined test- beam," *Nucl. Instrum. Meth.*, vol. A614, pp. 400–432, 2010.

[67] The ATLAS Collaboration, "Muon Momentum Resolution in First Pass Reconstruction of pp Collision Data Recorded by ATLAS in 2010," Tech. Rep. ATLAS-CONF-2011-046, CERN, Geneva, Mar 2011.

[68] F. Aaron *et al.*, "Combined Measurement and QCD Analysis of the Inclusive $e^{\pm}p$ Scattering Cross Sections at HERA," *JHEP*, vol. 1001, p. 109, 2010. 61 pages, 21 figures.

[69] The ATLAS Collaboration, "Updated Luminosity Determination in pp Collisions at $\sqrt{s} = 7$ TeV using the ATLAS Detector." ATLAS-CONF-2011-011, 2011.

[70] The ATLAS Collaboration, "Search for the Standard Model Higgs boson in the $H \to \tau^+\tau^-$ decay mode with 4.7 fb^{-1} of ATLAS data at $\sqrt{s} = 7$ TeV," Tech. Rep. ATLAS-CONF-2012-014, CERN, Geneva, Mar 2012.

[71] A. Elagin, P. Murat, A. Pranko, and A. Safonov, "A New Mass Reconstruction Technique for Resonances Decaying to di-tau," 2010. arXiv:1012.4686 [hep-ex].

[72] The ATLAS Collaboration, "Luminosity Determination in pp Collisions at $\sqrt{s}$=7 TeV Using the ATLAS Detector at the LHC," 2011. Submitted to EPJC.

[73] S. van der Meer, "Calibration of the effective beam height in the ISR. oai:cds.cern.ch:296752," Tech. Rep. CERN-ISR-PO-68-31. ISR-PO-68-31, CERN, Geneva, 1968.

Appendix A

ATLAS LUMINOSITY DETERMINATION

Ideally the instantaneous luminosity can be measured by:

$$\mathcal{L} = \frac{\mu n_b f_r}{\sigma_{\text{inel}}} \tag{A.1}$$

where μ is the average number of inelastic interactions per bunch crossing (BC) (Section 2.1), n_b is the number of bunches that cross the interaction point, f_r is the frequency at which bunches circulate the accelerator ring, and σ_{inel} is the proton-proton (pp) inelastic collision cross-section. The μ quantity cannot be measured directly, however, due to detector inefficiencies. Instead only the visible number of inelastic interactions per bunch crossing, defined as:

$$\mu_{\text{vis}} = \epsilon\mu, \tag{A.2}$$

can be measured, where ϵ is the detector efficiency. Substituting into equation A.1 yields:

$$\mathcal{L} = \frac{\mu n_b f_r}{\sigma_{\text{inel}}} = \frac{\mu_{\text{vis}} n_b f_r}{\epsilon\sigma_{\text{inel}}} = \frac{\mu_{\text{vis}} n_b f_r}{\sigma_{\text{vis}}} \tag{A.3}$$

where $\sigma_{\text{vis}} = \epsilon\sigma_{\text{inel}}$ is now the observable inelastic pp collision cross-section [72, 69].

Thus, in order to measure the luminosity for every data run, the calibration constant, σ_{vis}, must be known (the μ_{vis} will be measured for each run while n_b and f_r are known accelerator parameters). In order to measure σ_{vis}, Van der Meer (vdM) scans were employed to measure the individual widths of the horizontal and vertical beam profiles, Σ_x and Σ_y respectively [73], which can then be used to alternatively measure the luminosity as:

$$\mathcal{L} = \frac{n_b f_r n_1 n_2}{2\pi\Sigma_x\Sigma_y}, \tag{A.4}$$

where n_1 and n_2 represent the number of protons in the respective beam's bunches. Combining the previous equation with equation A.2, one can solve for σ_{vis}:

$$\sigma_{\text{vis}} = \frac{\mu_{\text{vis}} 2\pi\Sigma_x\Sigma_y}{n_1 n_2}. \tag{A.5}$$

In (vdM) scans, the rate of interactions is measured as a function of beam separation in both the x and y directions. A peak interaction rate is expected at a distance of zero beam separation, while the rate is expected to fall off as Gaussian as the beam separation distance is increased. The horizontal and vertical beam width profiles can then be extracted from a Gaussian fit. Once the beam profiles, Σ_x and Σ_y, are extracted, the calibration constant σ_{vis} can be extracted and the luminosity can be determined on a run by run basis.